

Causes and Mitigation of Radio Frequency (RF) Blackout During Reentry of Reusable Launch Vehicles

26 January 2007

Prepared by

R. A. HARTUNIAN¹, G. E. STEWART², S. D. FERGASON³,
T. J. CURTISS⁴ and R. W. SEIBOLD⁵

¹Launch Systems Division, Space Launch Operations; ²Antenna Systems Department, Communication Systems Implementation Subdivision; ³Fluid Mechanics Department, Vehicle Performance Subdivision; ⁴Propulsion Science Department, Space Materials Laboratory; ⁵Civil/Commercial Launch Systems, Space Launch Projects

Prepared for

VOLPE NATIONAL TRANSPORTATION SYSTEMS CENTER
U.S. DEPARTMENT OF TRANSPORTATION
Cambridge, MA 02142

Contract No. DTRT57-05-D-30103, Task 7.0

Space Launch Operations

PUBLIC RELEASE IS AUTHORIZED

REPORT DOCUMENTATION PAGE			Form Approved OMB No. 0704-0188		
<p>The public reporting burden for this collection of information is estimated to average 1 hour per response, including the time for reviewing instructions, searching existing data sources, gathering and maintaining the data needed, and completing and reviewing the collection of information. Send comments regarding this burden estimate or any other aspect of this collection of information, including suggestions for reducing the burden, to the Department of Defense, Executive Services and Communications Directorate (0704-0188). Respondents should be aware that notwithstanding any other provision of law, no person shall be subject to any penalty for failing to comply with a collection of information if it does not display a currently valid OMP control number.</p> <p>PLEASE DO NOT RETURN YOUR FORM TO THE ABOVE ORGANIZATION.</p>					
1. REPORT DATE (DD-MM-YYYY) 26-01-2007		2. REPORT TYPE Contractor Final Report		3. DATES COVERED (FROM - TO) June – September 2006	
4. TITLE AND SUBTITLE Causes and Mitigation of Radio Frequency (RF) Blackout During Reentry of Reusable Launch Vehicles			5A. CONTRACT NUMBER DTRT57-05-D-30103		
			5B. GRANT NUMBER		
			5C. PROGRAM ELEMENT NUMBER		
6. AUTHOR(S)* R. A. HARTUNIAN, G. E. STEWART, S. D. FERGASON, T. J. CURTISS, AND R. W. SEIBOLD			5D. PROJECT NUMBER FA2R CL411		
			5E. TASK NUMBER Task Order #7		
			5F. WORK UNIT NUMBER FA2R CL411		
7. PERFORMING ORGANIZATION NAME(S) AND ADDRESS(ES) U.S. Department of Transportation Research and Innovative Technology Administration Volpe National Transportation Systems Center Safety Information Systems Division Cambridge, MA 02142-1093			8. PERFORMING ORGANIZATION REPORT NUMBER DOT-VNTSC-FAA-06-23		
9. SPONSORING/MONITORING AGENCY NAME(S) AND ADDRESS(ES) U.S. Department of Transportation Federal Aviation Administration Office of the Assoc. Administrator for Commercial Space Transportation Washington, DC 20591			10. SPONSOR/MONITOR'S ACRONYM(S) FAA AST-300		
			11. SPONSOR/MONITOR'S REPORT NUMBER(S)		
12. DISTRIBUTION/AVAILABILITY STATEMENT PUBLIC RELEASE IS AUTHORIZED					
13. SUPPLEMENTARY NOTES *The Aerospace Corporation, El Segundo, CA 90245-4691. Aerospace Corporation Report No. ATR-2006(5309)-1					
14. ABSTRACT <p>The Aerospace Corporation was tasked to assess radio frequency (RF) blackout phenomena caused by plasma generation around vehicles during reentry and presently known methodologies for mitigation of this condition inhibiting communications. The purpose was to understand these phenomena and mitigation approaches applicable to reusable launch vehicles (RLVs) used for commercial space. The viability and limitations of selecting frequency bands amenable to continuous communication in presence of plasma sheaths were assessed and mitigation recommendations provided.</p> <p>The ability to predict the ionized flow field for classes of vehicles most likely to emerge as hypersonic space transportation systems, with sufficient accuracy to identify the altitudes of blackout onset and recovery within reasonable bounds, has been demonstrated for altitudes greater than approximately 100 kft. This high-altitude regime is the most likely for future space transportation due to low g forces and low heat loads. For the lower, suborbital altitudes, many commercial RLVs will not be subjected to RF blackout because their relatively low velocities will not create conditions that generate plasma.</p> <p>Determination of the interaction of RF with a known ionized layer, including reflection, attenuation, refraction, high-power breakdown limits, and also effects of the plasma on the antenna characteristics, have been demonstrated successfully. Analytic codes are available to evaluate these phenomena.</p> <p>Approaches for mitigating the interruption of communications due to interactions of plasma electrons with RF signals are reviewed. The most promising are: aerodynamic shaping, injection of quenchants, use of magnetic windows, and use of high frequencies.</p>					
15. SUBJECT TERMS Reusable Launch Vehicle, RLV, Plasma Sheath, Radio Frequency Blackout, RF Blackout, Licensing, Regulation					
16. SECURITY CLASSIFICATION OF:			17. LIMITATION OF ABSTRACT UU	18. NUMBER OF PAGES 90	19A. NAME OF RESPONSIBLE PERSON James N. Hallock, Ph.D.
A. REPORT U	B. ABSTRACT U	C. THIS PAGE U			

CAUSES AND MITIGATION OF RADIO FREQUENCY (RF) BLACKOUT DURING REENTRY OF REUSABLE LAUNCH VEHICLES

Prepared by

R. A. HARTUNIAN¹, G. E. STEWART², S. D. FERGASON³,
T. J. CURTISS⁴ and R. W. SEIBOLD⁵

¹Launch Systems Division, Space Launch Operations; ²Antenna Systems Department, Communication Systems Implementation Subdivision; ³Fluid Mechanics Department, Vehicle Performance Subdivision; ⁴Propulsion Science Department, Space Materials Laboratory; ⁵Civil/Commercial Launch Systems, Space Launch Projects

26 January 2007

Space Launch Operations
THE AEROSPACE CORPORATION
El Segundo, CA 90245-4691

Prepared for

VOLPE NATIONAL TRANSPORTATION SYSTEMS CENTER
U.S. DEPARTMENT OF TRANSPORTATION
Cambridge, MA 02142

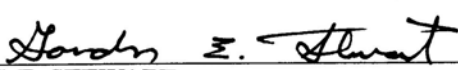
Contract No. DTRT57-05-D-30103, Task 7.0

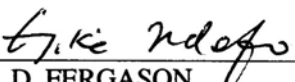
PUBLIC RELEASE IS AUTHORIZED


CAUSES AND MITIGATION OF RADIO FREQUENCY (RF)
BLACKOUT DURING REENTRY OF REUSABLE LAUNCH
VEHICLES

Prepared by


R. A. HARTURNIAN
Launch Systems Division
Space Launch Operations


G. E. STEWART
Antenna Systems Department
Communication Systems Implementation Subdivision


S. D. FERGASON
Fluid Mechanics Department
Vehicle Performance Subdivision

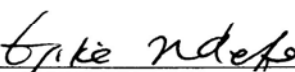

T. J. CURTISS
Propulsion Science Department
Space Materials Laboratory


R. W. SEIBOLD
Civil/Commercial Launch Systems
Space Launch Projects

Approved


E. K. RUTH, Systems Director
Civil/Commercial Launch Systems
Space Launch Projects


F. A. PISANO III, Director
Antenna Systems Department
Communication Systems Implementation Subdivision


E. D. NDEFO, Director
Fluid Mechanics Department
Vehicle Performance Subdivision


T. B. STEWART, Acting Director
Propulsion Science Department
Space Materials Laboratory

Abstract

The Aerospace Corporation was tasked to assess radio frequency (RF) blackout phenomena caused by plasma generation around vehicles during reentry and presently known methodologies for mitigation of this condition inhibiting communications. The purpose was to understand these phenomena and mitigation approaches applicable to reusable launch vehicles (RLVs) used for commercial space. The viability and limitations of selecting frequency bands amenable to continuous communication in presence of plasma sheaths were assessed and mitigation recommendations provided.

The ability to predict the ionized flow field for classes of vehicles most likely to emerge as hypersonic space transportation systems, with sufficient accuracy to identify the altitudes of blackout onset and recovery within reasonable bounds, has been demonstrated for altitudes greater than approximately 100 kft. This high-altitude regime is the most likely for future space transportation due to low g forces and low heat loads. For the lower, suborbital altitudes, many commercial RLVs will not be subjected to RF blackout because their relatively low velocities will not create conditions that generate plasma.

Determination of the interaction of RF with a known ionized layer, including reflection, attenuation, refraction, high-power breakdown limits, and also effects of the plasma on the antenna characteristics, have been demonstrated successfully. Analytic codes are available to evaluate these phenomena.

Approaches for mitigating the interruption of communications due to interactions of plasma electrons with RF signals are reviewed. The most promising are: aerodynamic shaping, injection of quenchants, use of magnetic windows, and use of high frequencies.

Acknowledgments

The authors are grateful to the Office of the Associate Administrator for Commercial Space Transportation, Federal Aviation Administration (FAA/AST), for the opportunity to work on this project. Specifically, gratitude is extended to Mr. Pradipta Shome at FAA/AST for valuable guidance on AST regulatory and licensing needs and insights on plasma sciences. The authors also wish to thank the following personnel at the DOT Volpe National Transportation Systems Center, who provided valuable insight into relevant technical issues and government needs and regulations: Ms. Ann R. DiMare, who served as the Contracting Officer's Technical Representative (COTR), and Dr. James N. Hallock and Ms. Ruth A. Hunter, who carefully reviewed and edited this report.

Dr. Richard A. Hartunian and Dr. Gordon E. Stewart served as Co-Principal Investigators at The Aerospace Corporation, and Mr. Robert W. Seibold served as Program Manager. Dr. Hartunian contributed to descriptions and analysis of representative vehicle classes, and Dr. Stewart led the antenna and radio frequency research. Support was provided by Dr. Stephen D. Ferguson, who analyzed vehicle environments, and Dr. Thomas J. Curtiss, who contributed to understanding of electrophilic quenchants and other blackout mitigation approaches. The authors are grateful for valuable guidance and support provided by Dr. Richard L. Baker (reentry ablation and plasma effects), Mr. Lindsay Coffman (Shuttle Orbiter trajectories and blackout), and Mr. Hubert Chew (atmospheric effects).

Executive Summary

The Aerospace Corporation was tasked by the Volpe National Transportation Systems Center to provide technical support to the Federal Aviation Administration, Office of Commercial Space Transportation (FAA/AST), to assess radio frequency (RF) blackout phenomena caused by plasma generation around vehicles during reentry. This assessment included evaluation of known methodologies, including selection of frequency bands to provide continuous communication, for mitigation of this condition. The purpose was to understand these phenomena and mitigation approaches applicable to expendable launch vehicles (ELVs) and reusable launch vehicles (RLVs) intended for commercial space transportation. The viability and limitations of selecting frequency bands amenable to continuous communication in presence of plasma sheaths were assessed and mitigation recommendations provided.

Background

Blackout is caused when the RF transmission waves used for communication are attenuated and/or reflected by electrons in the plasma sheaths. The major source of the electrons is the extreme heating of the air by strong shock waves originating at all vehicle leading edges and surrounding the vehicle for blunt vehicles, and viscous dissipation of a layer of air on the surface of sharp leading-edge vehicles [Fuhs, 1963; Steiger et al., 1970]. A more detailed explanation of the electron source is presented in the Appendix. In general, transmission is possible at RF frequencies greater than the characteristic “plasma frequency,” a plasma parameter that scales with the square root of the electron density in the plasma sheaths. Electron densities depend strongly on the vehicle shape, altitude, velocity (and therefore temperature of the plasma sheath), and the angle of attack (AoA) of vehicle surfaces with respect to the direction of flight. During flight trajectories, vehicles can generate electron densities with plasma frequencies exceeding the RF transmission frequency, leading to communication blackouts. Communication is restored when plasma frequencies decrease, due mostly to the deceleration to lower vehicle velocities and increase in collision frequency of electrons with neutral particles due to the higher density of the plasma at lower altitudes.

Approach and Findings

The approach taken in this study is listed below:

1. Vehicle classes to be evaluated were defined. These included RLVs most likely to be used for space transportation in the future and other classes selected because of published flight data relevant to the reentry blackout problem.
2. Ionized flow fields for each vehicle class were defined over a characteristic trajectory. In the absence of published flight data, the best state-of-the-art flow field codes were used to predict the ionized flow field. In each case, the altitudes of onset and subsequent recovery from blackout were highlighted.
3. RF interaction with the ionized flow field is presented.
4. Mitigation methodologies were studied and promising concepts recommended for more detailed assessment in actual application to full-scale RLVs.
5. Frequency bands best suited for RF transmission through plasma were reviewed.

This report is organized to present these subjects in the order listed above.

Representative Vehicle Classes

Three main classes of vehicles were selected: ballistic reentry vehicles, unpowered lifting glide vehicles, and powered air-breathing lifting vehicles. The latter two classes are candidate reusable vehicles for future commercial space transportation, while the ballistic reentry vehicles were included because they are the only source of relevant published flight data for the blackout problem and also provided the primary data to validate prediction codes for hypersonic aerothermodynamic phenomena. To assure that all potential candidate configurations were addressed, powered air-breathing lifting vehicles and a commercial cargo “slightly lifting” ballistic reentry vehicle were also studied.

The Space Shuttle Orbiter is an example of the unpowered lifting glide vehicle, while a number of powered air-breathing designs are offered but are awaiting scramjet and other technologies to mature. The comprehensive several-year, seven-vehicle flight test NASA Radio Attenuation Measurements (RAM) program, which focused on blunt, slender cones with nose radii of 1 in. and 4 in. (4 vehicles at 18 kft/sec reentry) and 6 in. (3 vehicles at 25 kft/sec reentry) is relevant to this study and is discussed. This program supported extensive laboratory tests and analytical programs. Predictive codes evolved and were compared to the flight data, all done predominantly in the 1960s and 1970s. The aerothermodynamic codes contributed to the design of the Orbiter’s thermal protection system and, more relevant to this study, to predicting the plasma flow field during reentry. Newer codes are also discussed.

Another class of vehicle was added in response to a request from FAA/AST. This class can be described as a ballistic, large, very blunt-nosed cylinder with a flare at its aft end. The two-stage K-1 vehicle, being developed by a private enterprise, Rocketplane Kistler, Inc. (RpK) falls into this category. The second stage goes to orbit, delivers the payload, reenters the atmosphere, and is ultimately recovered by deploying parachutes at Mach 2.5. On August 18, 2006, RpK received a \$207M award from NASA under the Commercial Orbital Transportation Services (COTS) demonstration program to help complete the K-1 reusable rocket and develop a cargo module that could later be modified to carry astronauts to the International Space Station.

Definition of Plasma Flow Fields

For each class of vehicles, the first step undertaken was to define the ionized flow field (plasma sheath) around the vehicle over a typical trajectory for that vehicle class. Actual flight-measured data were used where available in the open literature, while analytic predictions were used and are presented for vehicles with no flight plasma data. For each vehicle class, the altitude and velocity at the onset of and recovery from blackout are indicated on a typical trajectory plot.

Ballistic Reentry Vehicles

Simple axisymmetric bodies are usually categorized, for the purposes of plasma sheath analysis, as blunt- or sharp-nosed, depending on the dominant source of plasma formation. Thus, a blunt-nosed body is one whose sheath properties are determined by air that has passed through a normal or nearly normal strong shock wave with potential to create large volume flows of plasma, whereas a sharp-nosed, slender body is one whose sheath properties are determined by viscous dissipation in the boundary layer, which on a sharp-nosed vehicle is supplied with air that has passed through a weak oblique shock [Fuhs, 1963]. Another distinguishing characteristic between blunt- and sharp-nosed vehicles is that for the former, the thickness of the plasma sheath on the conical part of the vehicle fills the volume of flow between the edge of the boundary layer of the reentry vehicle and the oblique shock wave, whereas the analogous volume on sharp, slender reentry vehicles is void of plasma.

Blunt Ballistic Vehicles

One class is very blunt-nosed vehicles and/or those that intentionally reenter the atmosphere at high angles of attack in order to decelerate at very high altitudes where the aerodynamic heating rates are very low (e.g., the Shuttle Orbiter reenters at 40° angle of attack). The Space Shuttle was still in development when the RAM C-III vehicle was flown. This vehicle had a 6 in. nose radius, and was blunt-nosed with a 9° half-angle cone and 51 in. length. It was instrumented with several four-frequency reflectometers and electrostatic probes on a rake (blade) that projected 5.5 in. (14 cm) from the reentry vehicle and had 16 probes evenly spaced to measure ion density (and therefore electron density) between the RV and the enveloping shock wave [Schexnayder et al., 1970; Jones and Cross, 1970]. (Schematic depictions of the RAM C vehicles and rakes are presented in Section 4.1.) This heavily instrumented vehicle provided the high-quality data required to validate codes. A NASA code [Schexnayder et al., 1970] was in generally good agreement with the diagnostic data at altitudes greater than 125 kft. At lower altitudes there was agreement with attenuation data but not with reflectometer data, for reasons not fully understood. Another code developed by authors at Cornell Aeronautical Laboratory [Dunn and Kang, 1973] compared favorably with the RAM data at high altitudes, 233–275 kft. They did not extend the calculations for RAM C below 233 kft. They point out that at higher altitudes, such as 275 kft, it is important to include more than the NO^+ ion, as had been the custom, but to add reactions leading to N_2^+ and O^+ .

The RAM C-III vehicle experienced onset of S-band blackout, for the antenna 9 in. along the centerline from the tip of the nose, at an altitude of 255 kft and velocity of 25 kft/sec and recovered from blackout at 80 kft altitude and 16.8 kft/sec velocity.

Insight into the effects of using higher-frequency RF to reduce reflection from the plasma sheath is derived from Table IV in Grantham [1970], page 81, which lists the onset altitude of 20% reflection at S, X, and K_a bands for four locations along the RAM C vehicle. For a station 9 in. along the centerline from the tip of the nose, going to X band from S band decreases the altitude of 20% reflection onset from 255 kft to 229 kft, whereas the K_a band achieves 20% reflection at 125 kft, for a reduction of 130 kft from S band. This could reduce the duration of blackout to only 4 seconds instead of 28 seconds for S band. Unfortunately, K_a band is attenuated by the atmosphere and cannot penetrate rain. The table also indicates a far smaller effect of moving the antenna farther aft of the nosetip. The reduction in onset of 20% reflection resulting from moving to the farthest possible location of the cone frustum is 20 kft, or only a 2-second reduction in blackout duration.

Sharp-Tipped Slender Cones

As indicated earlier, for sharp, slender vehicles, the air boundary layer ionizes to critical values (plasma frequency equal to RF frequency) and heats the RV surface, causing it to ablate and introduce molecules of the heat shield and some easily ionizable impurities into the flow. The air between the boundary layer edge and the weak, oblique shock wave does not reach ionization temperatures. At high altitudes the boundary layer is laminar and remains thin compared to the RF wavelength, which effectively reduces the attenuation. At 75 kft altitude, for a sharp vehicle geometry selected by Fuhs [1963] to represent this class, the boundary layer transitions from laminar (smooth) flow to turbulent flow, which increases the peak temperature of the air (and therefore the ionization level) and heating of the RV, and also increases the thickness of the boundary layer by a factor of four or more, causing the RF attenuation to increase dramatically, to a maximum over the entire trajectory.

However, a sharp, slender conical vehicle on a nonlifting ballistic trajectory would not be a candidate for commercial transportation. It has been included because a sharp-tipped cone with antennas could be mounted on RVs as a means of communication during periods where blackout might occur if the antennas were mounted directly on the body. This approach is addressed in Section 2.1.3.

Unpowered Lifting Glide Vehicle

The Space Shuttle Orbiter is the major representative of this vehicle class. Like the Apollo capsules, the reentering Orbiter was expected to experience communication blackout for a significant duration of reentry flight. After a number of flights, NASA determined that the onset of blackout occurred at 265 kft altitude and lasted through 162 kft altitude for a total duration of 16 minutes. The blackout was for S-band communication antennas mounted on the underside of the vehicle, which reenters at 40° angle of attack, exposing the antennas to very strong ionization at high altitudes. A practical solution to maintain communication throughout reentry was established by utilizing antennas above the crew compartment to transmit to ground stations via the Tracking & Data Relay Satellite System (TDRSS). In the early 1970s, while the Shuttle was in development, the NASA RAM program was flying instrumented, blunt-nosed ballistic vehicles to study the plasma that causes blackout (discussed above). Dunn and Kang [1973] predicted the ionized flow field around a 4 ft. nose radius 20° cone at 20° angle of attack as representative of the Orbiter. Using a software code that was validated by the RAM C data, they derived ionization profiles at high altitudes (233–275 kft). The altitude range was extended to 180 kft using results of colleagues who analyzed a blunted, delta-shaped orbiter at 20° angle-of-attack. A notable result of that work in 1973, eight years before Space Transportation System No. 1 (STS-1), and which used 20° angle-of-attack instead of 40°, is that they predicted blackout duration to be 15 minutes.

Powered Air-Breathing Lifting Vehicle

Many designs for the powered air-breathing hypersonic cruise vehicle class have been described. Under the National Aerospace Plane (NASP) program, three competitors designed and developed a single-stage-to-orbit vehicle, but the program was cancelled after three years. More recently NASA pursued a hypersonic cruising demonstration of air-breathing hypersonic propulsion under the X-43 program. The X-43 vehicles were designed to be launched from the nose of a Pegasus rocket at hypersonic speeds prior to engine ignition. The first launch of the X-43A in 2001 was aborted when the vehicle had to be destroyed in flight due to malfunction of the Pegasus booster. The second launch in 2004 was successful and Mach 7 flight was achieved. The program has now been cancelled.

There is currently no consensus as to a preferred design for a cruise vehicle, let alone for the velocity and altitude at which it would cruise. The NASA X-43 demonstrators targeted an altitude of 100 kft and Mach number range of 7–10. Given those parameters, combined with the fact that the cruise vehicle design must attain minimum drag and, therefore, will most likely have sharp leading edges and cruise at near zero angle of attack, the chance of having a blackout problem appears remote. Should higher Mach numbers and cruise altitudes prevail, the possibility of blackout would have to be reassessed.

Commercial Cargo “Slightly Lifting” Ballistic Reentry Vehicle

An example of a low-cost commercial class of vehicle presently under development is the Rocketplane Kistler, Inc. (RpK) two-stage fully recoverable K-1 vehicle. The second stage goes to orbit, delivers the payload, reenters the atmosphere, and is ultimately recovered by deploying parachutes at Mach 2.5. The vehicle is a large, very blunt-nosed cylinder with a large flare at its end. Since no flow field results have been found that address the ionization distribution, the trajectory that has been reported was used to make reasonable estimates of altitudes and velocities of blackout onset and recovery.

Development of Flight Test Instrumentation and Computer Codes

During the late '60s and early '70s, The Aerospace Corporation participated in developing flight test instrumentation for measuring the effects of the reentry sheath on electromagnetic systems. This work included initial measurements of the conductivity of the plasma sheath using conductance gauges as well as later work using aperture antennas to measure the electron density.

These measurements showed that the electromagnetic properties of the plasma can be well approximated by the Lorenz model. That is, there are no so-called “warm plasma” effects. The plasma can be modeled using an equivalent dielectric constant. The collision frequency, ν , which determines the ohmic loss, varies during reentry by six orders of magnitude.

Computer codes were developed based on this electromagnetic model of the plasma. Initially, the codes were used to predict the antenna patterns of slot antennas in a ground plane covered by a uniform plasma layer. They were then generalized to include variations of the plasma layer in the direction of the normal to the surface. Through further analysis, the ability to calculate the input impedance of individual slots and the mutual coupling between slots was added, so that it was possible to predict the performance of an array of slots in the presence of a nonuniform plasma layer. The analysis was extended to the case of axial and circumferential slots on a plasma-clad cylinder so that, to first order, the curvature of the vehicle could be included.

The results showed that, when the peak electron density occurred at low altitudes, as would be the case for a sharp-tipped, conical reentry body on a ballistic trajectory, the effect of the plasma on an aperture antenna could be modeled using a thin, conducting sheet of material such as “space cloth.”

At high altitudes, the plasma is nearly lossless because of the low collision frequency. The first modeling of lossless plasma was done using grids of thin wires. Later on, Aerospace developed a unique simulation facility where nearly lossless plasma could be produced over a metallic surface. The plasma-clad models were placed in an absorber-lined anechoic chamber capable of being evacuated, so that the effects of the plasma on the radiation patterns could be measured without any perturbing effects due to a radome, for instance. The electron density profile generated in this facility was measured using Langmuir probes.

The Aerospace computer codes were used for both preflight and postflight scenarios and were compared with contractors' models. An analysis of the RAM C-II was carried out as an example of relatively lossless plasma. The results compare favorably with the NASA calculations.

For axisymmetric/2-D boundary layer conditions, the most widely used algorithm in the industry is the Boundary Layer Integral Matrix Procedure (BLIMP) code [User's Guide, 1970; Lin et al., 1995]. BLIMP includes heatshield ablation effects in its formulation and has built-in multi-species transport properties and chemical reacting flows. Newer codes, e.g, HYpersonic GPS SIMulation (HYGPSIM), REACH, EMRUN, and PIRATE are discussed in Section 3.1.

Blackout Mitigation Approaches

The final task of this study was to identify proposed techniques for mitigating blackout and make recommendations to the Volpe Center and FAA/AST regarding which concepts are most promising for application to future commercial space transportation systems. The major concepts in the literature were reviewed, and two approaches were found to appear promising. These approaches were injection of quenchants and aerodynamic shaping, the latter focusing primarily on effects of nose radius. Another approach that was addressed was use of a magnetic field window concept.

Injection of Quenchants

Quenchants, e.g., water and electrophilics, can be injected into the plasma flow to reduce the ionization level. The Gemini 3 Reentry Capsule is an example of a successful flight demonstration that used injection of liquids into the flow to alleviate blackout. The Gemini 3 Reentry Capsule was manned by two astronauts and reentered the atmosphere on March 23, 1965 [Schroeder and Russo, 1968]. Significant levels of signal strength increase during the early portion of the water injection sequence over an altitude range of 272 to 246 kft were noted by ground stations on VHF telemetry (230.4 MHz) and VHF voice transmission (296.8 MHz). Enhancement of C-band beacon signal (5,690 MHz) was observed during the latter portion of the water injection sequence from 200 to 160 kft altitude. A comparison of calculated electron concentration – based on the theory that the primary mechanism of electron concentration reduction is assumed to be recombination at or near the surface of water drops, with values deduced from the observed VHF attenuation data – shows the same trends. The data from this flight provide evidence that it is possible to alleviate RF attenuation on a blunt body by water injection in the flow field.

Aerodynamic Shaping

The second technique that has promise is use of a sharp, slender probe, containing an antenna and made to project ahead of the bow shock of the blunt-nosed vehicle. This aerodynamic shaping concept is reported in a paper by Russian authors [Belov et al., 2001], who have done considerable analysis and experimental evaluation of the aerodynamics, heat transfer, and nose radius required to assure sufficiently low electron density to flow aft, where the antenna is located. The sharp nose-cone of the probe is a porous, sintered metal, selected to accommodate cold gas cooling for survival. Their paper portrays excellent knowledge of all issues that must be analyzed and tested for success of the concept.

To be sure, the Russian design is just one that applies the principle of sharp, slender aerodynamic shaping to avoid blackout. In the NASA RAM C flight series, a design of the electrostatic rake (blade) to measure ion densities in the shock layer, employed a blade-like design with an extremely sharp nosetip of 0.01 in. radius to hold the small metallic ion collectors [Schexnayder et al., 1970; Jones and Cross, 1970]. The rake was mounted on the very rear end of the conical heat shield and survived the heating down to 180 kft altitude, at which point it was retracted because of concerns that components would melt. The rake (blade) used on RAM C had a beryllium oxide (BeO) nosetip, which melts at 2,341°F. The authors propose that design of fully passive systems be emphasized, using, where needed, advanced materials such as fine-weave 3-D carbon-carbon composites. As mentioned above, schematic depictions of the RAM C vehicles and rakes are presented in Section 4.1.

In light of this, the authors recommend performance of a study to examine the rake design with an antenna, but using advanced thermal protection materials to assure survival to much lower altitudes. Recall, the Shuttle comes out of blackout at 162 kft, so for that application the survival altitude needs to be extended only an additional 18 kft. Application to other RLVs would also be examined. This approach will need to be reviewed in considerably more detail in order to validate it and apply it to candidate RLVs of the future. Also, other sharp, slender designs to house the antennas should be investigated.

Magnetic Field Window

A third technique for alleviating RF blackout would exploit the magnetic field window concept. Theory supports the concept that a static magnetic field applied to a plasma with field lines in the direction of intended RF propagation will, under appropriate conditions of magnetic field strength and certain parameters of the plasma, as well as the frequency of the RF, reduce the plasma attenuation

sufficiently to allow the RF to propagate through the plasma. Experiments conducted at NASA-Langley support that concept [Russo and Hughes, 1964]. In that work, the flow from a small, highly aluminized solid rocket motor was used, expanding the ionized flow to Mach 10 over a 2 in. nose radius, 9° half-angle conical model containing a VHF slot antenna aligned with the flow. Eight magnetic field coils that produced field strengths up to 750 gauss were applied under the antenna. The ionized flow parameters were electron density of about 3×10^{11} electrons/cm³ and collision frequency of 10⁹/sec. The measured attenuation was 60 dB through the plasma layer with no magnetic field applied and 40 dB when the magnetic field was turned on. Russo and Hughes concluded that demonstration of a 20 dB reduction of attenuation with application of a 750-gauss magnetic field indicates feasibility of the magnetic window technique.

Mitigating the potential efficacy of this finding, analyses by Starkey [2003] and Rothman et al. [1964] indicate that the magnetic field strength required to penetrate a reentry plasma sheath is on the order of 10⁴ gauss or more. Reconciliation of this one (or more) order of magnitude difference of required field strength is a topic of proposed further study. Another issue that must be addressed in applying magnetic fields to alleviate RF transmission through plasmas follows from an analysis by Usui et al. [2000]. These researchers concluded that a radiated unique right circular polarized wave of frequency (ω) equal to the cyclotron frequency, $\Omega_c \equiv (e/m) B_0$, called the whistler mode, will propagate through a plasma with moderate magnetic field as long as Ω_c is greater than the RF frequency. (In the above equation, e = electron charge, m = electron mass, and B_0 = magnetic induction, or number of magnetic lines per m²). As an example, for $\Omega_c/\omega = 1.8$ and for S-band RF, they estimate that a 1,500-gauss magnetic field would permit transmission through their model plasma, assuming a collisionless plasma. For reentry plasmas the collision frequency is quite low at very high altitudes but becomes higher as the vehicle descends.

Further study is needed to determine reasons for the large disparity of magnetic field strengths between the NASA experiment and the theoretical projections of Starkey [2003] and Rothman et al. [1964]. Regarding the proposed whistler mode, the study should include the effects of collision frequency, and if the use of whistler mode still looks attractive, experiments using a shock tube should be considered, where well defined plasmas could be produced, to evaluate its effectiveness. The study should also examine changes in the applied magnetic field produced by eddy currents in the moving conductive plasma. Additionally, effect of magnetic field presence on the plasma profile would need to be determined. Work done in the area of magneto-aerodynamics shows that, if the flow field has sufficiently high conductivity, it can produce changes in the drag and heat-transfer rate.

GPS Reception Enhancement

Typically, GPS antennas have wide-angle coverage with resultant low gain because of the desire to keep multiple satellites in the field of view. Low power from GPS signals would be further degraded by signal attenuation due to plasma sheaths around reentering vehicles. If the antenna is located on the aft side of a lifting reentry vehicle, there may be little attenuation because of the absence of a plasma sheath on that surface, but multipath phenomena might be produced by reflections from the wake and plasma spilling around the vehicle top and sides.

To increase the antenna gain and reduce the effects of multipath, an array antenna could be built that is capable of forming multiple receive beams. To achieve the best possible noise figure, a low-noise amplifier (LNA) would be provided for each element. Associated with each beam would be a beam-forming network. These beams could be pointed at individual satellites given the location and attitude of the reentry vehicle and the ephemeris data of the GPS satellites within the field of view. Alternatively, each beam could acquire and track a given GPS satellite.

Conclusions and Recommendations

The RF blackout mitigation strategies described above fall into two general classes: passive and active. Passive approaches tend to be less costly than active approaches and argue for attention to design to minimize the plasma effects on communications signals. Active approaches entail manipulation of the plasma conditions and electron density in localized regions surrounding communication antennas to facilitate RF transmission.

Examples of passive approaches to mitigating the RF blackout problem are: transmitting at higher frequencies, radiating higher power from the vehicle, or using an antenna with a surface aerodynamically shaped to produce low ionization levels that can be extended through the reentry sheath without perturbing it. Although increasing the frequency generally reduces attenuation, higher frequencies are more subject to atmospheric and rain attenuation. As a practical limit, 10 GHz is often suggested as an upper limit. Transmitting higher power from the vehicle is limited by aperture breakdown. Typical breakdown powers are in the range of hundreds of watts. Increasing the transmit power to compensate, as an example, for even 30 dB of attenuation is clearly impractical. Implementing one or a combination of passive approaches will minimize and possibly eliminate the blackout phenomenon. In our view, aerodynamic shaping is the most practical and influential approach for mitigating blackout. However, there are limitations in implementing such passive approaches and competing design requirements. For example, Belov et al. [2001] had to use cooling to protect their protruding tip from the environment, making it an active system.

Active approaches are designed to manipulate the plasma conditions and electron density in localized regions surrounding the communications antenna to facilitate RF transmission. Example active approaches include: injection of chemical quenchants or droplets that evaporatively cool the plasma and application of magnetic fields. These can be used periodically where passive approaches are inadequate. Among these, the use of quenchants is the more well established, practical method, particularly when requirements are periodic rather than continuous. Magnetic field mitigation holds some promise, particularly for continuous operation, but has not been demonstrated sufficiently, and the requirements appear daunting using existing technologies. Both of these active approaches (quenchants and magnetic fields) could be placed on a more secure footing with additional experimental work to validate model calculations, particularly the proposal by Usui et al. [2000] that unique “whistler” modes may facilitate RF communications in a narrow range of “resonant” transmission frequencies.

Several recommendations are proposed. The first is to study candidate mitigation methodologies such as aerodynamic shaping, injection of liquids, and application of a magnetic field, analytically and, where appropriate, experimentally, to prove that the concepts will work over the entire blackout period for a given vehicle configuration. For concepts shown to be viable, creation of full-scale system parametric designs is recommended, to assess size, weight, and complexity. A Failure Modes and Effects Analyses (FMEA) should then be performed for systems that progress to a potential implementation stage, to assure safety of the vehicle under all conditions.

Evaluation of indirect RF transmission from vehicles to the ground via satellites was beyond the scope of the present effort but might warrant exploration. This approach is used, for example, for the Space Shuttle. The parameters for commercial space vehicles should be explored, including considerations of employing commercial satellite constellations for communication.

The authors also recommend that an analysis be performed of frequency ranges suitable for commercial RLV developers, taking into account RF blackout amelioration and availability of frequencies not reserved for other applications incompatible with commercial launch vehicle use. Example issues to be explored for high frequencies would include atmospheric attenuation at approximately 10 GHz and above, compatibility with ground stations and satellites, and compatibility with Automatic Dependent Surveillance - Broadcast Mode (ADS-B) architecture. Example issues to be explored for low frequencies include antenna size, compatibility with ground stations and satellites, and workarounds such as gap antennas around the vehicle. Such research could lead to exploration and potential development of all-weather approaches for RF communications.

Contents

1. Introduction and Summary	1
2. Representative Vehicle Classes	3
2.1 Ballistic Reentry Vehicles	3
2.1.1 Sharp-Tipped Cones and Effect of Nose Radius	4
2.1.2 Blunt Cones	6
2.1.3 Blunt Cones with Sharp Tip	11
2.1.4 Plasma Level Variations with Vehicle Nose Radius and Heat Shield Impurity Levels	11
2.2 Commercial ELV and RLV Concepts	13
2.3 Unpowered Lifting Glide Vehicles	17
2.3.1 Space Shuttle Orbiter	18
2.3.2 Hypersonic Boost-Glide Vehicle	25
2.3.3 Powered Air-Breathing Hypersonic Cruise Vehicles	26
3. RF Interaction with Reentry Vehicle Flow Field	29
3.1 The Physical Problem	29
3.2 Plasma and RF Code Development	29
3.2.1 BLIMP, HYGPSIM, REACH, and EMRUN Codes	30
3.2.2 PIRATE Tool Set	31
3.3 Slot Gain vs. Frequency	31
3.4 Sharp-tipped Vehicle RF Results	32
3.5 Data for Sharp-tipped Configuration at Higher Frequencies	34
3.6 RAM C Radio Frequency Results	36
3.7 Antenna Breakdown	43
3.8 GPS Reception Enhancement	43
4. Identification and Comparison of Mitigation Approaches	45
4.1 Aerodynamic Shaping	45
4.2 Review of Quenchants, Their Properties, and Droplet Insertion	46
4.3 Magnetic Window	49
4.4 High Frequencies	53
4.5 High Transmit Power	54
4.6 Observations on Raman Scattering	55
5. Conclusions and Recommendations	57

5.1 Conclusions.....	57
5.2 Recommendations.....	59
6. Acronyms and Abbreviations.....	61
7. References.....	65
Bibliography	69
Appendix.....	A-1

Figures

Figure 1. Sharp-tipped ballistic RV with shock wave.	4
Figure 2. Clean air peak electron density decay. [Steiger et al., 1970].....	7
Figure 3. Electron density profile at X-band location. [Steiger et al., 1970].....	7
Figure 4. VHF attenuation. [Steiger et al., 1970]	8
Figure 5. Schematic of RAM C vehicles and reentry flow characteristics. [Rybak and Churchill, 1971].....	8
Figure 6. RAM C-II reentry trajectory showing onset and end of RF signal blackout. X-band and C-band reacquisition were delayed because of tracking difficulties. [Grantham, 1970]. (Reprinted courtesy of NASA).....	9
Figure 7. Comparison of measured and predicted electron density for RAM C flights. [Dunn and Kang, 1973]. (Reprinted courtesy of NASA)	10
Figure 8. Comparison of measured electron temperature to predicted translational temperature for RAM C flights. [Dunn and Kang, 1973]. (Reprinted courtesy of NASA)	10
Figure 9. Variation of electrons and positive ions (NO^+ , Impurities) with vehicle nose radius and heat shield impurity level for 0° angle of attack (AoA) at rear frustum and 50 kft altitude. [Mather et al., 2005]	12
Figure 10. Artist's conception of RpK K-1 reentry vehicle (Illustration reprinted courtesy of Kistler).	14
Figure 11. K-1 vehicle profile (Illustration reprinted courtesy of Kistler).	14
Figure 12. K-1 orbital vehicle reentry profile. [Kistler, 2002]. (Reprinted with permission of Kistler).....	15
Figure 13. Typical K-1 OV reentry trajectory. [Kistler, 2002]. (Reprinted with permission of Kistler).....	16
Figure 14. Blackout trajectories and times for reentry of Shuttle, RpK OV, RAM C, and sharp- tipped RVs.	17
Figure 15. Drawing of Space Shuttle Orbiter during reentry conditions (Drawing reprinted courtesy of NASA).....	18
Figure 16. Typical Space Shuttle reentry trajectory. [Starkey, 2003]. (Reprinted with permission of the American Institute of Aeronautics and Astronautics, Inc.).....	19
Figure 17. Schematic flow field. [Dunn and Kang, 1973]. (Reprinted courtesy of NASA)..	20
Figure 18. Assumed Space Shuttle trajectory. [Dunn and Kang, 1973]. (Reprinted courtesy of NASA).....	20

Figure 19. Plasma flow profiles for Shuttle configuration for 280 kft altitude. [Dunn and Kang, 1973]. (Reprinted courtesy of NASA).	21
Figure 20. Plasma flow profiles for Shuttle configuration for 310 kft altitude. [Dunn and Kang, 1973]. (Reprinted courtesy of NASA).	22
Figure 21. Plasma flow profiles for Shuttle configuration for 180 kft altitude. [Dunn and Kang, 1973]. (Reprinted courtesy of NASA).	23
Figure 22. Plasma flow profiles for Shuttle configuration for 220 kft altitude. [Dunn and Kang, 1973]. (Reprinted courtesy of NASA).	24
Figure 23. <i>Discovery</i> STS-121 hypersonic boundary layer transition from protruding aft gap-filler at Mach 18 reentry, captured by “Cast Glance” optics on Navy P-3 aircraft. (Image reprinted courtesy NASA).	25
Figure 24. Schematic of Dynasoar design configuration.	26
Figure 25. Schematic depiction of X-43 vehicles. (Reprinted courtesy of NASA).	27
Figure 26. Photo of X-43A vehicle during ground testing. (Reprinted courtesy of NASA).	27
Figure 27. Representation of the Physical Problem ($M =$ Mach number). [Nusca and Cooper, 1998]	30
Figure 28. Gain of Dynasil-filled guide.	33
Figure 29. Rectangular slot antenna geometry.	33
Figure 30. Collision frequency vs. altitude.	34
Figure 31. Sharp-tipped configuration, 60 kft.	35
Figure 32. Sharp-tipped configuration, 60 kft, variable collision frequency (ν).	35
Figure 33. Electron density profiles calculated preflight for contaminant-free flow at various altitudes. [Swift et al., 1970].	37
Figure 34. Slot gains for RAM C-III at 156 kft altitude.	37
Figure 35. Slot gains for RAM C-III at 131 kft altitude.	38
Figure 36. Conical model mounted in microwave anechoic chamber capable of being evacuated.	39
Figure 37. Tip of conical model with symmetrically excited gap showing coaxial feed and contours of constant electron density for excitation using an anode at the back.	39
Figure 38. Axial cut of E_θ radiation pattern for symmetrically excited cone clad with underdense plasma layer. Argon pressure 0.6 torr. [Stewart et al., 1970]. (Reprinted courtesy of NASA).	40
Figure 39. Axial cut of E_θ radiation pattern for symmetrically excited cone clad with overdense plasma layer. Argon pressure 0.6 torr. [Stewart et al., 1970]. (Reprinted courtesy of NASA).	40

Figure 40. Axial cut of E_0 radiation pattern for asymmetrically excited cone clad with overdense plasma layer. Argon pressure 0.6 torr. [Stewart et al., 1970]. (Reprinted courtesy of NASA).....	41
Figure 41. Comparison of RAM C-II microwave attenuation data with air theory. [Schexnayder et al., 1970]. (Reprinted courtesy of NASA).....	42
Figure 42. Broadside gain calculated as a function of frequency for RAM C at 156 kft altitude.	42
Figure 43. Power reflection coefficient, Trailblazer flight 2.	43
Figure 44. RAM C payload configurations, showing electrostatic ion-probe and thermocouple probe rakes. [Jones and Cross, 1970]. (Reprinted courtesy of NASA).....	47
Figure 45. Hypothetical blade configuration.....	48
Figure 46. Comparison of magnet weight using current technology with stainless steel structure and composite material structure.....	53
Figure 47. Estimates of magnet weight for carbon nanotubes (CN), projected from superconductivity data.	54
Figure A-1. Nonequilibrium flow species distribution for hemisphere on 20° cone at 280 kft altitude. [Dunn and Kang, 1973]. (Reprinted courtesy of NASA).....	A-4
Figure A-2. Nonequilibrium flow species distribution for hemisphere on 20° cone at 310 kft altitude. [Dunn and Kang, 1973]. (Reprinted courtesy of NASA).....	A-5
Figure A-3. Region of nonequilibrium flows for the Shuttle. [Rakich et al., 1982]. (Reprinted with permission of the American Institute of Aeronautics and Astronautics, Inc).	A-6
Figure A-4. Modeling flow phenomena for hypersonic flight. [From Bertin, J.J., <i>Hypersonic Aerothermodynamics</i> , reprinted with permission of the American Institute of Aeronautics and Astronautics, Inc.].....	A-7

Tables

Table 1. Data for Plasma Sheath on Sharp Cone.....	5
Table 2. K-1 Gross Liftoff Weight (GLOW) Summary (lbm). [Kistler, 2002].....	14
Table A-1. Chemical Reactions and Rate Coefficients used in Nonequilibrium Calculations [Dunn and Kang, 1973].....	A-3

1. Introduction and Summary

The Aerospace Corporation was tasked by the Volpe National Transportation Systems Center to assess radio frequency (RF) blackout phenomena caused by plasma generation around vehicles during reentry and published methodologies for mitigation of this condition inhibiting communications. This analysis was provided to Federal Aviation Administration, Office of Commercial Space Transportation (FAA/AST), to support understanding of these phenomena and mitigation approaches applicable to reusable launch vehicles (RLVs) under development for commercial space use. The viability and limitations of selecting frequency bands amenable to continuous communication in presence of plasma sheaths were assessed and mitigation recommendations provided.

Blackout is caused by high electron concentration in the plasma, which reflects or attenuates electromagnetic waves. Potential mitigation approaches that were explored included aerodynamic shaping, injection of electrophilics (molecules that reduce electron density in the plasma), and use of magnetic fields, high power, high frequencies, low frequencies, and lasers.

The approach taken in this study is listed below:

1. Vehicle classes to be evaluated were defined. These included RLV configurations most likely to be used for space transportation in the future and other classes selected because of the availability of published flight data relevant to the reentry blackout problem.
2. Ionized flow fields for each vehicle class were defined over a characteristic trajectory. In the absence of published flight data, the best state-of-the-art flow field software codes were used to predict the ionized flow field. In each case, the altitudes of onset and subsequent recovery from blackout were highlighted.
3. RF interaction with the ionized flow field is presented.
4. Mitigation methodologies were studied and promising concepts recommended for more detailed assessment in actual application to full-scale RLVs.
5. Frequency bands best suited for RF transmission through plasma were reviewed.

This report provides details on: (1) potential methods to mitigate communications outages during reentry and enable controller communications for operation within the National Airspace System (NAS) and the Space and Air Traffic Management System (SATMS) and (2) recommendations for providing uninterrupted communications through plasma sheaths. A detailed explanation of the electron source is presented in the Appendix.

2. Representative Vehicle Classes

Representative vehicle classes were selected to direct further study. Three main classes of vehicle were chosen: ballistic reentry vehicles, unpowered lifting glide vehicles, and powered air-breathing hypersonic vehicles. The latter two classes are candidate reusable vehicles for future commercial space transportation, while the ballistic reentry vehicles were included because they are the only source of relevant published flight data for the blackout problem and also provided the primary data to validate prediction codes for hypersonic aerothermodynamic phenomena. Within each of these groups, a number of specific subgroups were selected that represent either existing or designed vehicles that may experience blackout conditions. Examples of ballistic reentry vehicles include blunted cone (Genesis and Stardust sample return capsules) and sharp tip designs (experimental reentry vehicles). Examples of unpowered lifting glide vehicles are the Space Shuttle orbiter and several designs for hypersonic boost-glide vehicles (e.g., Dynasoar and Crew Return Vehicle). The study included one private enterprise's reentry vehicle design, the Rocketplane Kistler, Inc. (RpK) K-1 vehicle, which falls within the ballistic reentry category, but is a blunted cylinder flared at the aft end.

A comprehensive literature search was conducted, focusing on flight measurements of vehicle plasma sheath electron density distribution, as well as results from experimental blackout alleviation techniques. The search focus was later appended to include predicted plasma flow fields to allow for inclusion of vehicle classes with little or no flight history. Over 1,000 titles were reviewed for applicability. These were drawn from a variety of sources, including The Aerospace Corporation's Charles Lauritsen Library, the National Aeronautics and Space Administration (NASA) technical reports server, the NASA Langley Research Center (NASA-LaRC) technical reports server, the NASA Johnson Space Center (NASA-JSC) technical reports server, and American Institute of Aeronautics and Astronautics (AIAA) databases. Selected references deemed useful were acquired and reviewed in depth.

2.1 Ballistic Reentry Vehicles

Significant data on the reentry characteristics of ballistic vehicles are available in the open literature. These data are drawn mainly from efforts supporting ballistic missile programs, the NASA-LaRC Radio Attenuation Measurements (RAM) program, and NASA's Mercury, Gemini, and Apollo programs. For this study, ballistic reentry vehicles are defined as vehicles that do not provide active thrust or generate significant lift during the reentry phase. As a result, the vehicle flight-path angle is nearly constant (and typically small) over most of the reentry trajectory. Ballistic reentry trajectories are characterized by sharp peak in vehicle deceleration (magnitudes of 5 g's or more). Ballistic vehicles are typically designed as axisymmetric bodies.

Simple axisymmetric bodies are usually categorized, for the purposes of plasma sheath analysis, as blunt- or sharp-nosed, depending on the dominant source of plasma formation. Thus, a blunt-nosed body is one whose sheath properties are determined by air that has passed through a normal or nearly normal strong shock wave with potential to create large volume flows of plasma, whereas a sharp-nosed, slender body is one whose sheath properties are determined by viscous dissipation in the boundary layer, which on a sharp-nosed vehicle is supplied with air that has passed through a weak oblique shock [Fuhs, 1963]. Another distinguishing characteristic between blunt- and sharp-nosed vehicles is that for the former, the thickness of the plasma sheath on the conical part of the vehicle

fills the volume of flow between the edge of the boundary layer of the reentry vehicle and the oblique shock wave, whereas the analogous volume on sharp, slender reentry vehicles is void of plasma.

Fuhs also discussed an intermediate category of vehicle that may be described as slightly blunted. The boundary layer on the forward part of a slightly-blunted vehicle is fed by high-entropy gases from the nose. At some point along the vehicle, the high-entropy flow is absorbed by the boundary layer; downstream from that point the boundary layer feeds on air that has been processed by an oblique shock wave.

In the following sections, the plasma flow fields of ballistic reentry vehicles are defined. The main delineation between ballistic vehicle designs involves the shape of the conic section used. In general, two types of axisymmetric bodies are utilized for ballistic reentry vehicles—sharp or blunt cones.

2.1.1 Sharp-Tipped Cones and Effect of Nose Radius

The sharp tip cone configuration consists of an axisymmetric cone body with a small half-angle and small nose radius. The flow field for this configuration consists of an oblique shock wave that forms along the length of the body and a thin boundary layer. Figure 1 shows a turbulent wake along the aft portion of the vehicle. In this case, the flow of molecules through the normal shock wave at the small nose generates electrons, but not enough to ionize a large portion of the flow. Instead, the boundary layer on the surface provides the energy to increase the air temperature by viscous dissipation and cause ionization.

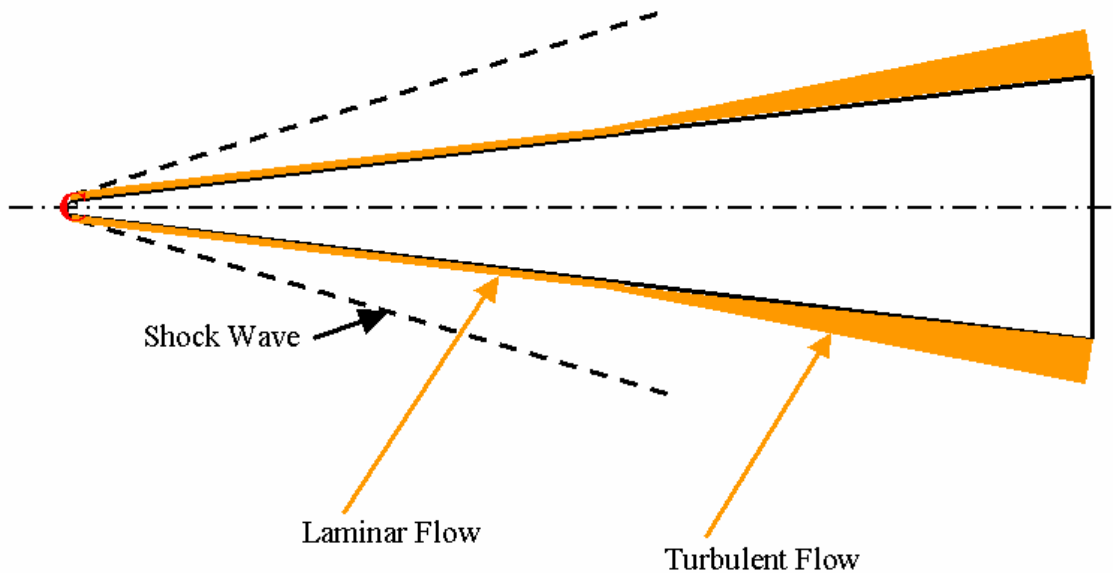


Figure 1. Sharp-tipped ballistic RV with shock wave.

Table 1 [Fuhs, 1963] contains information concerning the plasma sheath surrounding a sharp cone. In this table, ω_p = plasma frequency, ν = electron collision frequency, σ = electrical conductivity, δ = plasma sheath thickness, and N_e electron density. The quantity ω_p/ν determines the strength of magnetic field required to make ω_p/ν equal to unity. The plasma sheath thickness δ has been taken as being equal to the boundary-layer thickness and is calculated for a station 3 ft. from the nose.

For sharp, slender vehicles, the hot boundary layer not only ionizes the air but also heats the reentry vehicle (RV) surface, causing it to ablate and introduce molecules of the heat shield and some easily ionizable impurities into the flow. The air between the boundary layer edge and the shock wave does not reach ionization temperatures. At high altitudes the boundary layer is laminar and remains thin compared to the radio-frequency (RF) wavelength, which effectively reduces the attenuation. At 75 kft altitude for the sharp vehicle geometry selected to represent this class, the boundary layer transitions from laminar (smooth) flow to turbulent flow, which increases the peak temperature of the air (and therefore the ionization level) and the heating of the RV. This causes the thickness of the boundary layer to increase by a factor of four or more, causing the RF attenuation to increase dramatically.

Table 1. Data for Plasma Sheath on Sharp Cone

Stagnation Region ^a								
Altitude ft	ω_c/\sqrt{B} per gauss	ω_p rad/sec	ν collision/sec	σ mho/m	u m/sec	σu mho/sec	δ cm	N_{e3} cm ⁻³
250	8.8×10^{-3}	1.77×10^{11}	2×10^9	140	---	---	---	10^{13}
200	1.25×10^{-3}	5.22×10^{11}	1.41×10^{10}	170	---	---	---	9×10^{13}
150	2.3×10^{-4}	1.51×10^{12}	7.6×10^{10}	270	---	---	---	7×10^{14}
100	3.2×10^{-5}	4.97×10^{12}	5.6×10^{11}	390	---	---	---	8×10^{15}
50	5.5×10^{-6}	4.46×10^{12}	3.2×10^{12}	55	---	---	---	8×10^{15}
Flank Region ^a								
250	0.28	3×10^9	6.3×10^7	1.4	3500	4900	5	3×10^9
200	0.0354	10^{10}	5×10^8	1.8	3600	6500	1.5	3×10^{10}
150	6.4×10^{-3}	3×10^{10}	2.75×10^9	2.4	3600	8600	0.6	3×10^{11}
100	8.4×10^{-4}	7×10^{10}	2.1×10^{10}	2.3	3500	8100	0.2	1.6×10^{12}
50	1.3×10^{-4}	4.3×10^{10}	1.3×10^{11}	0.12	2800	340	0.08	6×10^{11}

^aThe data are for a semivertex angle of 10 deg, a wall temperature of 2,000K, and an ICBM trajectory with a velocity of 23.5 kft/sec at 150 kft alt. [Fuhs, 1963].

Steiger et al. [1970] have also summarized the characteristics of reentry flow fields. In the case of slender, conical reentry vehicles, these authors report that electron production can occur in the nose region of blunted vehicles or on the conical portion of the body as a result of viscous dissipation. In the case of sharp nose vehicles, viscous dissipation causes the temperature and, therefore, the chemical production of electrons increases with distance from the apex until an equilibrium condition is reached. However, for increased bluntness, electron production occurs in the stagnation region, and the subsequent behavior of the electron density level about the body is a decay, rather than the aforementioned rise for sharp nose vehicles. The electron levels for blunted and sharp nose bodies do approach each other at downstream distances.

A sharp, slender conical vehicle on a nonlifting ballistic trajectory would not be a candidate for commercial transportation. However, sharp-tip geometries were evaluated in this study because small sharp-tipped cones, with antennas, positioned to protrude through the plasma layer could be mounted on reentry vehicles of various configurations, to provide a means of communication during periods where blackout might occur if the antennas were mounted directly on the body. This approach is addressed in Section 2.1.3.

Steiger et al. [1970] reported that high altitude telemetry blackout was experienced on a fairly sharp, slender reentry vehicle. The vehicle was a sphere-cone with a 0.25-inch nose radius, an 8-degree cone half-angle, with a clean nosetip and heatshield, and an X-band circumferential ring antenna at about the five-inch station. Telemetry plasma attenuation appeared around 190 kft and increased until blackout at about 145 kft. An analysis indicated that the signal degradation was due to plasma attenuation with pattern distortion, resulting from the small look angle, as the main contributor.

Steiger et al. indicated that effects of ablation species on electron production would be substantial, in addition to causing changes in gross flow characteristics such as temperature, velocity, and boundary layer thickness. Ablation also leads to complicated chemical kinetics. However, since electron production is a consequence of trace alkali impurities in the ablative material, a general practice is to consider only the influence of sodium on the electron number density. In the nose region, the effect of sodium is minimal due to the high electron density produced by the bow shock. The diffusion of electrons on the conical portion of the body leads to the following relation for peak electron density decay along the length of the body:

$$N_{e_{\text{peak}}} \propto N_{e_0} \rho_{\infty}^{1/2} R_N^m / x^n \quad (1)$$

Where $N_{e_{\text{peak}}}$ is the peak electron density, and N_{e_0} is a characteristic electron density in the stagnation region and a function of free-stream velocity (v_{∞}) and proportional to the free-stream density (ρ_{∞}). R_N is the nose radius, x the distance along the body, $m = 3$, and $n = 1.5$ to 2.5 [Steiger et al. 1970].

The analysis by Steiger et al. indicated that a substantial reduction in plasma attenuation can be achieved by sharpening the nose radius or by moving the antenna to a more aft location. The first method of alleviation was recommended. Equation (1) indicates that by reducing the nose radius by a factor of 2.5, the telemetry link will perform above the required performance level for an additional 35 kft. Although the effect of sharpening the nose had not previously been substantiated experimentally, the method worked well on a flight. The effect of reducing the nose radius on the plasma properties is shown in Figures 2 and 3.

An extensive body of plasma attenuation data exists at VHF. For example, Figure 4 presents data for similar vehicles, with the same antenna location, but with different nose radii. The 0.25-inch nose radii data consist of a compilation of about five flights. Comparison between theory, which uses a plane wave approximation, and data is reasonably good.

2.1.2 Blunt Cones

A large amount of relevant data was collected during NASA's Radio Attenuation Measurements (RAM) project for blunt-cone bodies. This project included specific measurements of blackout attenuation [Grantham, 1970]. The goals for project RAM were to verify attenuation theory and ground test data with flight data, study ionization effects for various antenna designs, develop flight plasma profile measurement techniques, and study blackout alleviation techniques. A total of eight flights were made over the duration of the project. Of particular interest are the three flights in the RAM C series. A schematic of the RAM C vehicle is shown in Figure 5 [Rybak and Churchill, 1971], and the RAM C reentry flight trajectory (with blackout regions noted) is shown in Figure 6 [Grantham, 1970]. The RAM vehicles had a conical cross-section (half-angle of 9°) with a blunted nose (radius of 6 inches). The overall vehicle length was 41 inches. Figure 6 shows that the onset of ionization blackout was approximately 277 kft for VHF and lasted until roughly 80 kft altitude (32 seconds of flight time). The flow field for this configuration consists of a nearly normal bow shock

wave at the vehicle nose that becomes an oblique shock along the length of the body. A thin boundary layer develops very close to the surface where the majority of aerodynamic heating occurs. The abrupt end of the vehicle causes a turbulent wake to form downstream. The flow of molecules through the shock wave results in large temperature increase, which leads to ionization and the subsequent creation of a plasma sheath surrounding the vehicle body.

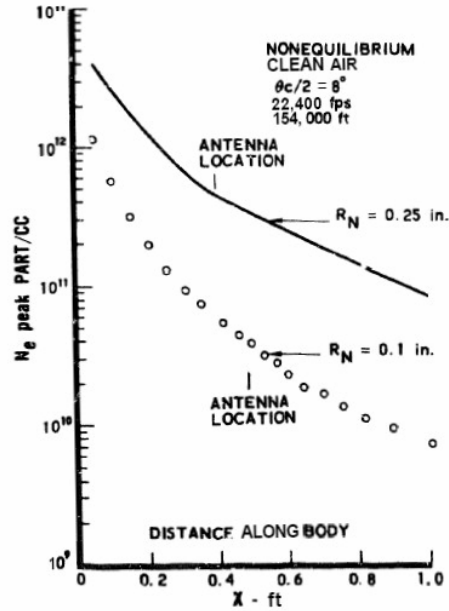


Figure 2. Clean air peak electron density decay. [Steiger et al., 1970].

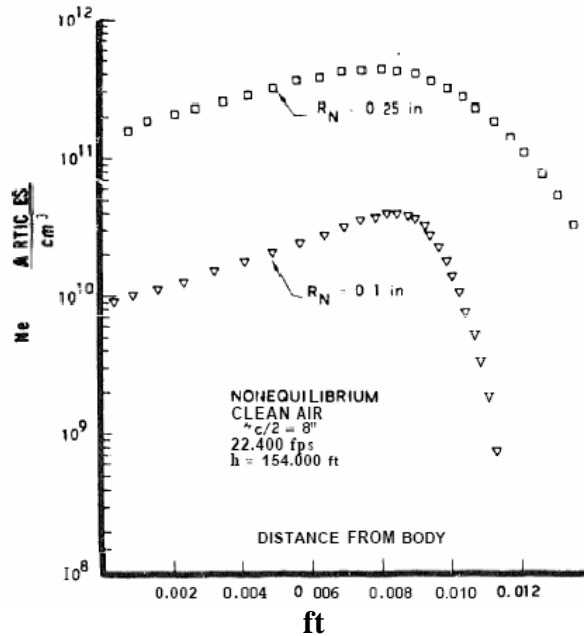


Figure 3. Electron density profile at X-band location. [Steiger et al., 1970].

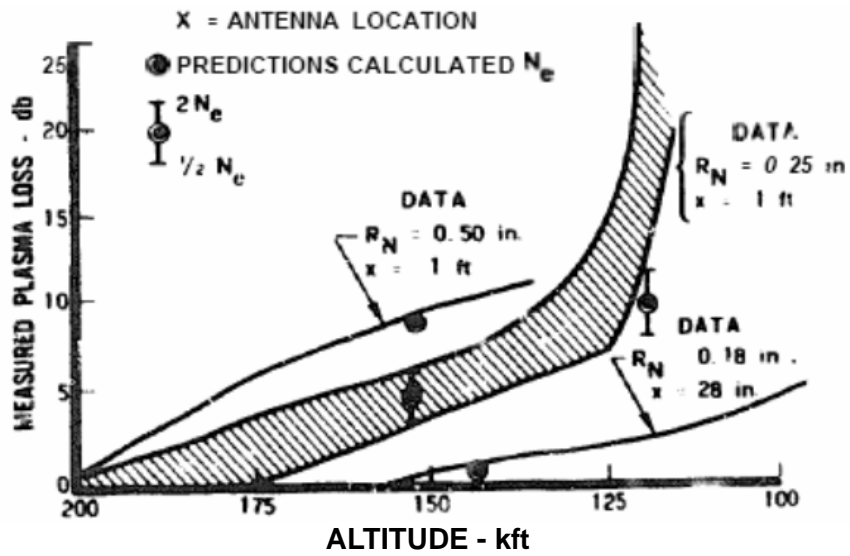
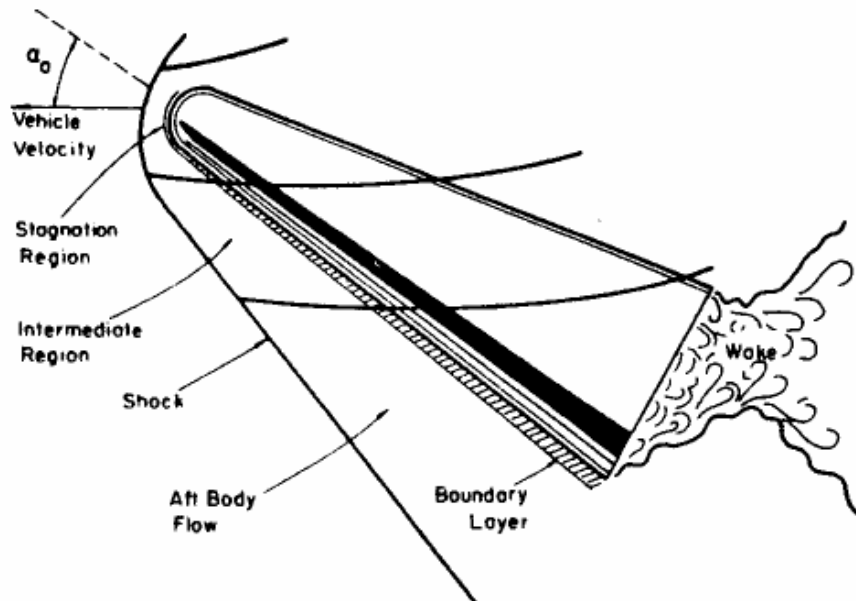


Figure 4. VHF attenuation. [Steiger et al., 1970].



© 1971 IEEE

Figure 5. Schematic of RAM C vehicles and reentry flow characteristics [Rybak and Churchill, 1971].

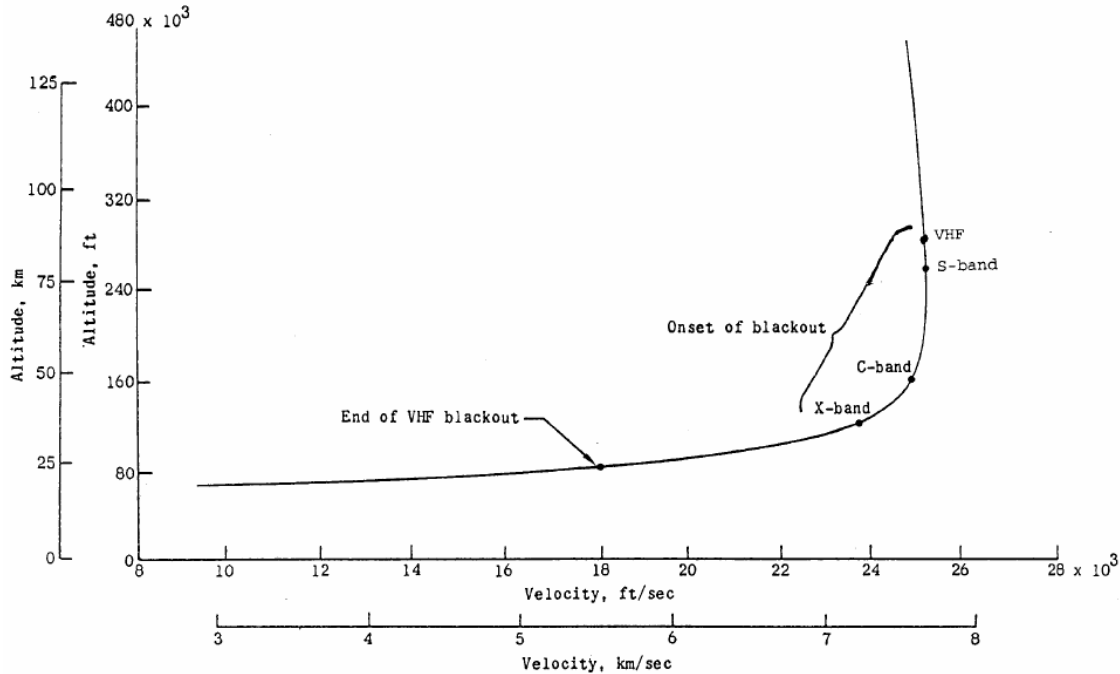


Figure 6. RAM C-II reentry trajectory showing onset and end of RF signal blackout. X-band and C-band reacquisition were delayed because of tracking difficulties. [Grantham, 1970]. (Reprinted courtesy of NASA).

Data collected during the RAM C second and third flights provided invaluable insight into the plasma behavior of conic bodies traveling at reentry velocities. Electrostatic probes were incorporated into the vehicle design to expressly measure the in-flight electron density distribution between the body surface and oblique shock wave at a variety of locations and altitudes. Results of the measurements were reported by Huber et al. [1971]. In conjunction with the flight measurements, analytical studies were performed to develop prediction capabilities for future programs and missions.

Dunn and Kang [1973] developed an analytical model applicable to reentry plasma flow fields for blunt cones. Based on previous work by Kang [1970] and Blottner [1969], the technique models the nonequilibrium flow as a viscous, ionized shock layer around the body surface. Dunn and Kang applied the method to the RAM C-II and RAM C-III flight data between the altitudes of 230 kft and 275 kft for validation. Figure 7 illustrates the results of the analytical technique as compared with electron density data for both RAM C flights. As can be seen in the figure, acceptable agreement was obtained with respect to the experimental uncertainty. Figure 8 shows the measured electron temperature as compared to the computed translational temperature for the model heavy species. This result confirms that the model kinetics assumptions are appropriate, since the translational temperature was assumed equal to the electron temperature in the model derivation. The uncertainty of the chemical reaction rate coefficients within the model were analyzed and found to be within the range of experimental uncertainty as well.

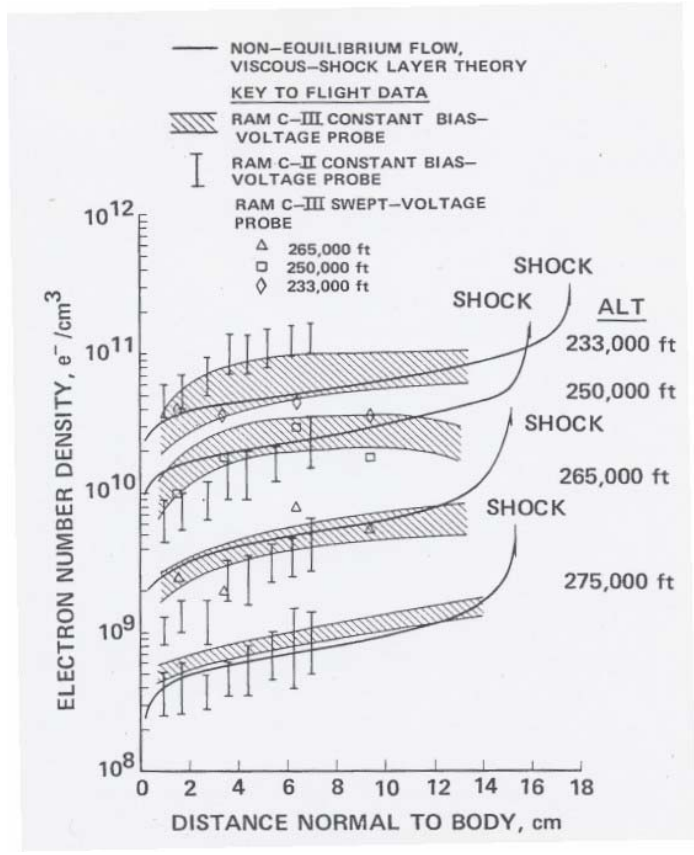


Figure 7. Comparison of measured and predicted electron density for RAM C flights. [Dunn and Kang, 1973]. (Reprinted courtesy of NASA).

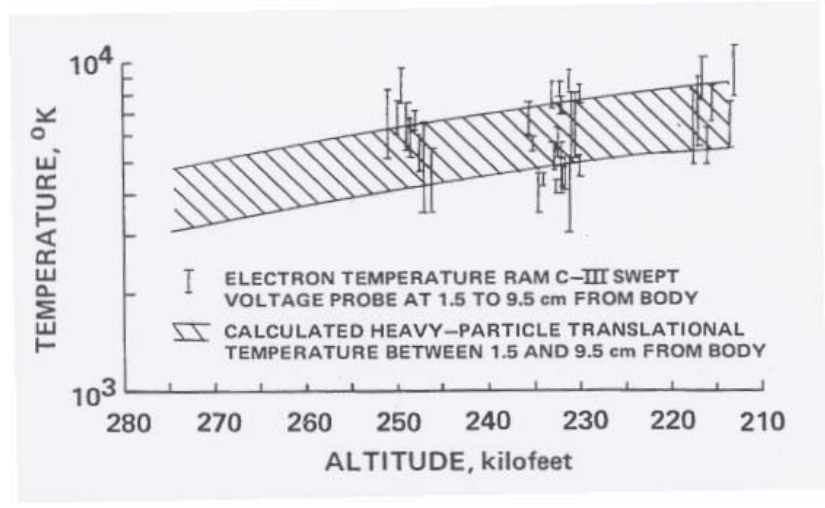


Figure 8. Comparison of measured electron temperature to predicted translational temperature for RAM C flights. [Dunn and Kang, 1973]. (Reprinted courtesy of NASA).

Schexnayder et al. [1970] performed further analytical work for RAM C flights focusing on lower altitudes. For an altitude range between 60 and 250 kft, these authors used a number of different models to describe the plasma flow field and compare it with measured values. Discussion is presented by these authors on the applicability of each model based on the assumptions made and characteristics of the flow itself. The models were found to agree for altitudes above 125 kft but not as well at lower altitudes. These authors also noted that electron density distributions measured below 200 kft were significantly affected by ablation and subsequent ionization of heat shield material during the RAM C-I flight.

2.1.3 Blunt Cones with Sharp Tip

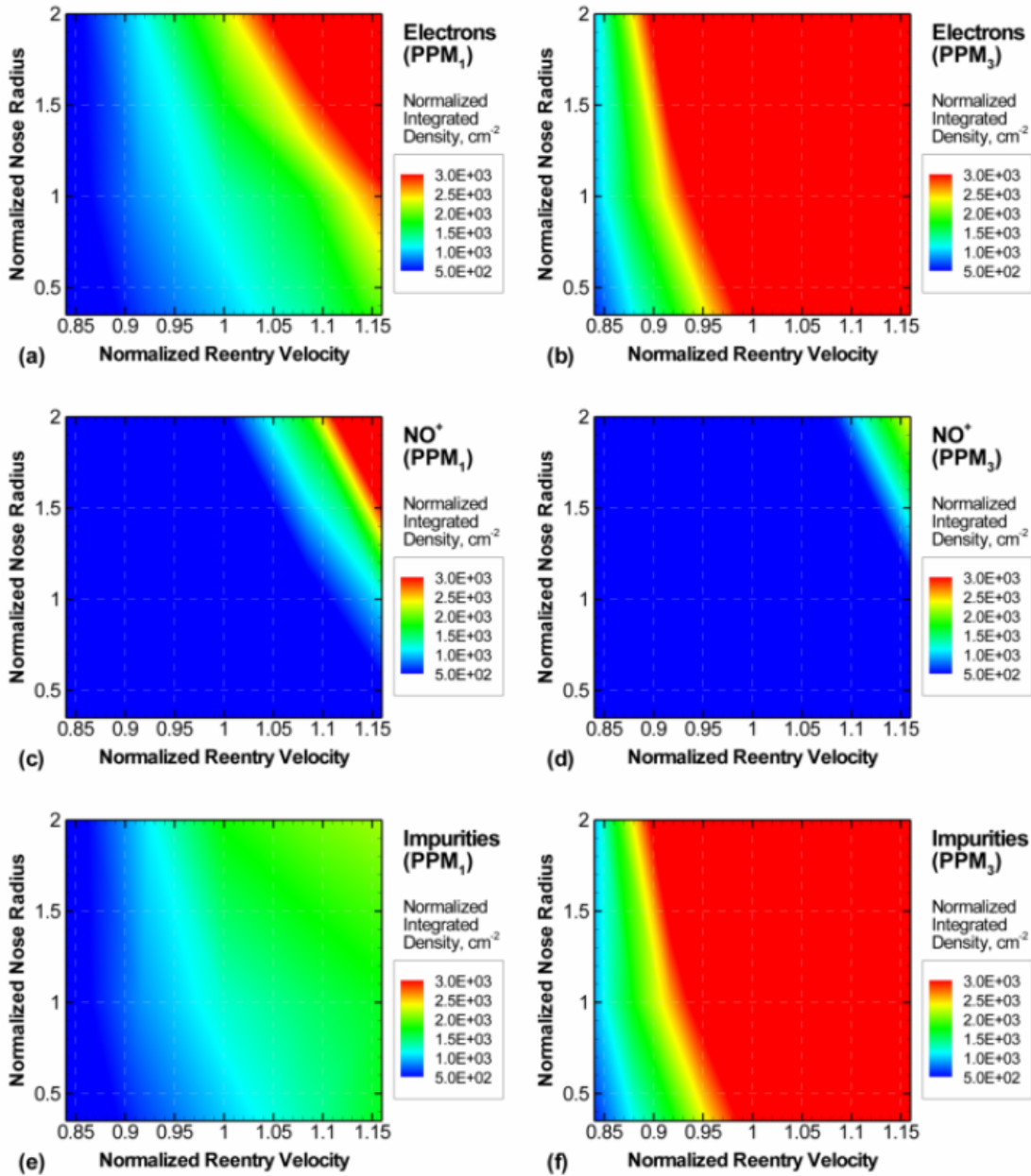
A large body of work was done in Russia [Belov et al., 2001] on blunt-cone vehicles with sharp tips. This configuration consists of a slender probe being extended in front of the main vehicle body with an attached antenna. By placing the antenna ahead of the vehicle body shock front, the antenna may escape significant attenuation, allowing for continuous direct communication with the main vehicle. At this time, Aerospace has not evaluated the impact of this work in sufficient depth to validate it, but it looks promising since the authors addressed most of the concerns one would raise, e.g., shock interactions and their effect on heating rates to the blunt body and the slender probe, as well as a detailed evaluation of the effect the probe would have on the aerodynamics of the vehicle. The sharp conical tip of the probe is actively cooled by injecting pressurized air through the porous sintered metal. Future efforts should include a detailed evaluation of this design option.

2.1.4 Plasma Level Variations with Vehicle Nose Radius and Heat Shield Impurity Levels

Mather et al. [2005] have reported that significant plasma generation mechanisms include (1) bow shock ionization that occurs in the stagnation region at the nose of the vehicle and (2) ablation of the heat shield, producing easily ionizable impurities, caused by heat transfer at the wall along the frustum of the vehicle. The bow shock plasma generation is greatly affected by the vehicle nose radius. The primary species produced through this mechanism is NO^+ and its free electron, which flow downstream and recombines along the length of the body. The ablation plasma is dominated by various positive ions arising from impurities in the heat shield. This plasma varies with wall and boundary layer temperature along the length of the body.

Mather et al. also report that the vehicle shape influences major plasma mechanisms: The production of NO^+ in the stagnation region is directly related to the vehicle nose radius. In particular, larger nose radii give rise to a larger bow shock region, which increases the level of air ionization at the nose. At the same time, these larger stagnation regions yield higher temperature boundary layers as the shock layer expands downstream along and around the body. In turn, the rate of ablation increases with nose radius as well. Figure 9 shows the integrated densities of electrons and positive ions over ranges of normalized reentry velocities (V) and nose radii (R_N) (with interpolation across these ranges). In general, vehicles with blunter nosetips moving at higher velocities generate larger levels of both NO^+ [shown in (c) and (d)] and ablation ions [shown in (e) and (f)] in Figure 9. As a result, the plasma levels exhibit a similar trend [shown in (a) and (b)]. Note that these calculations are at the rear frustum and an altitude of 50 kft, and so ablation is clearly the dominant mechanism for plasma generation.

Whereas the vehicle nose radius influences both plasma mechanisms via the bow shock, the level of impurities in the vehicle heat shield only directly affects the ablation products.



(a) integrated electron density at PPM₁ impurity level, (b) integrated electron density at PPM₃ impurity level, (c) integrated NO⁺ density at PPM₁ impurity level, (d) integrated NO⁺ density at PPM₃ impurity level, (e) integrated impurity density at PPM₁ impurity level, (f) integrated impurity density at PPM₃ impurity level.

Figure 9. Variation of electrons and positive ions (NO⁺, Impurities) with vehicle nose radius and heat shield impurity level for 0° angle of attack (AoA) at rear frustum and 50 kft altitude. [Mather et al., 2005].

That is, an increased level of impurities yields larger concentrations of ablation ions that contribute to the plasma level. This effect is clearly shown in Figure 9, where the increase in impurity level,

expressed in parts per million (PPM), from PPM₁ to PPM₃, gives a significant increase in the ablation ions [comparing (e) and (f)] and a corresponding rise in electrons [compare (a) and (b)].

The concentration drop of NO⁺ as the impurity level increases from PPM₁ to PPM₃ [compare (c) and (d)] is evidence of interactions between the NO⁺ and ablation ions within the chemically reacting boundary layer. Since the flowfield conditions are similar for a given velocity and nose radius, the amount of air ionization at the nose region is the same regardless of the heat shield impurity level. However, the nose-generated NO⁺, which is present at non-equilibrium levels at the nose, can recombine at a much faster rate in the presence of various ablation ions from the two mechanisms.

2.2 Commercial ELV and RLV Concepts

Commercial ELVs and RLVs represent the future of space applications. Two enterprises currently developing commercial launch vehicles are Rocketplane Kistler, Inc. (RpK) and Space Exploration Technologies Corp. (SpaceX). If successful, these companies will significantly reduce overall launch costs, potentially leading to large numbers of orbital vehicles operating at any given time. RpK intends to produce a two-stage RLV with a first-stage flyback and a reentering second stage (Fig. 10). The SpaceX Falcon I and V first stages return by parachute to a water landing, while the second stages are expendable. On August 18, 2006, RpK received a \$207M award from NASA under the Commercial Orbital Transportation Services (COTS) demonstration program to help complete the K-1 reusable rocket and develop a cargo module that could later be modified to carry astronauts to the International Space Station (ISS). Simultaneously, SpaceX received a \$278M award from NASA under the COTS program to support funding of the development and flight demonstration of Dragon, a ballistic capsule launched atop the SpaceX Falcon 9 rocket currently in development. SpaceX intends to later modify Dragon to carry astronauts to the ISS.

Prior to the COTS award, RpK, a private enterprise, had been developing its low-cost two-stage launch vehicle, the K-1, primarily using private funds. The vehicle is designed to be fully recoverable. The first stage flies to an altitude of 142 kft and a velocity of 4 kft/sec. It separates from the second stage with its engines off, then the center engine of three re-ignites after 4.4 seconds and flies back to the launch site following a ballistic trajectory. Two drogue parachutes and two clusters of three main chutes are used to decelerate the first stage for a soft landing on four air bags.

The K-1 second stage Orbital Vehicle (OV) goes to orbit, delivers the payload, resides in a circular orbit until the proper time to de-orbit, and reenters the atmosphere at 25 kft/sec. It descends using a lifting bank angle to follow the autonomous guidance system's instructions to return to the launch site. At Mach 2.5, a stabilization chute deploys, followed by a drogue chute pulling three main chutes, which decelerate the OV for a soft landing using four air bags.



Figure 10. Artist's conception of RpK K-1 reentry vehicle (Illustration reprinted courtesy of Kistler).

Figure 11 shows that the OV is a large very blunt-nosed cylinder with a large flare at its aft end. The nose radius is 165.3 in., and a 25.5 in. radius is used to transition from the nose to the cylinder. A 27.9 in. radius curve fills the cylinder flare junction. The 14 ft. diameter of the blunt nose is somewhat larger than the Apollo Command Module. Table 2 gives weights of the components.

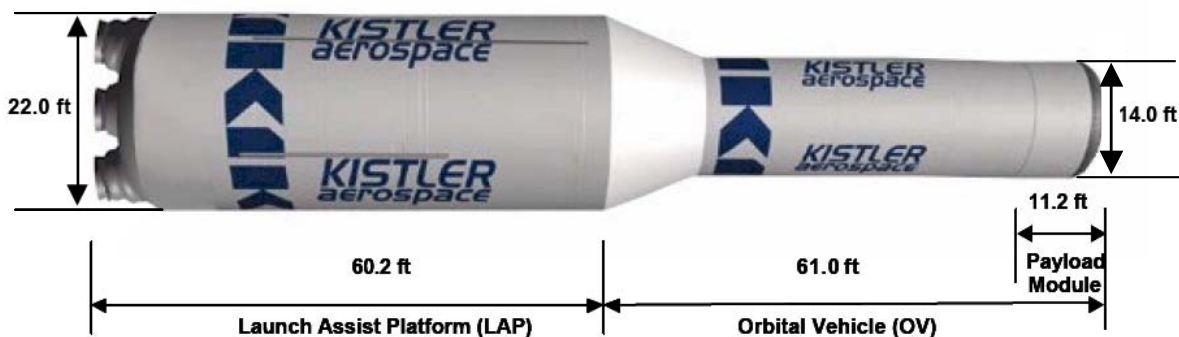


Figure 11. K-1 vehicle profile (Illustration reprinted courtesy of Kistler).

Table 2. K-1 Gross Liftoff Weight (GLOW) Summary (lbm).
[Kistler, 2002].

Launch Assist Platform (LAP)	551,000
Orbital Vehicle (OV)	290,000
K-1 Gross Liftoff Weight	841,000

Figures 12 and 13 show plots of the reentry trajectory for the K-1 OV. Determination of the ionized flow field around this vehicle was beyond the scope of this phase of work because it would involve

exercising complex codes. Furthermore, it would necessitate contacting the contractors to acquire information on the angle of attack history on descent, which affects the flow significantly.

Figure 14 compares blackout trajectories and times for reentry of the Shuttle, the RpK OV, the RAM C, and hypothetical sharp-tipped RVs. The authors compared the OV trajectory to that of the Space Shuttle and found that this vehicle retains considerably higher velocity at each equivalent altitude (Figure 14). For example, at 200 kft altitude, the Shuttle and OV velocities are 17.5 and 22.5 kft/sec, respectively. At 150 kft altitude, the Shuttle and OV velocities are 6.0 and 17.5 kft/sec. Whereas the Shuttle experiences blackout onset at 265 kft and recovers at 162 kft, the OV would be expected to have the same onset altitude (they are both at 25 kft/sec), but would recover from blackout much lower, at approximately 130 kft. Velocity is the major determinant of the maximum temperature in the flow field, and temperature is the major determinant of degree of ionization in the flow.

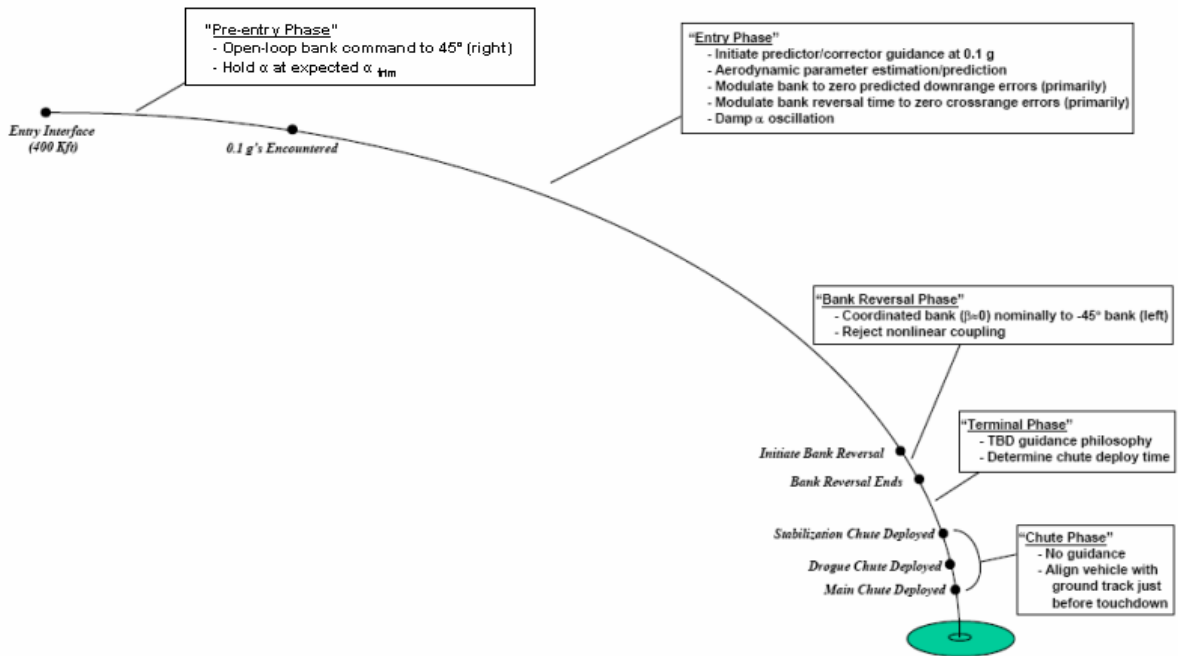
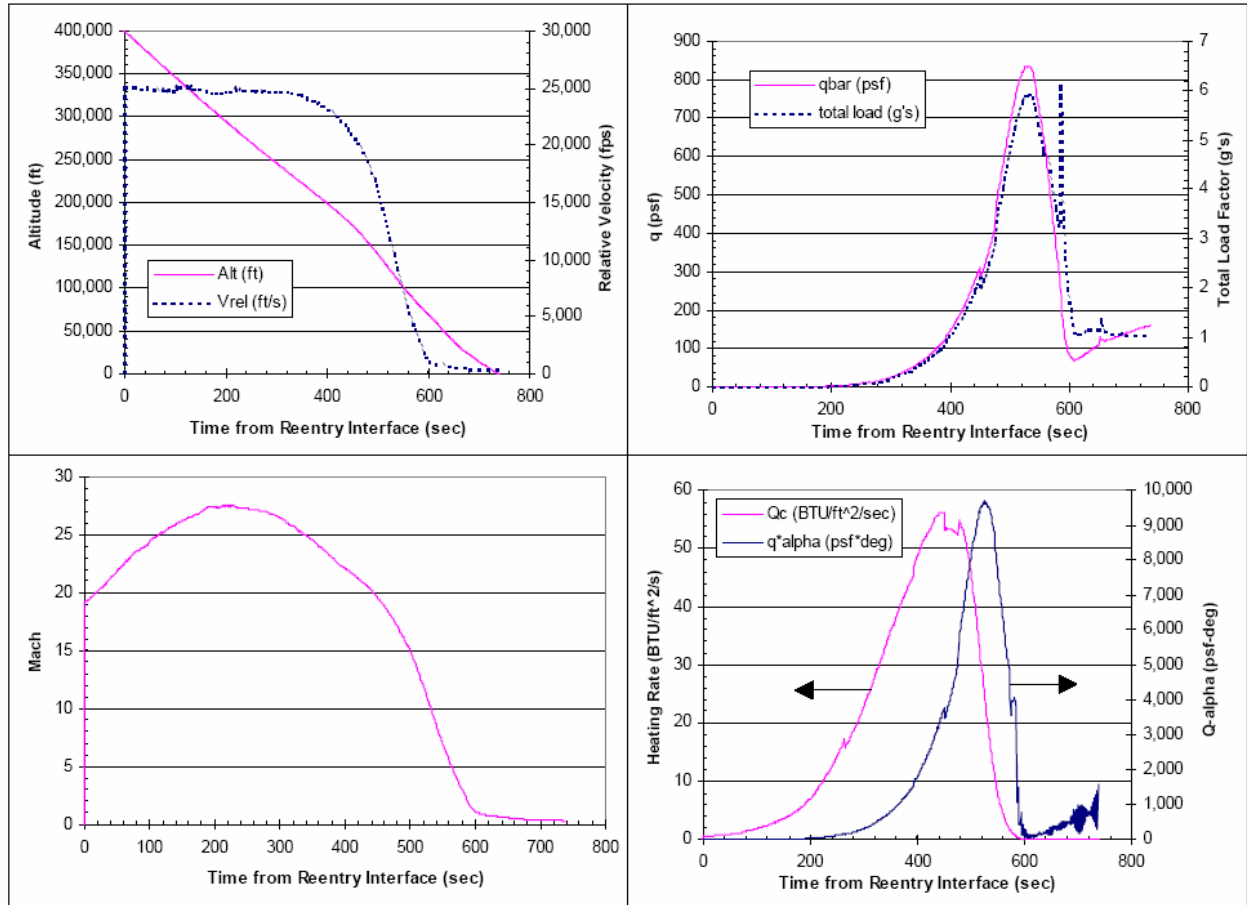
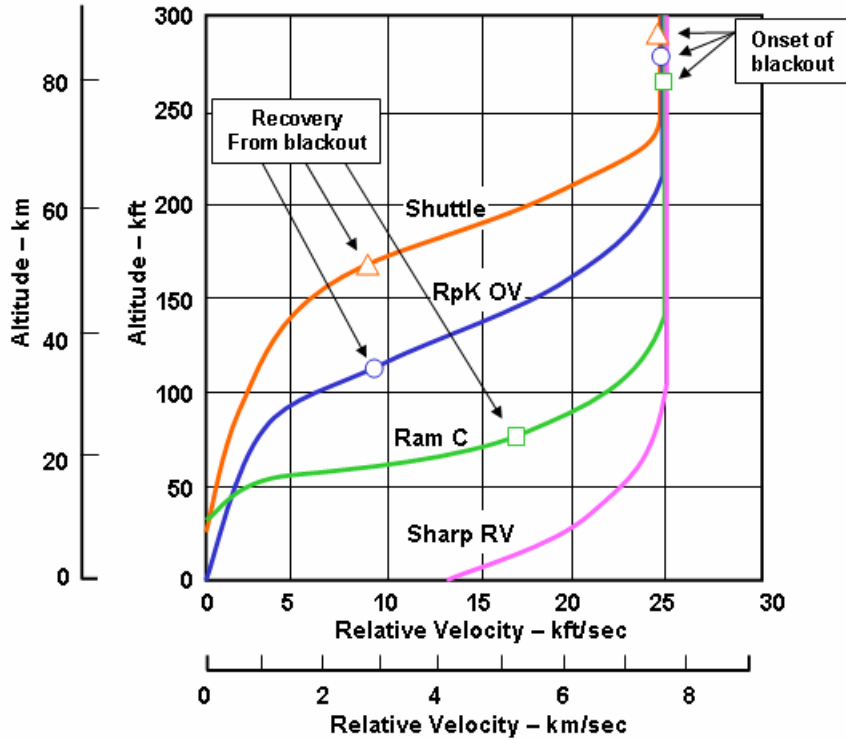


Figure 12. K-1 orbital vehicle reentry profile. [Kistler, 2002]. (Reprinted with permission of Kistler).



q_{bar} = dynamic pressure; Q_c = heat flux; α = angle of attack

Figure 13. Typical K-1 OV reentry trajectory. [Kistler, 2002]. (Reprinted with permission of Kistler).



Vehicle	Blackout duration, minutes
△ Shuttle	16
○ RpK OV	1
□ Ram C	0.5
Sharp RV	0

Figure 14. Blackout trajectories and times for reentry of Shuttle, RpK OV, RAM C, and sharp-tipped RVs.

2.3 Unpowered Lifting Glide Vehicles

Significant data are available on the reentry characteristics of unpowered lifting glide vehicles because of NASA's manned space program. For this study, unpowered lifting glide vehicles are vehicles that do not produce active thrust during the reentry or cruise phase, but do generate a significant amount of lift. For orbital systems, this design choice stems from the desire to limit the maximum vehicle deceleration during reentry for manned mission safety with a prolonged hypersonic glide. For the most part, these vehicles are recognized by the presence of wings and associated control surfaces.

The following sections examine the plasma flow fields of unpowered lifting glide vehicles. Particular attention is paid to the Space Shuttle orbiter, because of the large quantity of design and flight data available. Discussion of other vehicle designs is included but limited by sparse available flight data.

2.3.1 Space Shuttle Orbiter

After the successful conclusion of the Apollo program, NASA determined that a reusable manned platform was desirable to reduce launch hardware cost. In response, the semi-reusable Space Shuttle Orbiter vehicle was designed and tested. Over the course of more than twenty years of flight history, the Shuttle provided a wealth of data on plasma flow fields and operational experience with communication blackout issues. A representative drawing of the Space Shuttle Orbiter reentry configuration is shown in Figure 15.



Figure 15. Drawing of Space Shuttle Orbiter during reentry conditions. (Drawing reprinted courtesy of NASA).

Like the previous Apollo capsules, the Shuttle design was expected to experience communication blackout for a significant duration of the reentry flight. Figure 16 shows the known blackout event history for the Space Shuttle Orbiter. Onset of communication blackout was found to occur at approximately 265 kft and last through 162 kft altitude for total time duration of about 16 minutes. A practical solution to maintain Shuttle communication throughout reentry was established through the use of the Tracking & Data Relay Satellite System (TDRSS) satellite constellation. Placement of antennas on the upper surface of the Orbiter enabled uninterrupted communication via the TDRSS satellite downlink during the period of the trajectory when the antennas on the lower surface were blacked out.

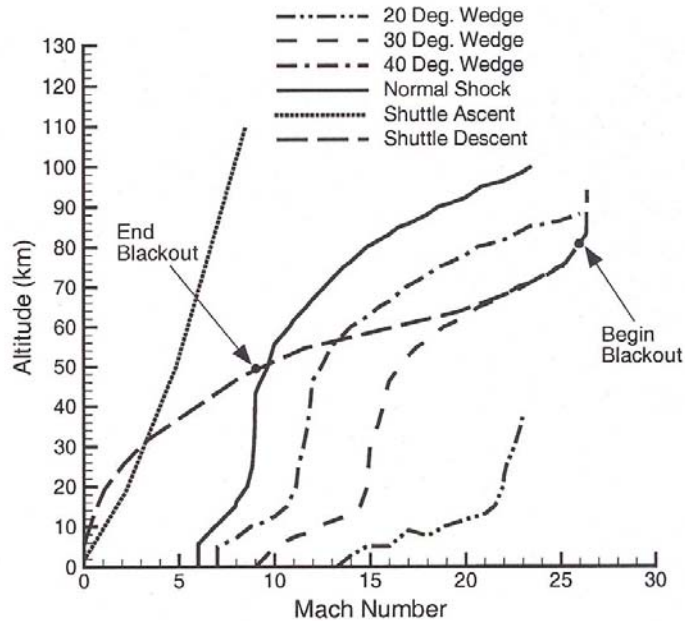
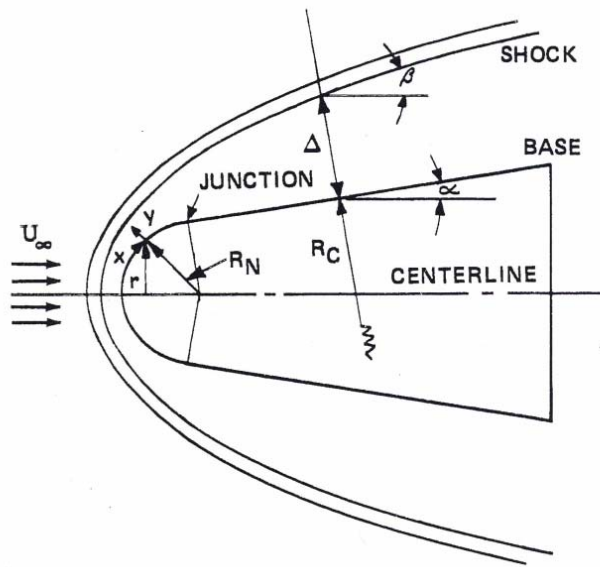


Figure 16. Typical Space Shuttle reentry trajectory. [Starkey, 2003]. (Reprinted with permission of the American Institute of Aeronautics and Astronautics, Inc.).

Numerous analytical and experimental studies were performed to define the communication blackout region expected during Shuttle reentry. Of particular relevance was a study performed by Dunn and Kang [1973] for a shuttle-like configuration and reentry trajectory. This study focused on approximating the lower surface of the Shuttle body where S-band antennas for voice communication are located. Using the same technique applied to the RAM experimental data (see Section 2.1.2), Dunn and Kang predicted the plasma flow field around a four-foot-radius hemisphere with adjoined 20° cone. A schematic of the body shape is shown in Figure 17. Since the Shuttle nose closely resembles a hemisphere with a radius of approximately four feet, qualitatively, the flow field around the nose and lower surface of the Space Shuttle resembles that of a blunted cone. Free electrons are produced by the strong shock wave and form a sheath around the Shuttle's lower surface, blocking communication. The reentry trajectory used in the study (see Figure 18) is remarkably similar to typical Shuttle trajectories, as shown in Figure 16, differing mainly in the vehicle angle of attack. Dunn and Kang assumed a 20° angle of attack (AoA), whereas the Shuttle reenters at 40°. By virtue of similarity, Aerospace considers the study done by Dunn and Kang as an acceptable preliminary result for the plasma flow field around the lower surface of the Space Shuttle Orbiter.



U_{∞} = free stream velocity; Δ = shock standoff distance

Figure 17. Schematic flow field. [Dunn and Kang, 1973]. (Reprinted courtesy of NASA).

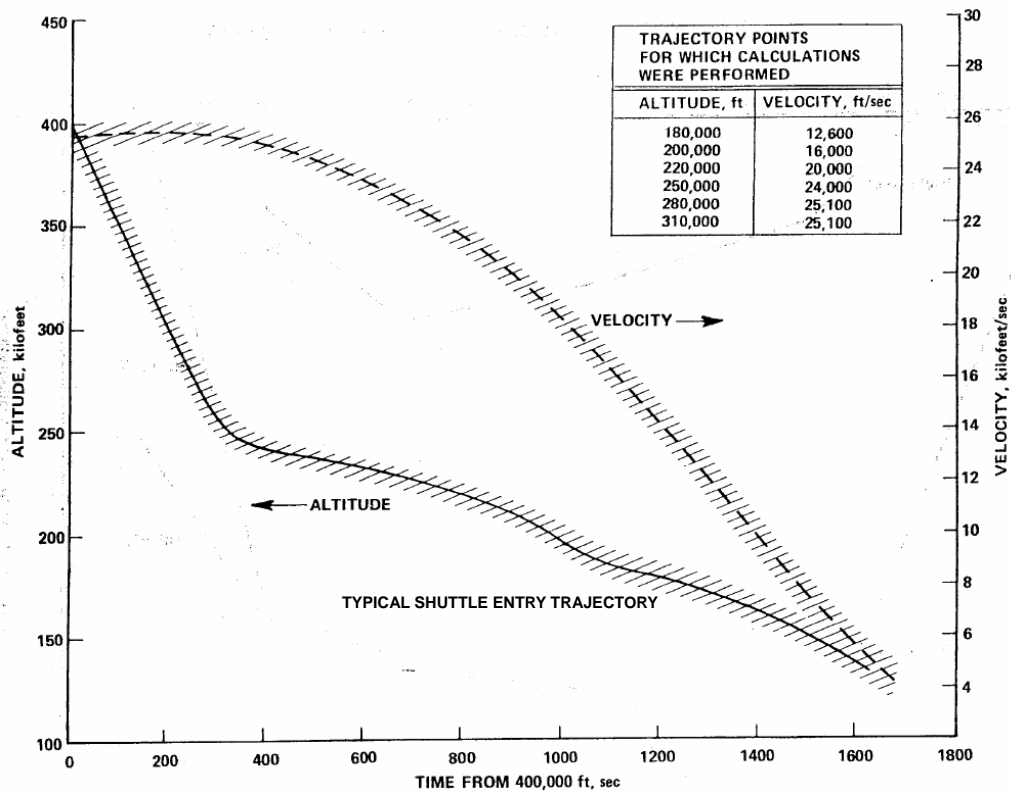
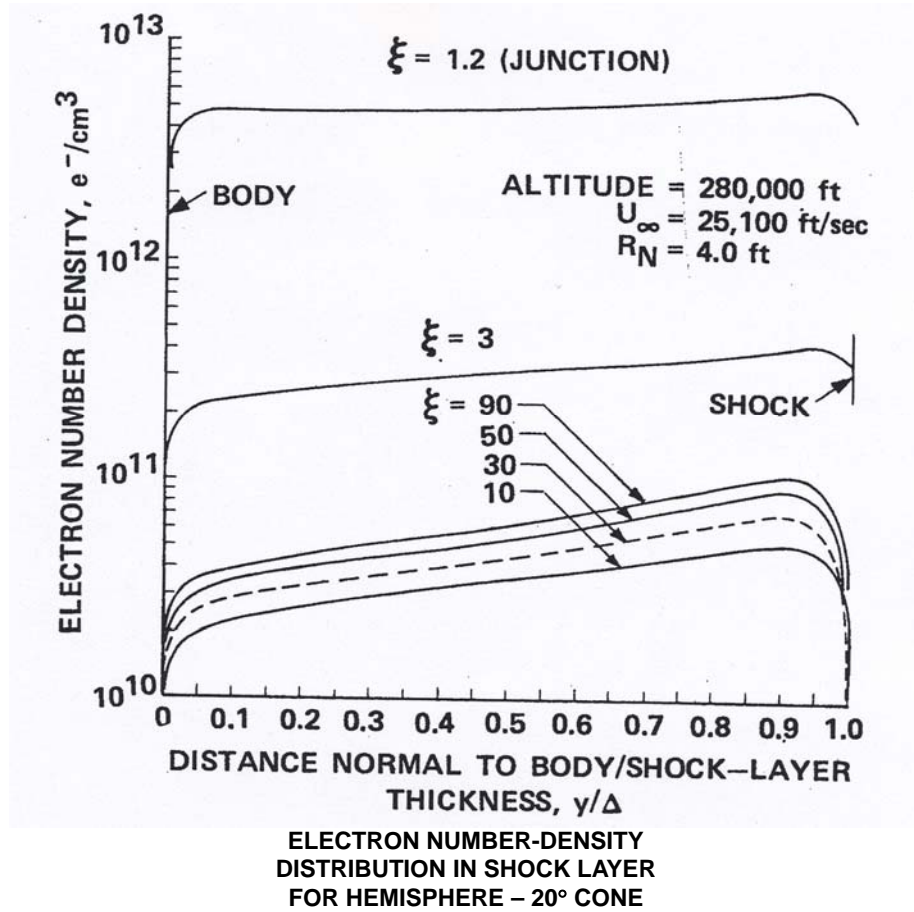


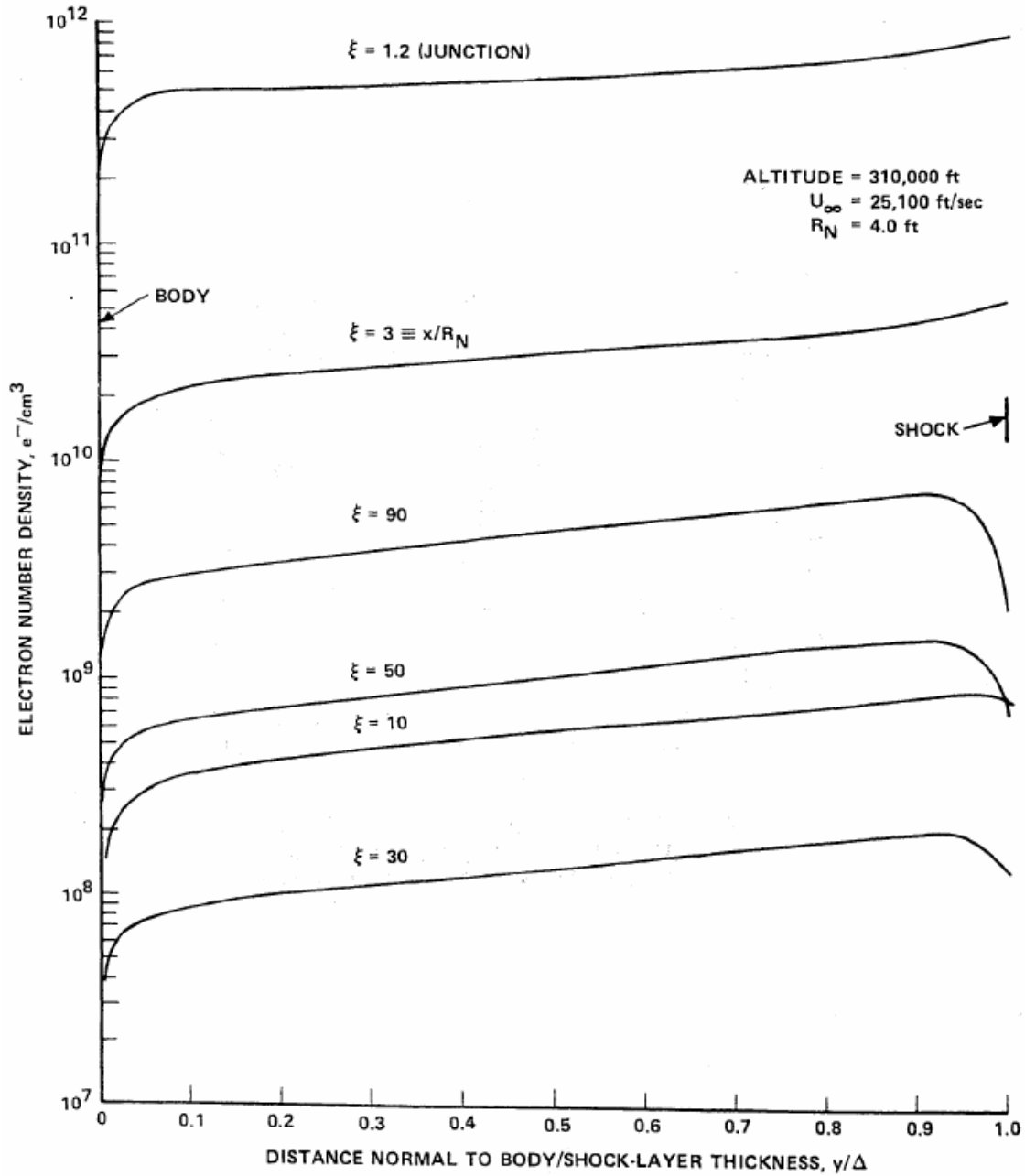
Figure 18. Assumed Space Shuttle trajectory. [Dunn and Kang, 1973]. (Reprinted courtesy of NASA).

Results of the numerical study by Dunn and Kang at a variety of altitudes and vehicle locations are shown in Figures 19 and 20. Figure 19 presents the electron density profiles found for the vehicle at an altitude of 280 kft, and Figure 20 represents a vehicle traveling at 310 kft, respectively. In each of these figures, ξ is the ratio of downstream position to the nose radius, and Δ is the shock standoff distance. As seen in the figures, the electron density tends to increase with distance away from the body surface until reaching the oblique shock found at $\Delta = 1.0$. Also of interest, the magnitude of the electron density decreases to a minimum (~ 10 radii for 280 kft, and ~ 30 radii for 310 kft) downstream of the nose, followed by a slight increase at further stations.



ξ = ratio of downstream position to hemisphere radius
 y = distance normal to body surface (abscissa)

Figure 19. Plasma flow profiles for Shuttle configuration for 280 kft altitude. [Dunn and Kang, 1973]. (Reprinted courtesy of NASA).

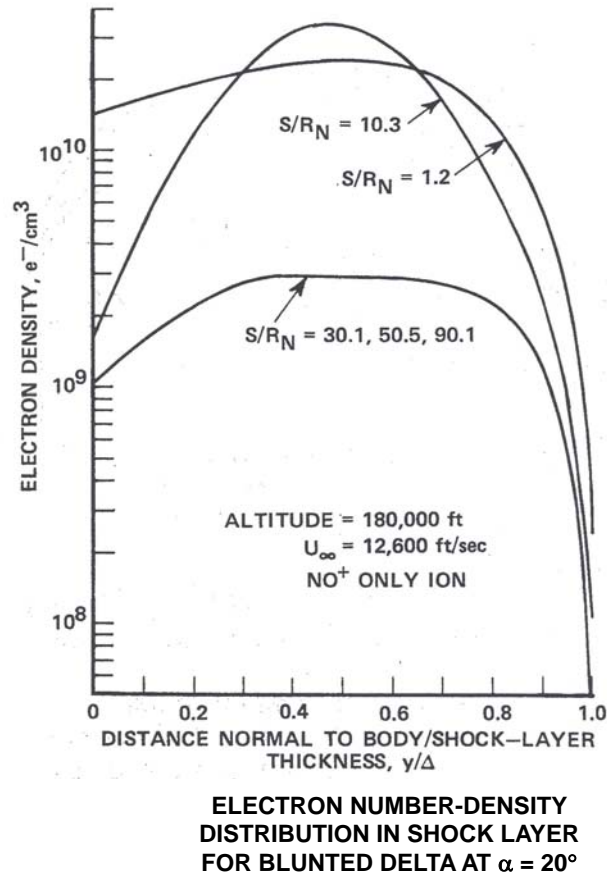


ELECTRON NUMBER-DENSITY DISTRIBUTION IN SHOCK LAYER

ξ = ratio of downstream position to hemisphere radius

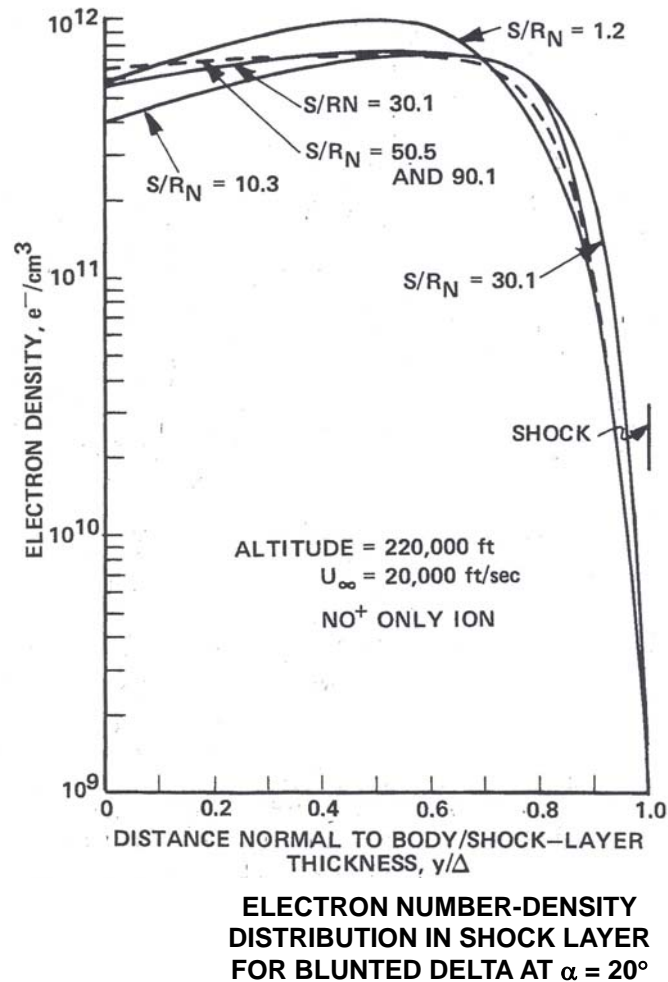
Figure 20. Plasma flow profiles for Shuttle configuration for 310 kft altitude. [Dunn and Kang, 1973]. (Reprinted courtesy of NASA).

Dunn and Kang performed predictions for the lower altitude portion of the Shuttle reentry trajectory as well. The predictions were completed using nonequilibrium flow calculations provided by Lordi et al. [1971] for a blunted delta-wing Orbiter configuration at 20° angle of attack and at altitudes below 250 kft. While somewhat different from the Shuttle platform shape, these results are consistent with the previous work and are considered reasonable for the preliminary nature of the work. Figures 21 and 22 show the predicted electron number density in the viscous shock layer for various body locations at altitudes of 180 kft and 220 kft, respectively. Note these calculations included the effect of NO^+ ions only. The qualitative trends found in Figures 21 and 22 are generally similar to those found previously. Namely, the electron density increases away from the body surface until reaching the shock wave location.



S = distance along surface of body from nosetip (same as x in Figure 17).
 S/R_N equivalent to ξ in Figure 19.

Figure 21. Plasma flow profiles for Shuttle configuration for 180 kft altitude. [Dunn and Kang, 1973]. (Reprinted courtesy of NASA).



S = distance along surface of body from nosetip (same as x in Figure 17).
 S/R_N equivalent to ξ in Figure 19.

Figure 22. Plasma flow profiles for Shuttle configuration for 220 kft altitude.
 [Dunn and Kang, 1973]. (Reprinted courtesy of NASA).

A specially equipped Navy P-3 aircraft was used to acquire imagery and spectral data of hypersonic aerodynamic flow on the belly of the Space Shuttle STS-121 *Discovery* during reentry. Imagery by reentry vehicle tracking optics on the P-3 obtained a unique view of how a minor tile gap-filler protrusion tripped the boundary layer into hotter, turbulent flow during the descent in July 2006. It shows a warmer, lighter shaded, infrared thermal “wedge” signature behind the protrusion, on the somewhat cooler, darker belly (Figure 23). This STS-121 Mach 18 imagery closely paralleled computer projections, giving managers confidence that they can accurately predict additional heating from any future Shuttle belly defects.

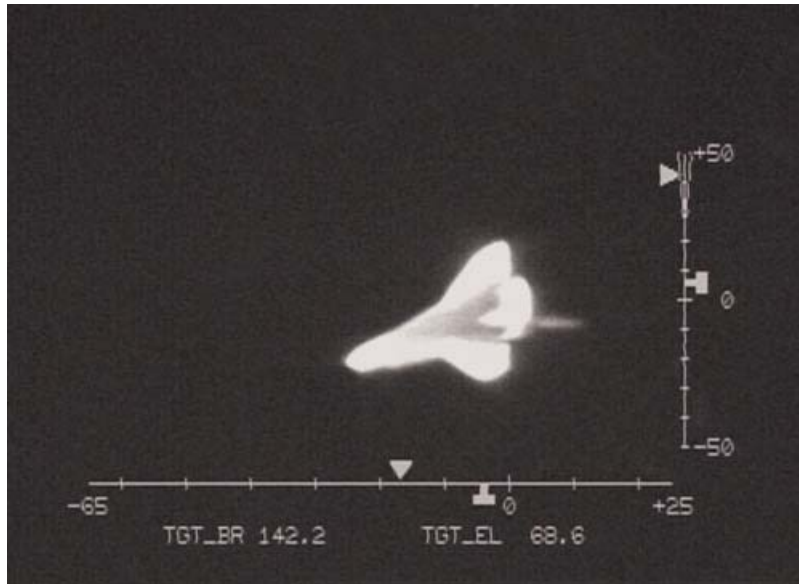


Figure 23. *Discovery* STS-121 hypersonic boundary layer transition from protruding aft gap-filler at Mach 18 reentry, captured by “Cast Glance” optics on Navy P-3 aircraft. (Image reprinted courtesy NASA).

2.3.2 Hypersonic Boost-Glide Vehicle

Hypersonic boost-glide vehicle designs have existed since the beginning of dedicated space programs. While typically designed for military applications, hypersonic boost-glide vehicles operate in the suborbital flight regime. Boost-glide refers to the stages of vehicle flight, where initially a rocket stage propels the vehicle to a cruising altitude and hypersonic velocity, followed by an unpowered cruise trajectory. Variants of this design include atmospheric “skipping” events, where the vehicle repeatedly enters the upper atmosphere to generate lift (and resulting cross-range) for short intervals.

Examples of hypersonic boost-glide vehicles predate NASA’s manned programs. Figure 24 shows a schematic of the Dynasoar vehicle design from 1959. Examination of preliminary design characteristics permits general speculation on the impact of communication blackout on this class of vehicle. In general, the design cruising velocity of this class of vehicle is below Mach 10. Comparison of this velocity to Space Shuttle data, with well defined reentry characteristics, reveals that the Shuttle emerges from communication blackout at approximately Mach 10. Therefore, communication blackout is not expected to occur for hypersonic boost-glide vehicles in general.

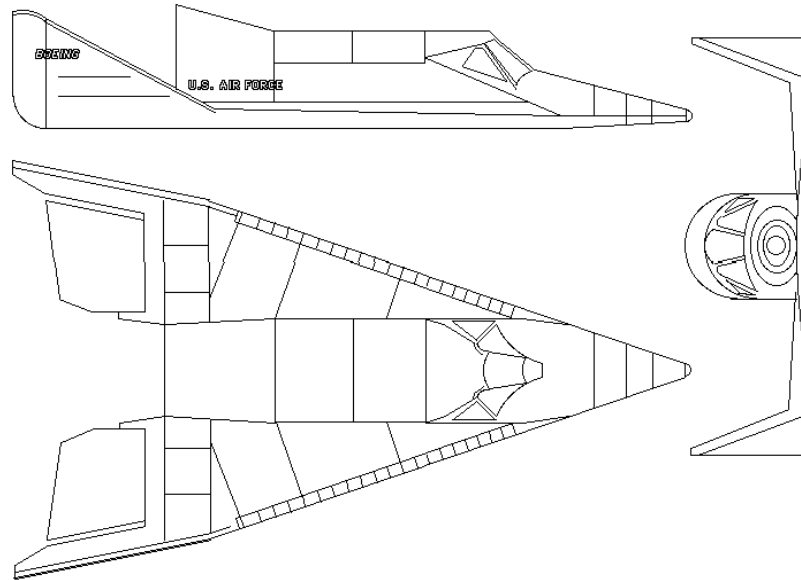


Figure 24. Schematic of Dynasoar design configuration.

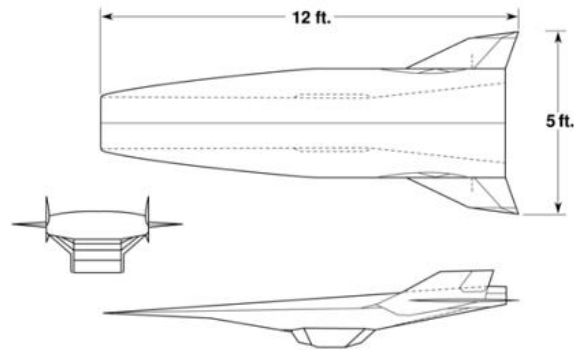
2.3.3 Powered Air-Breathing Hypersonic Cruise Vehicles

Powered hypersonic cruise vehicles were examined for potential communication blackout. Over the last thirty years various designs for hypersonic cruise vehicles appeared, typically in the form of single-stage-to-orbit vehicles with familiar program names such as National Aerospace Plane (NASP) and Aurora. NASA has proposed a new design for a vehicle with continuous hypersonic cruise capability [Orton and Scuderi, 1998]. This vehicle is intended to be a technology demonstrator for air-breathing hypersonic propulsion systems. Known as the X-43, NASA has funded three test flights that are currently under way. The X-43 vehicles, depicted in Figures 25 and 26, were designed to be launched from the nose of a Pegasus rocket at hypersonic speeds prior to engine ignition. The first launch of the X-43A in 2001 was aborted when the vehicle had to be destroyed in flight due to malfunction of the Pegasus booster. The second launch in 2004 was successful and Mach 7 flight was achieved. The program has now been cancelled. Other proposed hypersonic air-breathing vehicles of interest are mainly missile designs for military applications with roughly the same design trajectories noted above. As outlined in the previous section and discussed by Starkey [2003], this range of altitudes and velocities is not sufficient to generate a plasma sheath around the vehicle, making current hypersonic air-breathing vehicle designs unlikely to be affected by communication blackout.

As reflected in the literature, a number of programs have attempted to design vehicles that cruise in the hypersonic regime. To date, none have progressed to the point where full-scale production is imminent. The largest technology hurdle still to overcome is a propulsion system capable of reaching and sustaining hypersonic velocity [Jackson, 2006]. The general community consensus remains that these vehicles are at least one generation away from passenger transport. Looking ahead, current air-breathing hypersonic vehicle designs possess characteristics that allow the following general statements to be made. For instance, as seen in the X-43 design, hypersonic cruise vehicles necessarily will exhibit a relatively sharp leading-edge configuration. This design minimizes the drag

produced by the bow shock wave that precedes the vehicle in flight. Therefore, while not necessarily circular in cross-section, hypersonic cruise designs generally should produce plasma flow fields similar to a sharp-tipped cone for the same velocity and altitude. Given that significant data exist for sharp-tip cone designs, extrapolation to future hypersonic vehicle designs should provide an excellent estimate of plasma sheath characteristics.

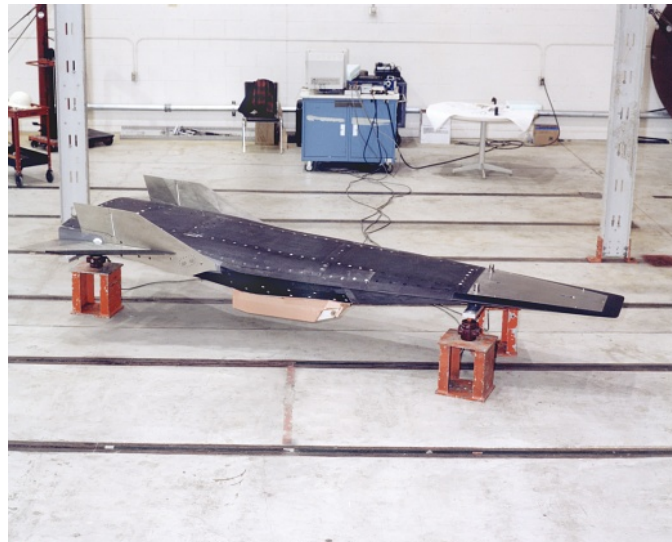
HYPER-X RESEARCH VEHICLE CONFIGURATION



HYPER-X 3 View/Reach

 Hyper-X
NASA Langley Research Center 3/19/1997 Image # EL-1997-00033

Figure 25. Schematic depiction of X-43 vehicles. (Reprinted courtesy of NASA).




 NASA Dryden Flight Research Center Photo Collection
<http://www.dfrc.nasa.gov/gallery/photo/index.html>
NASA Photo: EC99-45265-23 Date: December 1999 Photo by: Tom Tschida
X-43A Vehicle During Ground Testing

Figure 26. Photo of X-43A vehicle during ground testing. (Reprinted courtesy of NASA).

3. RF Interaction with Reentry Vehicle Flow Field

3.1 The Physical Problem

The physical problem has been succinctly and clearly summarized by Nusca and Cooper [1998]: As an example, consider a body of revolution (e.g., an RLV) traveling at high velocity (i.e., 4-6 km/s) in the atmosphere with a trajectory that traverses moderate to high altitudes (40-60 km). Figure 27 shows a representation of the flow field around the vehicle forebody with several physical effects highlighted including: the shock layer, the entropy layer, the boundary layer, chemical equilibrium in the stagnation region, flow expansion onto the conical forebody causing chemical “freezing” of ionization at a nonequilibrium state, surface enhancement of chemical reactions, ablation introducing additional chemical species and free electrons into the reacting gas, as well as a static charge on the surface that can be strong enough to interact with free electrons and ions in the gas (i.e., charge separation and forced diffusion effects).

Now consider an antenna within the body surface (Figure 27). The antenna transmits electromagnetic (EM) radiation in the form of a microwave signal for purposes of communication, sensing, or telemetry through a layer of ionized gas of variable thickness along the antenna aperture. The interaction of EM radiation with the ionized gas flow field causes several effects: the signal propagation path is altered and a signal phase shift occurs (refraction causes the wave propagation speed to change), a loss in signal strength occurs due to attenuation (power or energy loss changes the intensity of the wave), and the antenna free space radiation pattern and admittance properties are modified. The ionized gas layer represents a stratified medium or a medium of varying elasticity. The speed of each wave component is different for each frequency (or wavelength) in the medium; the medium is said to be dispersive and the wave is refracted by the medium (i.e., phase shift). If the frequency of the harmonic EM wave is similar to the frequency of the electrons, the electrons will absorb energy from the wave. Since this energy is related to the frequency of the wave, this frequency will change. The amplitude (proportional to the intensity) of the wave will decrease as it travels through the medium and the wave is said to be attenuated. All of these effects may be expected to occur simultaneously, and are dependent upon the properties of the gas.

3.2 Plasma and RF Code Development

During the 1970s, a number of algorithms were programmed and validated by The Aerospace Corporation for predicting the performance of slot antennas in the presence of a plasma layer. The software codes could calculate the input impedance, gain, and radiation pattern of slots in the presence of a boundary-layer type of plasma. Mutual coupling between slots on a conducting surface in the presence of a plasma layer could also be computed. (It was determined that for sharp-tipped vehicles at low altitudes, the coupling between slots could give a reliable measurement of the integrated electron density in the plasma layer.) These codes were first tested with laboratory measurements made in free space and later using plasmas generated in a reentry sheath simulation facility that was unique to The Aerospace Corporation. Under programs such as Fuzing and Arming Test and Evaluation (FATE), predictions were compared with flight test results (as well as with predictions by other contractors), and were found to have excellent agreement.

Unfortunately, some of the codes were written in Fortran 3, which did not support complex variables and required the use of punched cards. The codes were input on the cards and run on Aerospace’s

CDC 7600 computer. Aerospace has retained printouts of the old codes. These include planar, cylindrical, and sharp-tipped conical geometries covered with plasma layers. The planar codes required for this study have been converted to Fortran 95, which can be run on a personal computer.

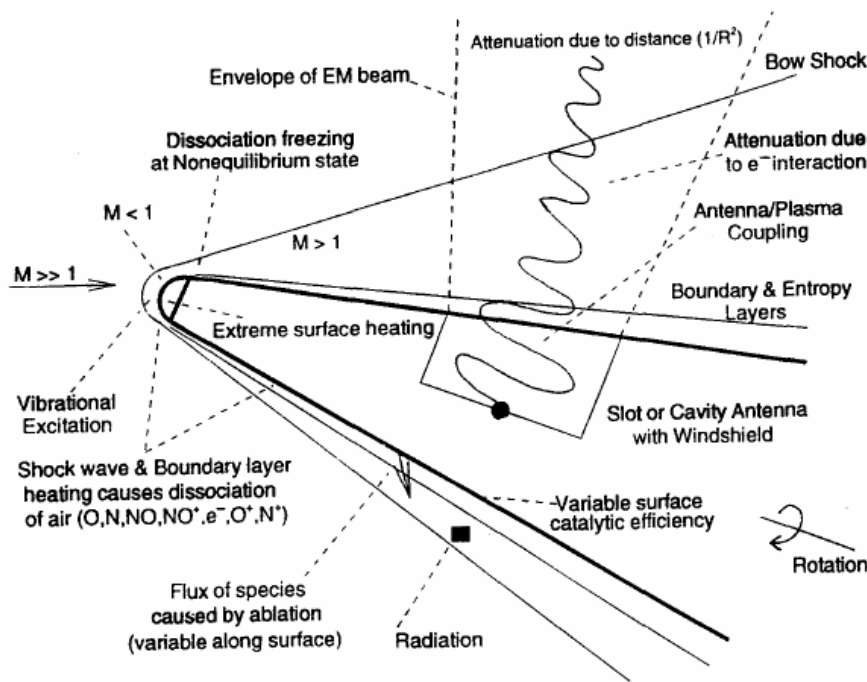


Figure 27. Representation of the Physical Problem (M = Mach number).
[Nusca and Cooper, 1998].

3.2.1 BLIMP, HYGPSIM, REACH, and EMRUN Codes

For axisymmetric/2-D boundary layer conditions, the most widely used algorithm in the industry is the Boundary Layer Integral Matrix Procedure (BLIMP) code [Aerotherm, 1970; Lin et al., 1995]. BLIMP includes heatshield ablation effects in its formulation and has built-in multi-species transport properties and chemical reacting flows. A new code, HYpersonic GPS SIMulation (HYGPSIM), was developed by The U.S. Air Force Research Laboratory (AFRL), in conjunction with Xotech, Inc. (acquired by the Northrop Grumman Corporation in 2003) [Mather et al., 2005]. This suite of models includes a hypersonic flowfield solver called the REentry Aerothermal CHEmistry code (REACH) and an electromagnetic propagation solver called EMRUN. The REACH code predicts the on-body plasma formation during hypersonic reentry for multiconic and lifting body vehicle geometries that fly ballistic and maneuvering trajectories. The EMRUN code then predicts the antenna performance during flight, accounting for the reentry plasma effects on the electromagnetic signal.

A summary description of the REACH and EMRUN codes is provided in [Mather et al., 2005]. The REACH plasma prediction code [Hall et al., 2004] was developed by Science Applications International Corporation (SAIC) in the mid 1980s and modified in the early 1990s. REACH incorporates either equilibrium or non-equilibrium boundary layer chemistry to model plasma formation for non-ablating or ablating reentry vehicles with spherical nose caps. REACH was

designed for computational efficiency by coupling inviscid shock layer solutions and nonequilibrium boundary layer solutions, limiting the computationally intensive non-equilibrium calculation to specific body streamlines of interest. Current capabilities allow the user to calculate plasma profiles for conic, multi-conic, elliptical, and lifting body vehicles with ballistic and maneuvering trajectories for both zero and non-zero ($< 8^\circ$) angles of attack. The code is currently capable of treating multiple heat shield layers of a variety of standard and user-specified materials and radiation gaps. REACH has long been the preferred model for predicting plasma formation during reentry at high velocity, due in large part to substantial validation of the model with intercontinental ballistic missile (ICBM) reentry tests. Experimental validation of the REACH code has been reported by Morris et al. [1999].

The EMRUN code [Golden, 2004] was developed in the 1980s to simulate antenna performance in a plasma environment. Xontech, Inc., streamlined the code in the 1990s to improve calculation performance and allow for circular apertures and antenna noise considerations. The code is designed to take electron density information in the boundary layer normal to the antenna location and to segment that non-uniform density profile into discrete uniform layers of varying thicknesses. It currently calculates ohmic loss across the plasma boundary layer, RF reflection and refraction in the plasma, RF interaction between the boundary layer and the antenna window, losses in the window, and thermal effects on RF propagation.

3.2.2 PIRATE Tool Set

Sandia National Laboratories has funded development of the Poly-Iterative Reacting Aero-Thermal Evaluation (PIRATE) tool set, which has utility for performing a parametric evaluation of plasma effects for a standard reentry system over a variety of flight conditions. PIRATE is Fortran code that acts as a driver program to solve the heating, thermal response, chemistry, inviscid flowfield, and electromagnetic wave propagation/interaction design problem for modern hypersonic systems. To accomplish this task, it employs a number of thermophysics programs executed iteratively and sequentially as necessary from a primary routine. All codes executed by the controlling routine are referred to as constitutive programs. A total of thirteen programs make up the constitutive pool. Evaluation of the design problem requires performing a coupled physics solution between the imposed aerodynamic surface heating and the ablating decomposing heatshield thermal response. To address this, PIRATE executes heating, thermal response, and chemistry analysis tools iteratively as required from the main program until a user-defined convergence criterion is met. The solution is performed over the entire vehicle surface for a complete reentry trajectory [Potter, 2006].

3.3 Slot Gain vs. Frequency

The Aerospace team selected two boundary-layer electron-density and collision frequency profiles for a hypothetical sharp-tipped conical body, one at low altitude (15 kft) and one at high altitude (154 kft). For the low-altitude case, the plasma layer is thin and has an extremely high collision frequency (~ 150 GHz). At high altitudes, the plasma layer is thicker and the collision frequency is several orders of magnitude less. The electron density and collision frequency have been reduced to a data list, which can be input to the planar code. These two profiles will be used to determine the reflection from and transmission through the plasma over a range from 0.5 to 50 GHz.

The team selected gain as the most appropriate parameter to compute for plasma-sheathed antennas because gain can be used directly in communication link calculations. In the calculations, the team

assumed that the slot antenna consists of a waveguide filled with a dielectric material that terminates in a ground plane. The dielectric window material is taken to be Dynasil, a fused quartz.

The gain of a waveguide-fed slot antenna is determined by first calculating the input admittance of the slot when covered with the appropriate plasma layer. Then, for an assumed incident power, the dominant waveguide mode voltage is computed at the aperture using the previously calculated aperture admittance by taking the electric field of the dominant mode at the aperture for the aperture field distribution. Radiated fields are then determined. The gain is the ratio of the power density computed in the far field to that of a hypothetical isotropic source that radiates the same power as that which is incident in the dielectric-filled waveguide.

Gain as a function of frequency was computed for a Dynasil-filled rectangular slot antenna using the electron density and collision frequency (ν) profiles computed for a hypothetical sharp-tipped conical reentry vehicle, a blunt-tipped cone (RAM C), and for the Shuttle. The so-called “planar” model was used. In this model, an infinite plasma sheath is assumed over a ground plane having the same electron density and ν as computed for the true shape and reentry conditions. The results using this model have been compared to laboratory and “in-flight” measurements and give good results when used appropriately. The aperture dimensions of the slot were adjusted at each frequency in order to cover the large frequency band (0.5 to 50 GHz). That is, the height of the slot, a , and the width of the slot, b , were selected to be a constant multiple of the free space wavelength.

In Figure 28, the gains at broadside (GAIN00), at 30° in the E-plane (GAINEP30) and 30° in the H-plane (GAINHP30), are shown for a Dynasil-filled rectangular slot (scaled as described above) on a bare ground plane. The E-plane for a rectangular slot corresponds to ϕ equal to 0°, and the H-plane corresponds to ϕ equal to 90°. The angle ϕ is defined in Figure 29. For the bare ground plane, the gain for the scaled slot is shown to be independent of frequency. It is highest at broadside and decreases faster in the H-plane than in the E-plane. (Note that the aperture dimensions are smaller by a factor of about two and the gain of the dielectric-filled waveguide is about 3 dB less than that for an air-filled waveguide).

3.4 Sharp-tipped Vehicle RF Results

Calculations were performed on a hypothetical sharp-tipped conical reentry body that maintains high velocity to very low altitudes. This leads to electromagnetic properties that can be quite different from those of the blunt tipped or lifting reentry bodies. To illustrate this difference, consider the collision frequencies associated with clean air shown in Figure 30. From 0 to 300 kft, the collision frequency (ν) is seen to change by six orders of magnitude. The curves were plotted using the equation:

$$\nu = 3 \times 10^8 (\rho/\rho_0) T \quad \text{Hz} \quad (2)$$

where ρ/ρ_0 is the density ratio and T is the temperature in degrees Kelvin. This equation was derived from a curve fit to the equilibrium results for high-temperature air from Bachynski et al. [1960].

While the equation gives the collision frequency for air only at a given temperature at the ambient pressure (i.e., does not include the added pressure produced by a shock), it gives an estimate of the ohmic loss of a plasma at a given altitude.

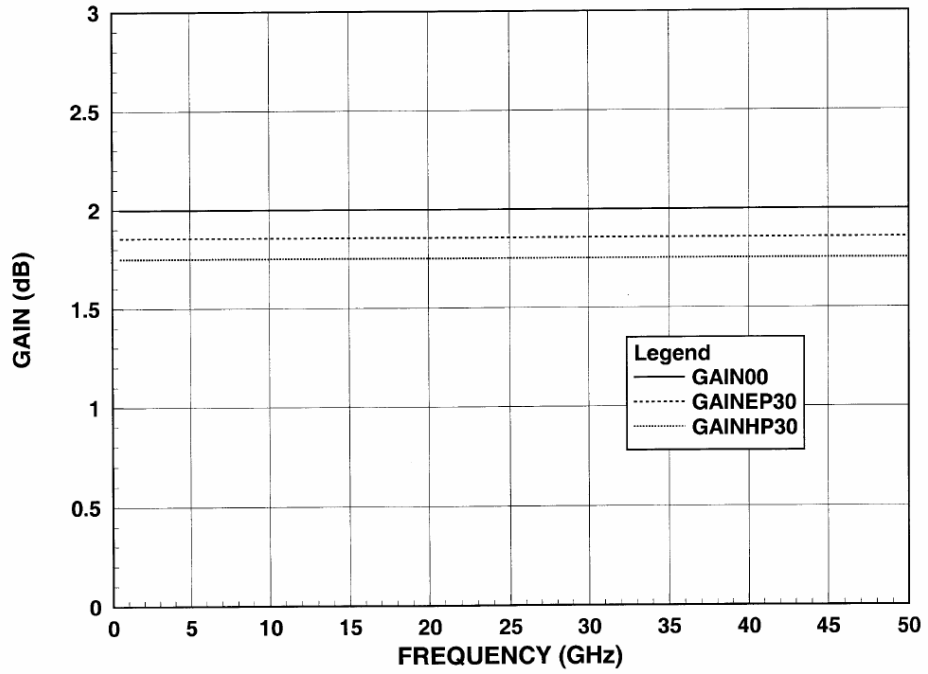


Figure 28. Gain of Dynasil-filled guide.

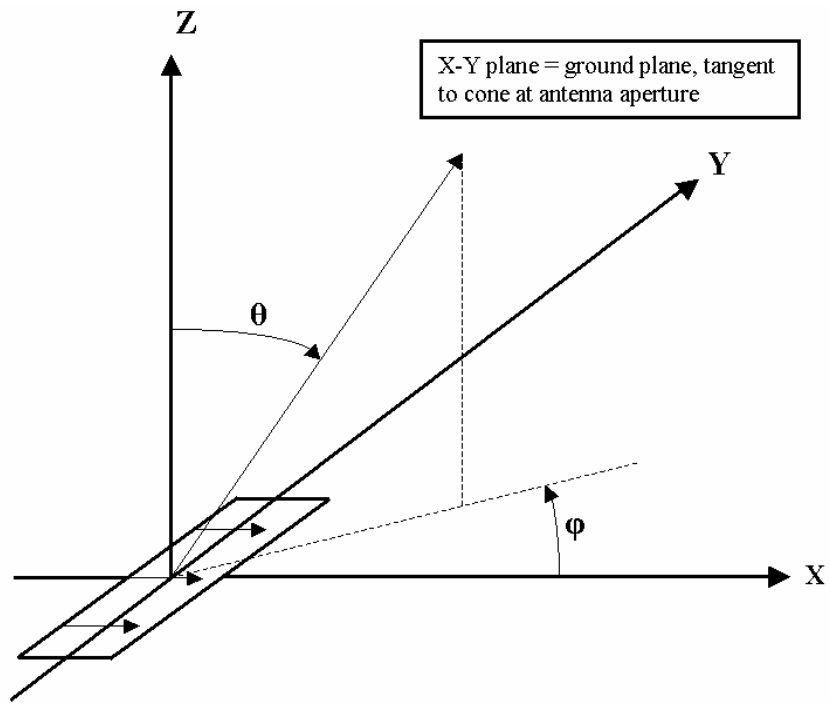


Figure 29. Rectangular slot antenna geometry.

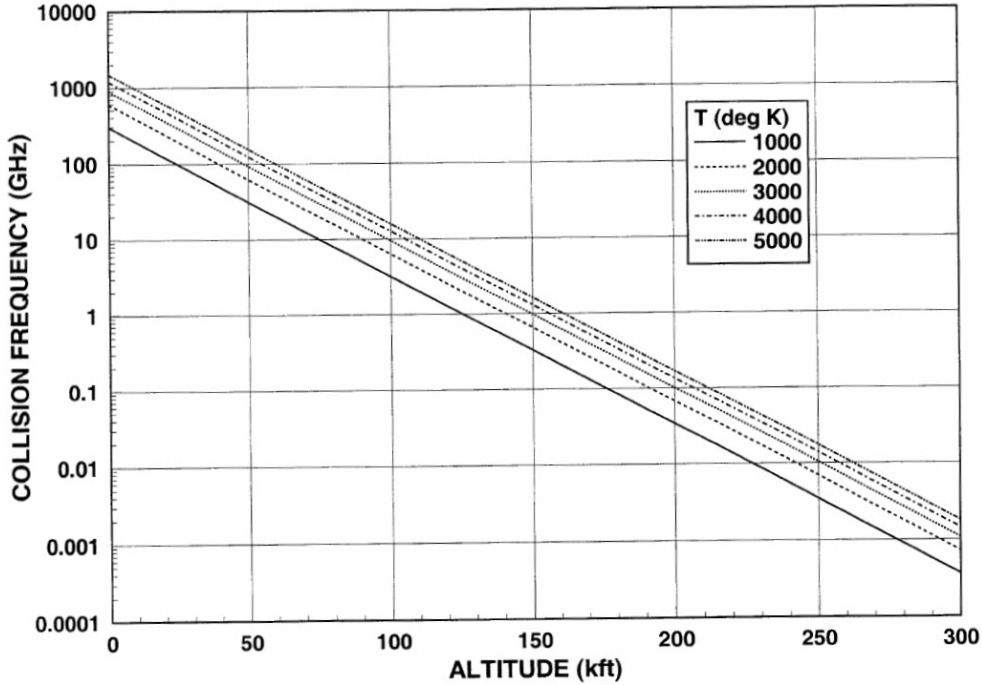


Figure 30. Collision frequency vs. altitude.

For a thin plasma with a collision frequency much greater than the signal frequency, the effect of the plasma sheath on a slot antenna is the same as that which would be produced by covering it with a material (such as space cloth) that has the same conductivity. The conductance of the plasma layer is:

$$G_s = 0.000281 \times \text{Integrated Electron Density/Collision Frequency} \quad (3)$$

3.5 Data for Sharp-tipped Configuration at Higher Frequencies

A key issue is whether the blackout problem can be alleviated by going to higher or lower frequencies. At higher frequencies, one must consider the effects of atmospheric absorption and attenuation. In order to avoid the effects of rain attenuation, a practical limit is about 10 GHz. In spite of this, calculations were made to as high as 50 GHz.

The results of the calculation for the 60 kft post-flight data are shown in Figure 31. The thin sheath model was used to calculate the gain labeled as GAIN_S. The gain is seen to be constant because the thin sheath model predicts a conductance, G_s , which is frequency independent. For the frequencies considered, it gives a good approximation to GAIN₀₀. Since the free space gain of the slot is 2.0 dB, our calculated attenuation at C band is 10.3 dB.

To demonstrate the importance of collision frequency, the same calculation was performed using five collision frequencies that varied from 20 to 100 GHz. The results are shown in Figure 32. Increasing collision frequency, contrary to intuition, is seen to reduce the attenuation.

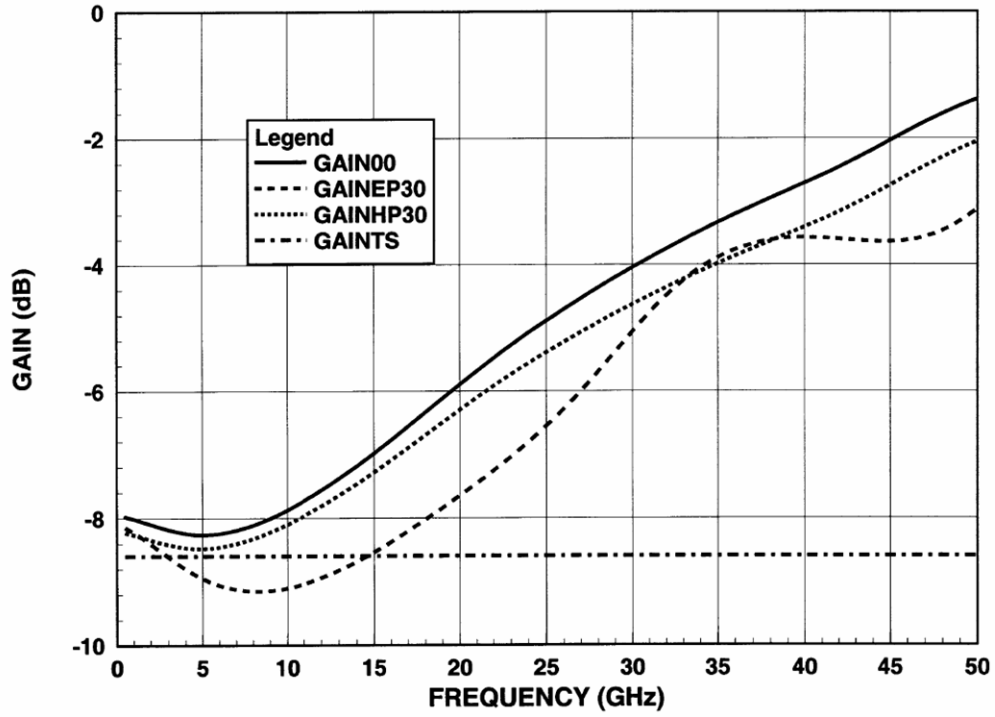


Figure 31. Sharp-tipped configuration, 60 kft.

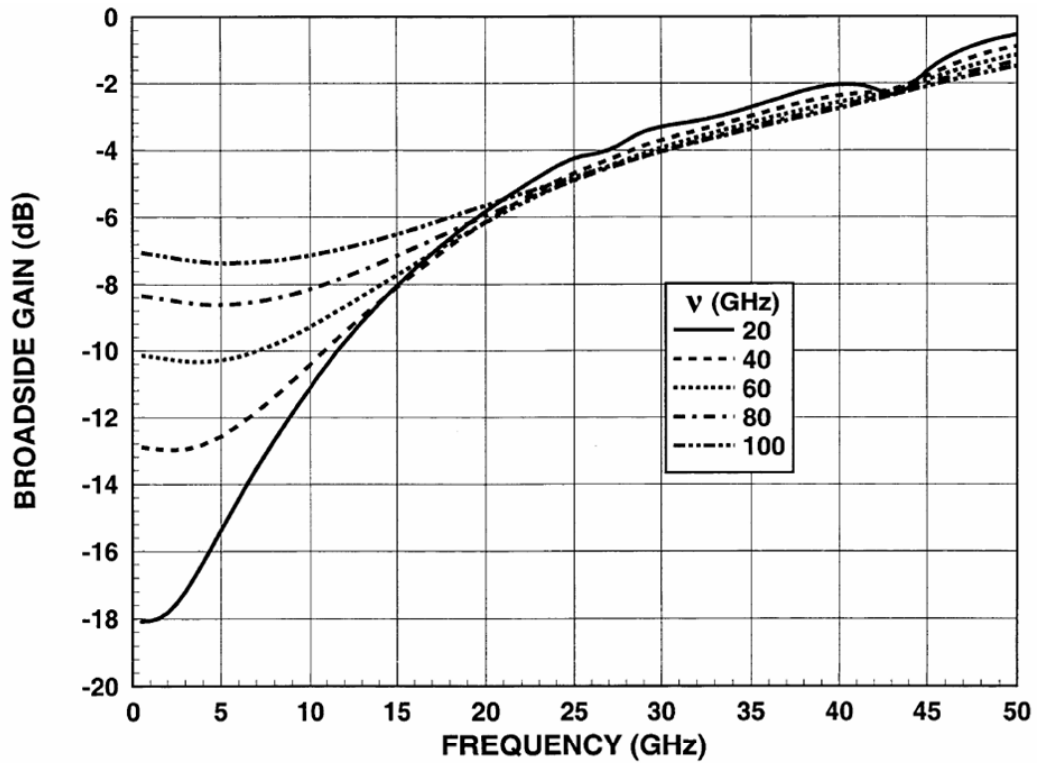


Figure 32. Sharp-tipped configuration, 60 kft, variable collision frequency (ν).

3.6 RAM C Radio Frequency Results

The RAM C vehicle was a blunt-tipped cone with a nose radius of about 6 in. There were three flights: RAM C-I, RAM C-II, and RAM C-III. Although all three flights followed approximately the same trajectory, there were differences in the heat shield material and the experiments flown on all three vehicles. In the RAM C-I and C-III flights, Narmco 4028, a phenolic-graphite charring ablator, was used at the nose. In the RAM C-II flight, for the primary data period from 300 to 180 kft, a beryllium (Be) nose cap positioned over a teflon ablator allowed reflectometer data to be taken in clean airflow. After 180 kft, the nose cap was ejected leaving the teflon as an ablator. All of the payloads used teflon on the afterbody for heat protection.

Analysis of a sample of Narmco 4028 material showed that it contained up to 5000 $\mu\text{g/g}$ of alkali (Na and K) as impurities. The beryllium nose cap and Teflon ablator were found to be free of any significant amounts of alkali.

The RAM C-III was selected for analysis because the clean airflow around that vehicle should have produced low electron density. The electron density profiles calculated preflight for contaminant-free flow at various altitudes are shown in Figure 33 [Swift et al., 1970]. Those authors apparently assumed no loss of the plasma sheath, as the collision frequencies are not given. Collision frequencies based on Figure 30 were selected for calculations, but the effect of varying the collision frequency will be shown. Calculations were performed for the 250, 233, 202, 156, and 131 kft profiles. The only profiles that displayed significant attenuation at C band were 156 and 131 kft. The slot antenna gains for these two altitudes are shown in Figures 34 and 35, respectively. The gains for these high altitudes clearly depend on angle and polarization. While the broadside and H-plane gains shown are relatively smooth curves, the E-plane gain shows an irregularity because the E-plane patterns always show more change due to refraction through the under-dense outer layer. To eliminate this irregularity, the electron density profile must be approximated using many more steps.

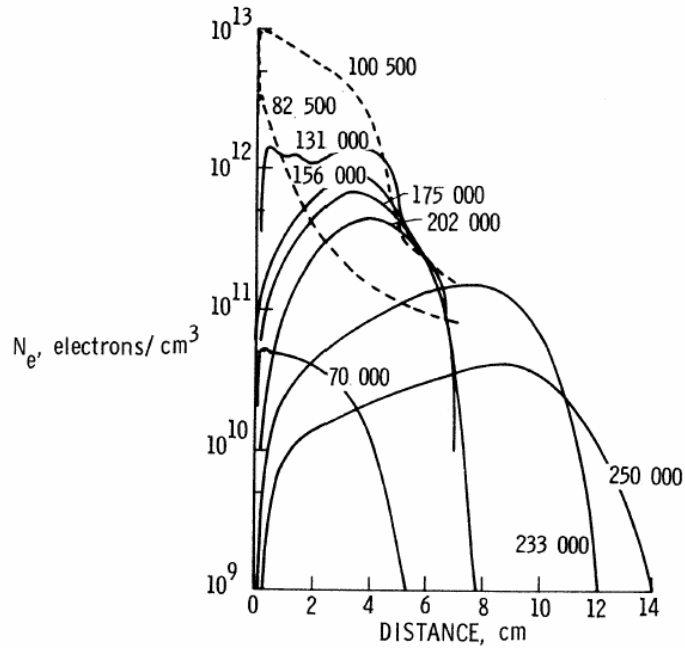


Figure 33. Electron density profiles calculated preflight for contaminant-free flow at various altitudes. [Swift et al., 1970]. (Reprinted courtesy of NASA).

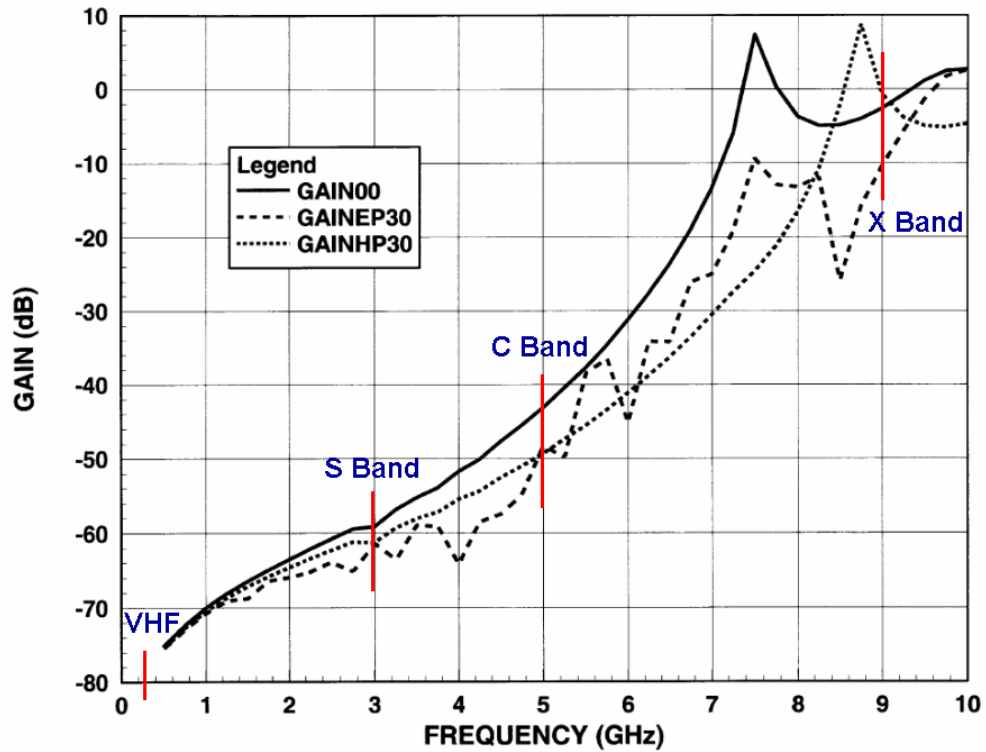


Figure 34. Slot gains for RAM C-III at 156 kft altitude.

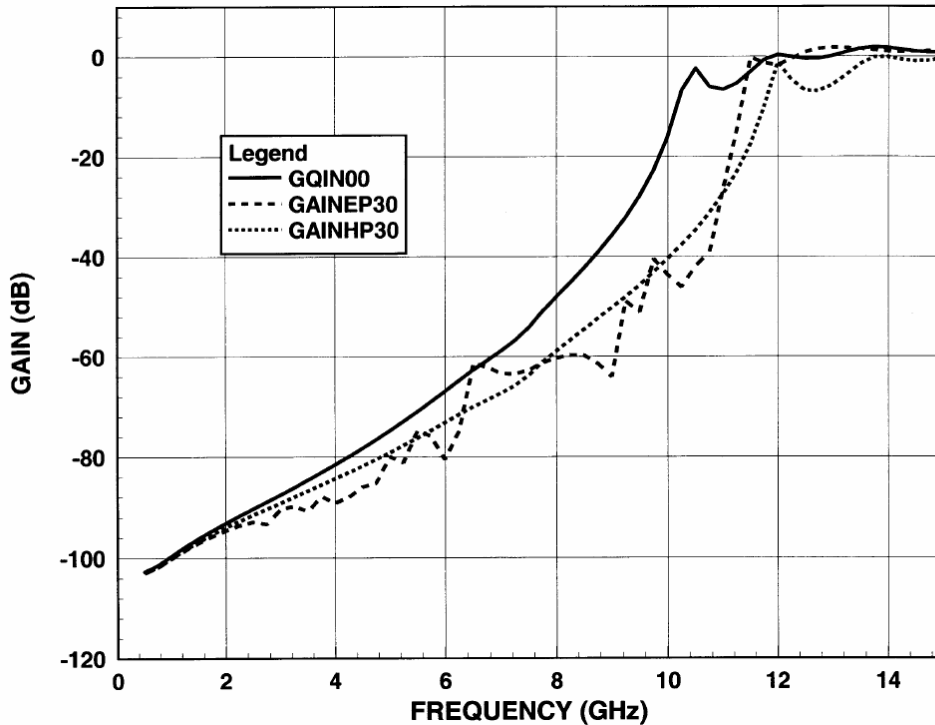


Figure 35. Slot gains for RAM C-III at 131 kft altitude.

The Aerospace Corporation built a unique anechoic chamber, capable of being evacuated, in which models could be clad with simulated plasma using an Aerospace-developed technique [Stewart, 1967]. This allowed testing of the models without the pattern distortion effects produced by a radome. The tank and model are shown in Figure 36. Using this facility, the pattern distortion effects that can occur at high altitudes, even when the plasma is under-dense, can be determined [Stewart et al., 1970]. The tank was first evacuated and then refilled with argon to a pressure of about one torr (1/760 of standard atmosphere). By varying the background pressure, the thickness of the plasma could be changed. A pressure of about 1.25 torr produced the plasma thickness as would be encountered by a sharp-tipped conical reentry vehicle at 154 kft. A sharp-tipped conical model used for the testing is shown in Figure 37 along with the contours of electron density. The plasma is produced by exciting the tip with a high-voltage pulse. Positive argon ions are accelerated into the conical model, and secondary electrons are emitted at the surface. The electric field between the plasma and the model accelerates these secondary electrons into the plasma layer. The secondary electrons produce more positive ions and electrons continuing the process. The plasma layer thickness is determined by the range of the secondary electrons. Measurements are made in the afterglow approximately 10 μ sec after termination of the pulse.

The E-plane radiation pattern for the symmetrically excited sharp-tipped conical model is shown in Figure 38. Measurements were taken for a series of under-dense cases with a signal frequency of 9.0 GHz. (For this frequency, the critical electron density is approximately 1.0×10^{12} electrons per cc). For the same model, a series of E-plane patterns were taken with the plasma over-dense. These are shown in Figure 39. Whereas the symmetrically excited bare cone has a null in the forward direction, the asymmetrically excited bare cone has a peak on the axis of the cone. Figure 40 shows that the plasma produces significantly more attenuation of this forward peak than it does at broadside.

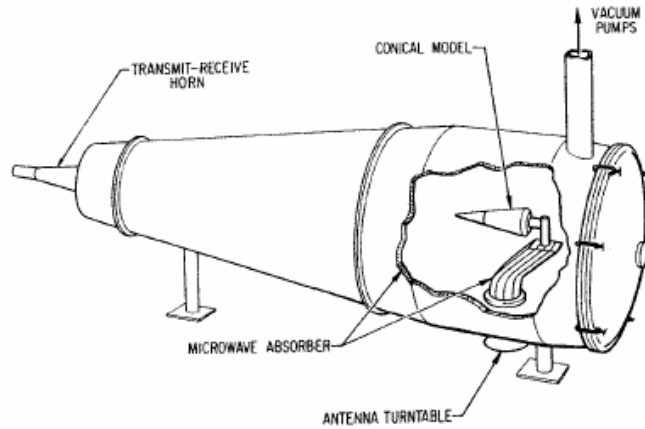


Figure 36. Conical model mounted in microwave anechoic chamber capable of being evacuated.

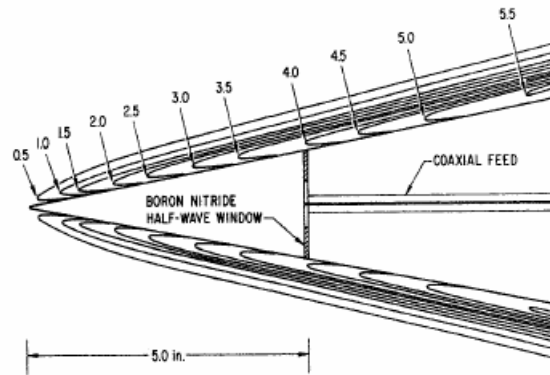


Figure 37. Tip of conical model with symmetrically excited gap showing coaxial feed and contours of constant electron density for excitation using an anode at the back.

The description of the RAM C results by Grantham [1970] shows a “blackout” from approximately 280 to 80 kft. The term “blackout” is a confusing term. It really describes a period of time during which a particular communication system fails to operate. Without knowing what the frequency is or what margins exist in a link, it gives no information about the plasma sheath parameters. A better way to describe the effects of the plasma sheath is to look at the attenuation as a function of frequency. For a thin plasma sheath, the attenuation is independent of angle. For the thicker plasma layers, the attenuation can be higher at angles away from boresight. Calculation of the gain of a slot antenna at a given angle minus the gain with the plasma layer present yields the appropriate attenuation value for use in a link calculation.

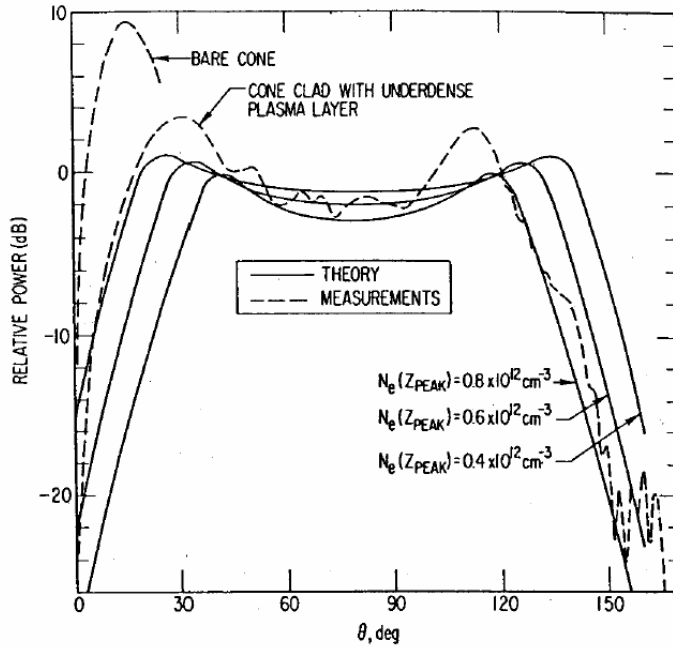


Figure 38. Axial cut of E_0 radiation pattern for symmetrically excited cone clad with underdense plasma layer. Argon pressure 0.6 torr. [Stewart et al., 1970]. (Reprinted courtesy of NASA).

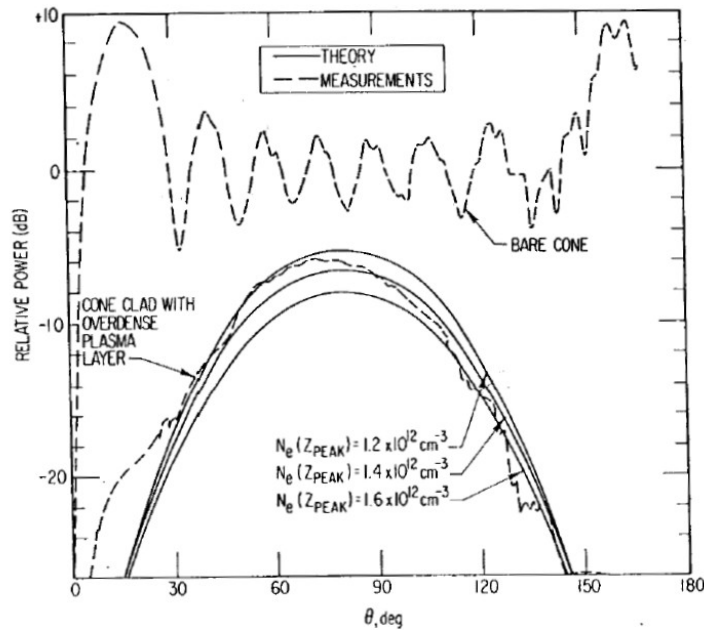


Figure 39. Axial cut of E_0 radiation pattern for symmetrically excited cone clad with overdense plasma layer. Argon pressure 0.6 torr. [Stewart et al., 1970]. (Reprinted courtesy of NASA).

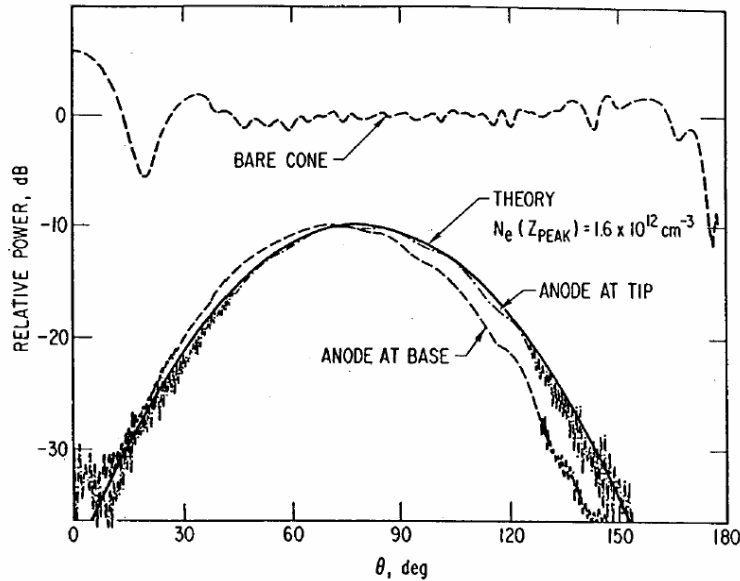


Figure 40. Axial cut of E_0 radiation pattern for asymmetrically excited cone clad with overdense plasma layer. Argon pressure 0.6 torr. [Stewart et al., 1970]. (Reprinted courtesy of NASA).

Since information about the angles between the vehicle and the ground station was not available, pattern distortion could not be included in analysis of the RAM C-II data. Therefore, the calculations were compared using only the boresight gain labeled in the figures as GAIN00. Attenuation of 10 dB was selected as one that would seriously impact a communications link. Calculated results from 131, 156, and 202 kft, and interpolated gains, indicated that the C-band link would be degraded by 10 dB at 181 kft. Similarly, an X-band communication link would be degraded by 10 dB at 148 kft.

The signal loss (i.e., attenuation) for the RAM C-II at C band and X band is shown in Figure 41 [Schexnayder et al., 1970]. The experimental data shown are clearly curve-fitted to the original data, since it is smooth showing no tracking errors, roll modulation, or noise. The altitudes for the signal loss to reach 10 dB are 163 kft for C band and about 152 kft for X band. There is clearly a signal received for C band down to about 138 kft and for X band down to 125 kft. The difference between the calculated altitudes and those measured is not unexpected because preflight flow fields at widely spaced altitudes were used, and an accurate collision frequency and data on the angles to the ground stations were not available.

In order to show that effects of collisions are less important for high-altitude cases, the electron density profile for RAM C-II at 156 kft altitude was examined with collision frequency treated as a parameter. In computing the results shown in Figure 34, a collision frequency of 0.7 GHz was estimated. Allowing the collision frequency to vary from 0.5 to 2.5 GHz, the results shown in Figure 42 were computed. As seen, there is almost no effect on the broadside attenuation except at very low frequencies and at frequencies close to the plasma frequency associated with the peak electron density.

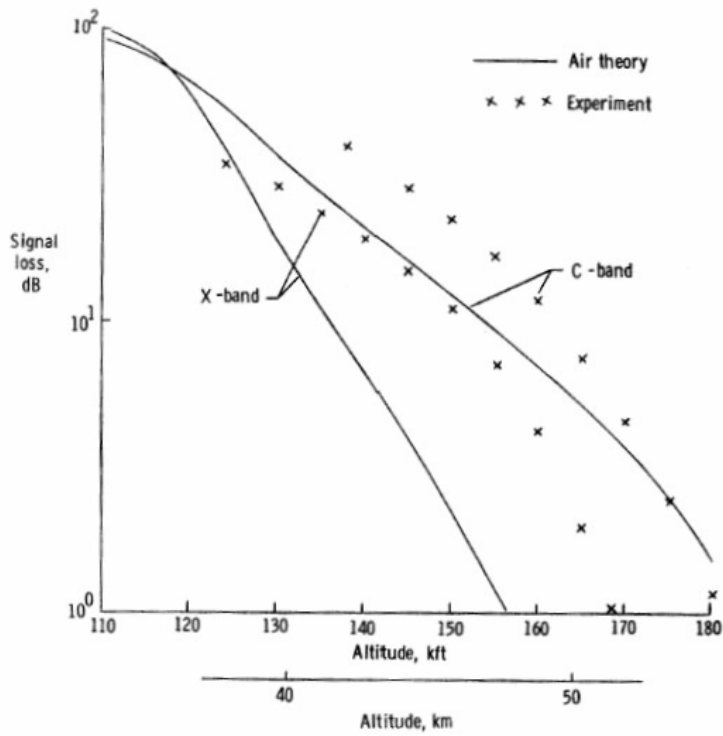


Figure 41. Comparison of RAM C-II microwave attenuation data with air theory. [Schexnayder et al., 1970]. (Reprinted courtesy of NASA).

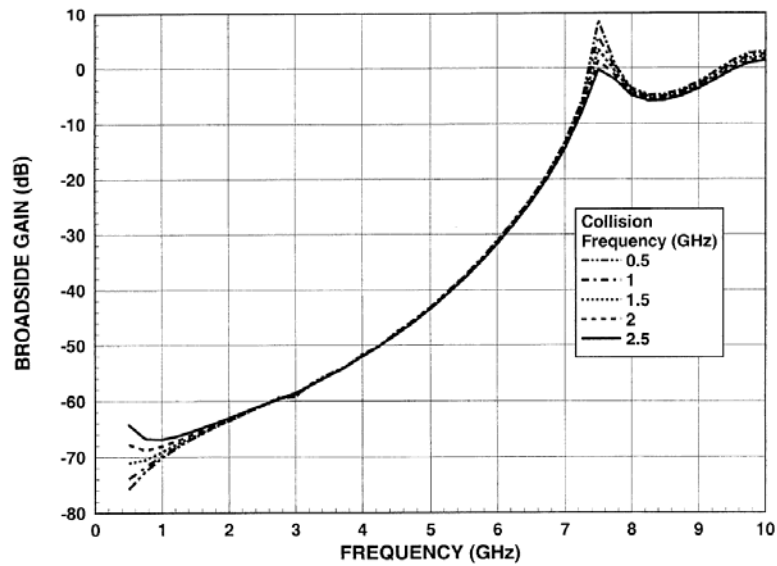


Figure 42. Broadside gain calculated as a function of frequency for RAM C at 156 kft altitude.

3.7 Antenna Breakdown

The first flights to quantify effects of antenna breakdown during reentry were those of Trailblazer vehicles on June 18, 1967, and June 17, 1969, conducted by the Air Force Cambridge Research Laboratory. Tests were run only at S band (2.8 GHz) and consisted of a sequence of 7.3 μ sec pulses transmitted at three different power levels: 600, 300, and 100 watts. The nonlinear effect can clearly be seen in Figure 43. At high power, 70 percent of the power is reflected at an altitude approximately 8 kft higher than the lowest power. Although this measurement is based on average power during the pulse, the shapes of the pulses clearly shows the effect of breakdown except for the lowest power.

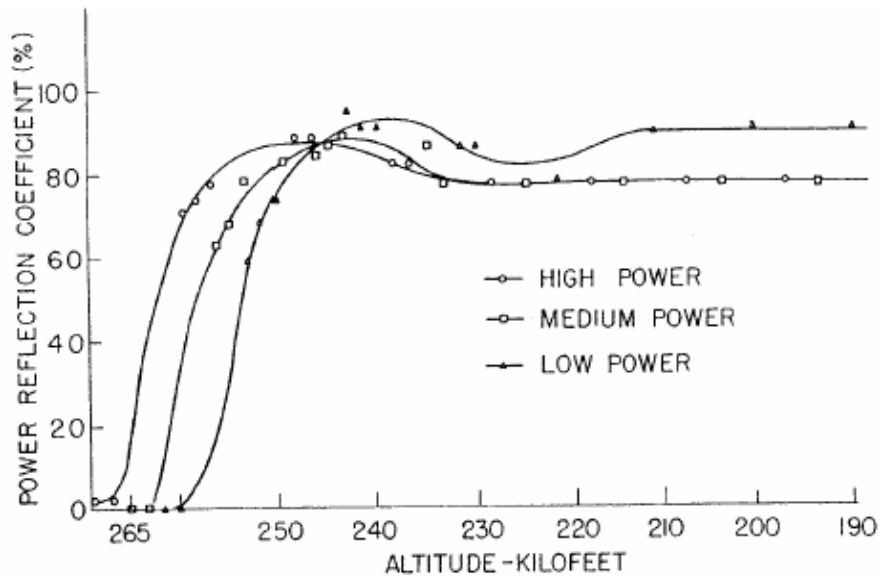


Figure 43. Power reflection coefficient, Trailblazer flight 2.

3.8 GPS Reception Enhancement

Typically, GPS antennas have wide-angle coverage with resultant low gain because of the desire to keep multiple satellites in the field of view. Low power from GPS signals would be further degraded by signal attenuation due to plasma sheaths around reentering vehicles. If the antenna is located on the aft side of a lifting reentry vehicle, there may be little attenuation because of the absence of a plasma sheath on that surface, but multipath phenomena might be produced by reflections from the wake and plasma spilling around the vehicle top and sides.

To increase the antenna gain and reduce the effects of multipath, an array antenna could be built that is capable of forming multiple receive beams. To achieve the best possible noise figure, a low-noise amplifier (LNA) would be provided for each element. Associated with each beam would be a beam-forming network. These beams could be pointed at individual satellites given the location and attitude of the reentry vehicle and the ephemeris data of the GPS satellites within the field of view. Alternatively, each beam could acquire and track a given GPS satellite.

4. Identification and Comparison of Mitigation Approaches

Ground communications signals with space vehicles are interrupted during certain stages of reentry into the Earth's atmosphere, as mentioned previously for the Shuttle. A plasma sheath formed around the vehicle absorbs energy from the electromagnetic carrier waves commonly used for communication. The electromagnetic field (EMF) loses energy to the plasma by doing work on the electrons in the plasma in the form of joule heating. A useful conceptualization of this process is the following. Electrons are held in a three-dimensional array by mutual repulsive interactions. Translation of electrons from their equilibrium positions results in coulombic forces opposing that movement, forces whose magnitude depends on the electron density. These harmonic forces create a characteristic resonance frequency, or plasma frequency ω_p . The energy of the oscillating electrons is dissipated through collisions with neutral atoms and molecules. The efficiency of this energy loss mechanism can be related to the plasma frequency, ω_p [Raizer, 1977]:

$$\omega_p = (4\pi e^2 N_e / m)^{1/2} \quad [\text{CGS units}] \quad (4)$$

where e is the charge on an electron, N_e is the electron density, and m is the electron mass. The oscillating electromagnetic field of RF carrier waves used in communications can interact strongly with the electrons in the plasma. The system becomes that of a damped, driven oscillator with resonance frequency ω_p and driving frequency ω , the communications transmission frequency. As equation (1) indicates, the electron density is the most critical factor in the plasma absorption of EMF energy in communication signals, and the foregoing processes determine the electron density.

A number of approaches have been suggested for mitigating the interruption of communications due to the interaction of plasma electrons with RF signals and are reviewed in this section. These mitigation approaches are listed below. The numbers in the list correspond to section numbers in this report:

- 4.1 Aerodynamic shaping [Belov et al., 2001]
- 4.2 Quenchant injection [Modica et al., 1970; Cowperthwaite et al., 1970; Parmentier et al., 1970; Aisenberg and Hu, 1970; Akey, 1970]
- 4.3 Magnetic windows [Russo and Hughes, 1964; Starkey, 2003; Rothman et al., 1964; Usui et al., 2000]
- 4.4 High frequencies
- 4.5 High transmit power
- 4.6 Raman scattering

The first four described are the most promising: Aerodynamic Shaping, Quenchants, Magnetic Windows, and High Frequency.

4.1 Aerodynamic Shaping

Flight tests involving sharp-tipped conical reentry vehicles have shown that it is possible at velocities as high as 21 kft per second to enter and pass through the Earth's atmosphere without "blackout." That is, all of the VHF, S-band, and C-band transmissions were received on the ground throughout the flight. The maintenance of a sharp tip might require the use of a refractory metal tip or a transpiration-cooled tip, as proposed by Belov et al. [2001].

If the sharp-tipped cone is not incorporated into the vehicle itself, it could for instance be attached to the front of a blunt-tipped conical reentry body. The antennas on the sharp-tipped cone would need to be located in front of the bow shock. The much higher drag of the blunt-tipped conical body would result in a much less hostile reentry environment for the sharp-tipped cone. For lifting reentry vehicles such as the Shuttle, a pylon might be required to attach a sharp-tipped communications module to the aft side of the vehicle.

During the RAM C flight tests, two rakes (blades) were attached to the sides of the vehicle [Schexnayder et al., 1970; Jones and Cross, 1970]. One was used for making electrostatic ion probe measurements, and the other was fitted with thermocouples. These instruments were used to measure the electron density distribution and the temperature in the boundary layer, respectively. It was assumed that the rakes did not disturb the distribution. The results were consistent with predicted results for unperturbed flow. The rakes were retracted at 180 kft. Schematic depictions of the RAM C vehicles and rakes are presented in Figure 44.

The results of these tests suggest that a “blade” that contains antenna slots in either of the two faces or at the end of the blade could be inserted through the boundary layer with minimal effect on the boundary layer. Even if the blade were extended only past the point of peak electron density, it would greatly reduce attenuation through the plasma layer. It should be noted that as a vehicle descends into the atmosphere, the boundary layer typically becomes thinner as the peak electron density increases. For the RAM C flights, at altitudes lower than 156 kft, the antennas on the blade would need to be inserted only to about 6 centimeters to reach a negligible electron density.

At altitudes below 100 kft, the electron-neutral collision frequencies will considerably reduce the attenuation of a signal received from a conventional slot on the vehicle surface. Communications could be switched to this slot. The blade could then be retracted until flush with the heat shield surface. Flow turbulence where the blade is attached to the heat shield surface would need to be addressed.

A hypothetical blade configuration is shown in Figure 45.

4.2 Review of Quenchants, Their Properties, and Droplet Insertion

Another strategy for mitigating the energy-dissipating effects of plasmas is to introduce a chemical “quenchant” into the flow field that reduces the electron density in the plasma. Flight data of considerable interest to this task include publications on measured plasma field. For example, Akey, [1970] describes RAM blunt-tip vehicle flights, and Parmentier et al., [1970] describes use of sulfur hexafluoride (SF_6) quenchants for sharp-tipped Reentry Antenna Test (RANT) flights. The RAM C vehicle had a large (6 in.) nose radius and 9° half-angle cone. It was 41 in. long and had a 19 in. base diameter. The vehicle was well instrumented with four reflectometers (4 frequencies each) and a rake of 8 electrostatic ion probes near the end of the cone [Schexnayder et al., 1970; Jones and Cross, 1970]. The vehicle entry velocity was 25.0 kft/sec, which it maintained down to 160 kft altitude, degrading to 16.8 kft/sec at 80 kft altitude. Electron densities as high as 6×10^{10} electrons/cc were measured. The RANT vehicle, as described by Parmentier et al. [1970] is a typical slender reentry vehicle with an 8° half-angle, a $\frac{1}{4}$ -in. nose, and a carbon-phenolic heatshield. These authors report that the antenna window is located at a station 30-in. back from the nose. The effectiveness of the SF_6 chemical technique is evaluated for a reentry velocity of 23.5 kft/sec and in the altitude range of 160 kft down to 40 kft.

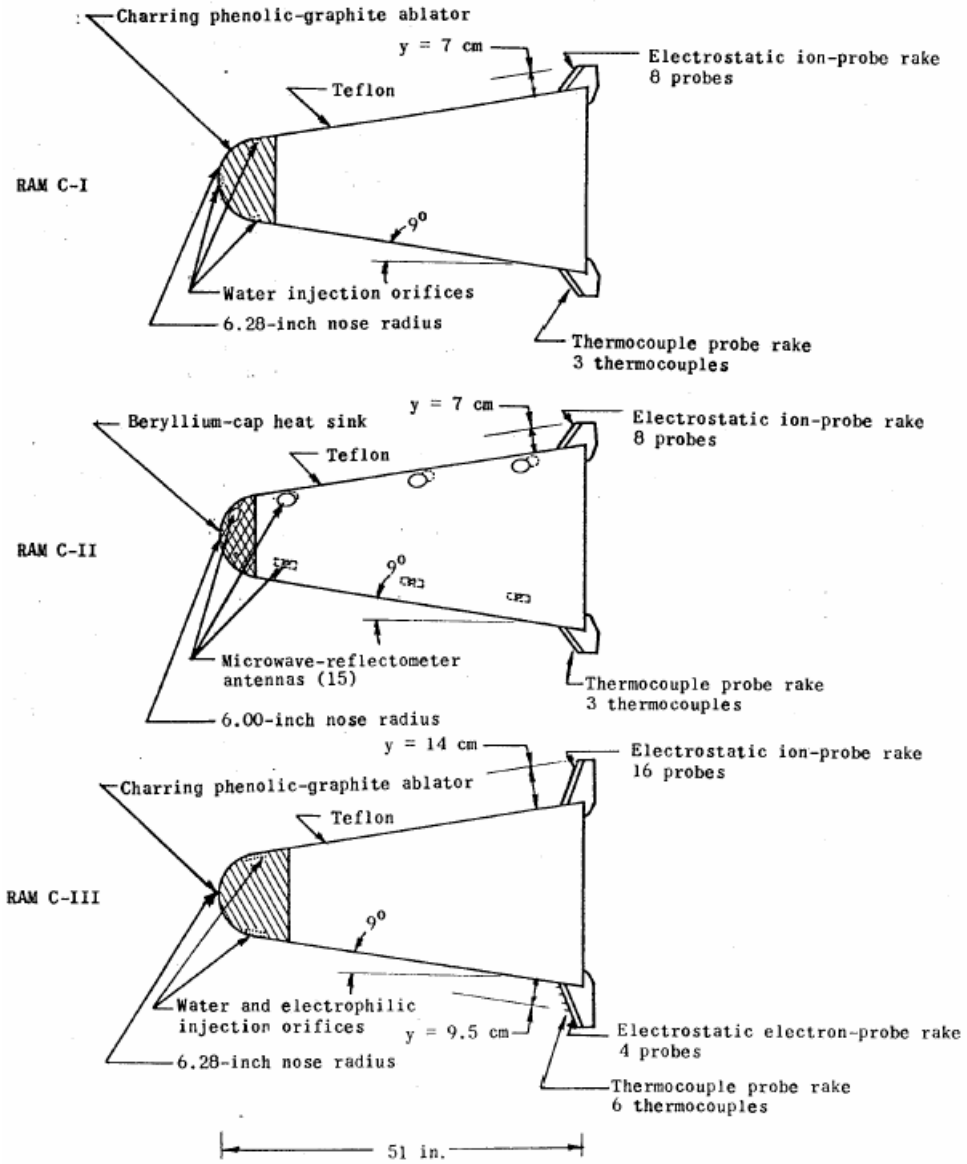


Figure 44. RAM C payload configurations, showing electrostatic ion-probe and thermocouple probe rakes. [Jones and Cross, 1970]. (Reprinted courtesy of NASA).

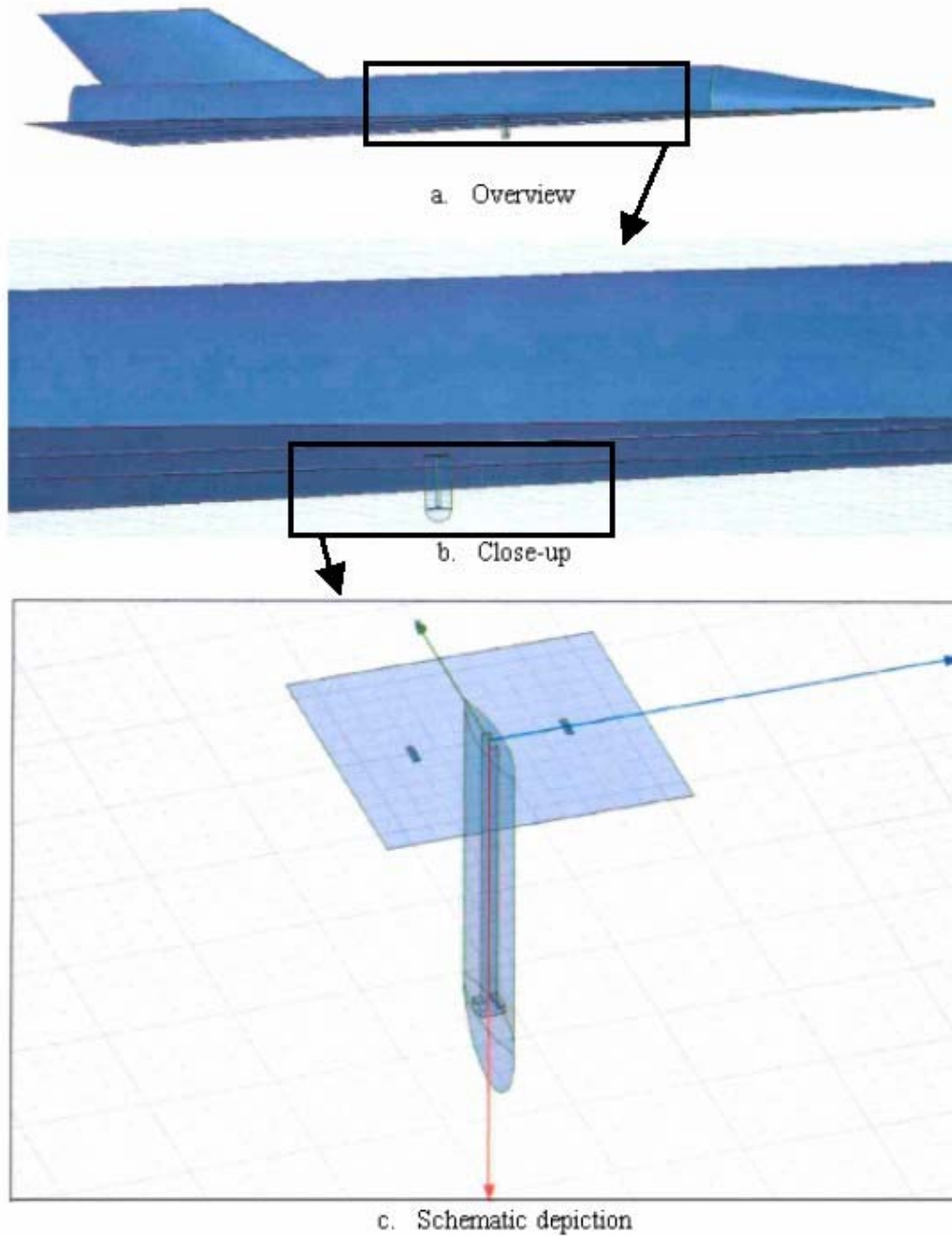


Figure 45. Hypothetical blade configuration.

The following discussion summarizes the underlying chemical principles that make chemical quenchants effective. Plasmas form behind the shock waves of reentry vehicles because the electron-producing processes for atmospheric gases are faster than the electron-consuming processes and the thermodynamic balance of rates produces a partially ionized gas. Injecting chemical quenchants into the plasma can impact its composition, specifically the electron density, in two important ways. First, the quenchant can cool the temperature of the gases, thereby altering the rates and shifting the balance

of rates toward a less ionized composition. Second, the quenchant molecules themselves become part of the system of gases, and depending on their thermodynamic properties they can consume free electrons through electron attachment processes. The goal then is to lower the electron density and plasma frequency to levels where the EMF radiation is not effectively absorbed and communication therefore becomes possible. These conditions can be transitory in the gases flowing over the reentry vehicle, as long as they persist near the communication antenna, “near” being within a wavelength or so of the communication frequency.

The molecular properties that distinguish good quenchant molecules depend on the system conditions and whether thermodynamic or kinetic factors are playing a predominant role. For example, at high temperatures, quenchants with a high electron affinity [e.g., rhenium hexafluoride (ReF_6), EA = 4.7 eV] are based on thermal detachment of the electron. Higher pressures are required to stabilize the negative ion through collisional relaxation. Under these conditions thermodynamic properties are most critical (e.g., EA and heat of formation). At lower temperatures and pressures, kinetic factors (e.g., electron capture rates or cross-sections, polarizabilities, densities of states) can more strongly influence the plasma electron densities. Campbell and Levine [2000] have reviewed recent work studying delayed ionization and fragmentation; long delay times in thermal electron detachment from a quenchant can lead to transient decreases in electron densities.

Sulphur hexafluoride (SF_6) has been the most extensively studied molecule used in plasma quenching, particularly at the lower temperatures and pressures characterizing the plasma trailing reentry vehicles. Recently detailed experimental and theoretical studies have been reported on the low-energy electron scattering/capture behavior of SF_6 [Hunter et al., 1989] and [Christophorou and Olthoff, 2001] and CCl_4 [Kowari et al., 1998].

Several factors contribute to the large electron capture cross-section measured for SF_6 . The large polarizability of SF_6 promotes long-range attractive interactions with free electrons. There are several low-lying energy states for the anion of SF_6 . The SF_6 molecule and anion are fairly large and have 15 vibrational degrees of freedom in which to store energy. The metastable SF_6^{*-} anion formed at low electron collision energies has a long auto-detachment lifetime ($10 \mu\text{s} < \tau_a < \text{ms}$) and can be stabilized by collision or radiation. At higher collision energies several fragment ions are observed (SF_5^- , SF_4^- , SF_3^- , SF_2^- , F_2^- , and F^-) leading to broad resonance bands in the electron-scattering measurements.

Other proposed mitigation techniques have not been followed by validation studies, but may hold potential for RF mitigation [Modica et al., 1970; Cowperthwaite et al., 1970; Parmentier et al., 1970; Aisenberg and Hu, 1970; Akey, 1970]

4.3 Magnetic Window

The third technique for alleviating RF blackout is the magnetic field window concept. Theory supports the concept that a static magnetic field applied to a plasma with the field lines in the direction of intended RF propagation will, under appropriate conditions of field strength and other parameters of plasma as well as the frequency of RF, reduce the plasma attenuation sufficiently that the RF will propagate through the plasma [Russo and Hughes, 1964; Starkey, 2003; Rothman et al., 1964; Usui et al., 2000].

Relatively little empirical data are available to support theoretical models predicting RF blackout mitigation effects using static magnetic fields. Russo and Hughes carried out two experimental tests in the 1960s to measure the effects of static magnetic fields on VHF transmission: a reentry plasma

simulator test and a flight test (RAM A-II) [Russo and Hughes, 1964]. The simulator tests were carried out in a 60-foot vacuum sphere at Langley Research Center using the exhaust from a small, highly aluminized solid rocket motor (100 lb., exit Mach 4, chamber $T = 6200^\circ\text{F}$) to simulate the reentry plasma flow field over a cylindrical (9° half-angle conical model), sharp-tipped probe (2-inch-diameter nose) fitted with a broadband VHS slot antenna aligned with the flow. The plasma simulator produced an approximate average electron density N_e of 3×10^{11} electrons/cm³ and approximate collision frequencies ν of 10^9 /sec in the vicinity of the slot antenna. Unfortunately, electron-density gradients normal to the antenna were not measured directly and theoretically calculated signal losses due to the plasma were estimated assuming a uniform plasma slab thickness of 4 cm. Using a theoretical model based on solving Maxwell's equations and the equations of motion for electrons in crossed electric and magnetic fields, transmission losses from the plasma were calculated to be 45 dB with 14 dB due to reflection. Measured transmission losses were somewhat higher at 60 dB relative to the plasma-free signals.

A magnetic field coil assembly was mounted behind the antenna to generate fields up to a maximum of 750 gauss in a direction normal to the slot antenna and parallel to the transmission propagation direction. The field strength decayed approximately exponentially to half its value (375 gauss) a distance of 1.5 cm along the normal from the antenna. Possible field-induced changes in N_e and ν were not measured. In calculating the influence of an applied magnetic field on transmission the electron density and collision frequency were assumed to be constant and the magnetic field strength was varied in the direction of propagation. Plane waves were separated into two contra-rotating circularly polarized waves. The results indicated that calculated losses were reduced from 45 dB for zero-field to 28 dB for the right-hand circularly polarized component at 750 gauss. The measured attenuation ranged from the 60 dB zero field limit to 40 dB at 750 gauss. This marks the most significant, directly measured blackout mitigation using magnetic fields identified in this study. A window was created below the electron gyrofrequency of the plasma, enabling right-hand circularly polarized waves to propagate with low attenuation.

Unfortunately the more relevant flight test reported by Russo and Hughes produced inconclusive results. The flight test occurred between 150 kft and 310 kft, with payload angles between 0° and 6° , and velocities of 17.7 kft/sec. The magnetic field showed minor signal variations on a modest 5 dB attenuation due to plasma effects. These magnetic field variations were masked by fluctuations due to vehicle motion and antenna pattern.

Rothman et al. [1964] also provided a useful theoretical discussion of the mitigating effects of strong magnetic fields on the attenuation of RF communications. They estimated that for a 10-cm-thick homogeneous plasma slab intended to simulate conditions for a reentry vehicle at 100 kft, a 250 MHz signal would experience 67 dB of attenuation for zero field, 53 dB for a 3 kG field acting on left-circularly polarized light, and 16 dB for a 3 kG field acting on right-circularly polarized light. Few details were provided (e.g., electron density, collision frequency) for these estimates. They also reported laboratory studies demonstrating the mitigating effects of magnetic fields. They generated a plasma above a slot antenna using an inductively coupled focused RF discharge operating in the X band. A rectangular solenoid behind the antenna produced magnetic fields of 280 gauss. While Rothman et al. were able to demonstrate strong effects on the transmission signals from the antenna by applying the magnetic field, a good quantitative analysis was precluded by the strong effects of the field on the RF-generated plasma. The plasma conditions were not well characterized in these experiments.

More recent theoretical studies demonstrate a continued interest in magnetic field mitigation approaches. These studies benefit from the availability of more advanced computational tools for modeling plasma flow fields.

Starkey [2003] has described results from simplified model calculations based on Maxwell's equations of the attenuation of electromagnetic (EM) wave transmission through a plasma sheath as a function of electron collision frequency (ν , a function of temperature and density), magnetic field strength, the transmission frequency (ω), and EM wave polarization. Results for the limiting case of a collisionless plasma ($\nu = 0$) are

$\omega > \omega_p$	100% transmission
$\omega = \omega_p$	100% reflection (0% transmission)
$\omega < \omega_p$	exponential decay in transmission

where ω_p is the plasma frequency. For more realistic "lossy plasmas" ($\nu \neq 0$) significant reductions in attenuation for $\omega < \omega_p$ were obtained only when the collision frequency exceeded the plasma frequency ($\nu/\omega_p > 1$). Above the plasma frequency attenuation drops rapidly with increasing frequency as expected. This implies that use of high frequencies will improve RF transmission.

Starkey also calculated the effects of static magnetic fields on transmission. For magnetic fields with field vectors aligned perpendicular to the EM wavefront, only circularly polarized waves provide solutions to the operational wave equation. As noted by Russo and Hughes [1964], right- and left-hand polarizations behave differently, the former providing up to three orders of magnitude greater reductions in attenuation constants. As expected, higher magnetic fields improve the range of usable transmission frequencies below the plasma frequency. Specific examples associated with the RAM C-II vehicle were calculated for microwave transmission at 2.45 GHz, $\nu/\omega_p = 0.39$, $\omega_p = 5.64 \times 10^{10}$ rad/s, and demonstrated that right-hand polarized EM waves were near the cutoff frequency for transmission at field strengths of $B_0 = 0.1$ T (tesla $\equiv 10^4$ gauss).

Finally, Starkey used an inviscid, steady, nonequilibrium plasma chemistry model to estimate reentry plasma conditions surrounding the Shuttle Orbiter and RAM C-II trajectories, as well as theoretical shapes for designs of an air-breathing hypersonic vehicle in order to predict blackout phenomena as a function of altitude (0–100 km) and Mach number (0–25). Plasma flow field calculations were used to estimate electron density and collision frequency as inputs for calculating transmission attenuation constants as discussed in the preceding paragraphs. The blackout mitigation effects of static magnetic fields ($B_0 = 0, 1$ and 5 T) were examined for hypersonic vehicles transmitting at 2.45, 10, and 20 GHz with circularly polarized waves. Significant improvements in mitigating blackouts by introducing a 1 T field were seen for right-polarized waves (much less for left), but less significant improvements were seen in going to the higher 5 T field. Fields between 0 and 1 were not examined in this study.

Starkey's methods were supported by positive correlations seen between calculated transmission blackout onset and recovery (Mach number and altitude) during simulated Shuttle Orbiter and RAM C-II trajectories and actual flight data. These comparisons were encouraging, but not detailed enough nor quantitative enough to validate his model for design and engineering purposes, nor were such claims made. This was a recent study, more work is needed, and Starkey reports he is continuing his work. No empirical data were reported to support calculated magnetic field mitigation effects and these remain untested.

Calculated magnetic field mitigation effects using a much simpler, one-dimensional modeling approach has also been reported by Usui et al. [2000]. Their model solves Maxwell's equations for

the fields and the equations of motion of the particles in one-dimension in the near-vehicle region using an assumed Gaussian distribution for the plasma. The plasma thickness is assumed to be much thinner than the transmission wavelength. The collision frequency with neutral particles is assumed to be zero ($\nu = 0$). Transmission efficiency is determined by initiating an electromagnetic wave at the vehicle surface and calculating attenuation through the plasma layer as a function of wavelength.

Blackout mitigation using magnetic fields was first examined by applying a magnetic field and analyzing the dispersion relation between frequency (ω) and wave vector (k) for parallel propagation through the plasma. In addition to standard R- (right) and L- (left) hand mode waves, they identified a unique R-mode wave with a resonance frequency equal to the electron cyclotron frequency (Ω_e), the “whistler” mode. They concluded that a radiated wave could penetrate the plasma layer as a whistler mode over a wide range of conditions. To test this analysis they modeled the transmission efficiency using their one-dimensional plasma model discussed above. Their simulations confirmed their analysis of the dispersion relations. They concluded that the radiated wave penetrates the plasma layer as a whistler wave and is converted to the light mode in the vacuum region beyond the plasma boundary based on phase velocity considerations. From their study they project that relatively modest field strengths can mitigate blackout under practical conditions. For example, using $|\Omega_e| / \omega_p = 1.8$ and assuming a transmission frequency of 2.3 GHz, they estimate that field strengths of 1500 gauss (0.15 T) are required.

Whistler transmission modes were first identified when it was discovered that waves generated by lightning could penetrate the ionosphere and travel to the opposite hemisphere along the Earth’s magnetic field lines, being detected as a descending frequency “whistle.” In low-temperature plasmas where the collision rate is high, damping of the whistler mode is severe. Usui et al. [2000] have assumed a collisionless plasma, and the utility of transmission using whistler modes remains to be demonstrated through either more realistic modeling or experiment.

Theoretical calculations and limited experimental data suggest magnetic field mitigation of RF blackout in communication with space vehicles may be viable. There are a number of problems that must be overcome to produce a “magnetic window.” Weight and complexity (e.g., refrigeration systems for superconducting magnets) are obstacles to implementation. Rawhouser [1970] has stated that a 13 kG field is required for an S-band signal frequency and a plasma frequency near X band (i.e., 10^{12} electrons/cm³). Creation of a uniform field requires a very large coil radius. For the Shuttle, for example, a coil six feet in diameter might be required to achieve a uniformity of 10 percent along the axis. The window would work only when the plasma frequency is in a given range around X band. How the variations in the plasma frequency, collision frequency, and magnetic field both along and normal to the axis would affect transmission would need to be determined. Finally, a magnetic field of this magnitude would almost certainly modify the flow of the plasma along the vehicle’s surface. This would be a very difficult problem.

The strength of the field required and the physical size could require use of superconducting wire and possibly a flyable dewar to contain it. Rawhouser also states that it might have to be energized on the ground. Superconducting electromagnets weighing thousands of pounds are generally used in terrestrial applications to generate variable magnetic field strengths up to and beyond 1 tesla. However, research in superconductivity and magnetic materials is extremely active. New technologies may be on the horizon, and exploring and evaluating these possibilities has not been part of the current study. For example, Chapman et al. [2003] have recently discussed the potential for using carbon nanotubes to produce a new generation of lightweight airborne magnets. Figure 46 below shows their estimates of weight versus magnetic field strength using current technologies.

Figure 47 shows estimates for carbon nanotubes projected from superconductivity data reported in the literature. [This figure shows magnet weight with $J_c = 10^5 \text{ a/cm}^2$ for current technology composite structure (shown in green) and advanced technology composite using carbon nanotubes (shown in blue). Also magnet weight is shown for $J_c = 10^6 \text{ a/cm}^2$, characteristic of expected current density with carbon nanotube conductors, for both current technology composite structure (brown) and with advanced technology composites (red) using carbon nanotubes.] These weight estimates do not include cryogenic cooling systems certainly required for existing technologies. The weight needed to generate a 1-tesla field is on the order of 250 kg without cryogenic cooling.

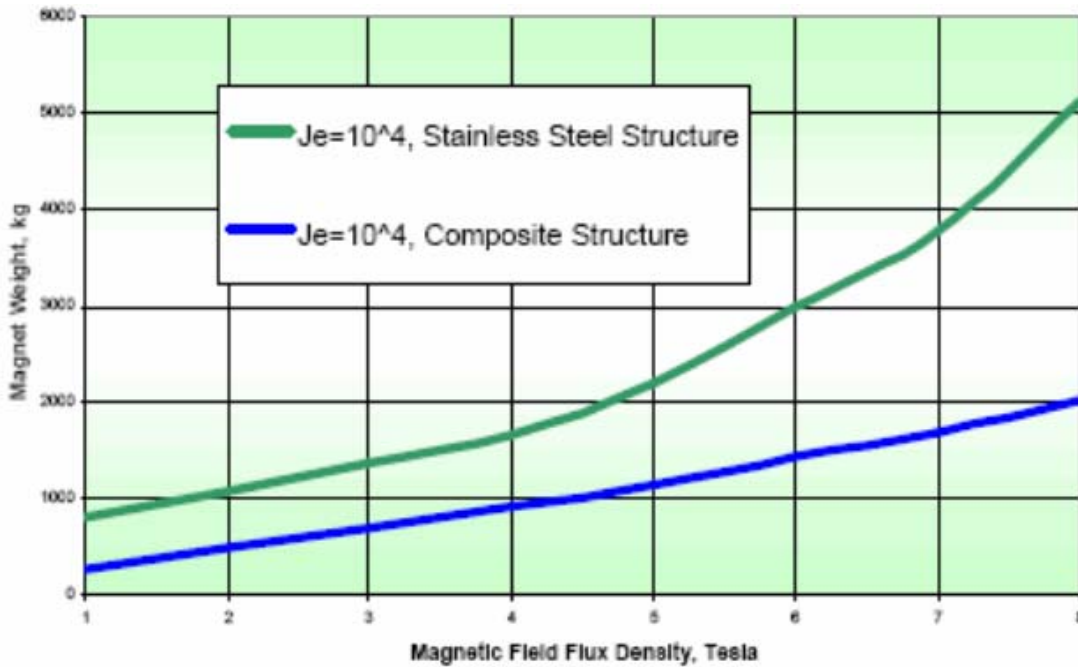


Figure 46. Comparison of magnet weight using current technology with stainless steel structure and composite material structure.

4.4 High Frequencies

The effect of shifting communication links to higher frequencies was examined. As noted in Sections 3.3 and 3.6, the attenuation broadside to the antenna is not significantly reduced with increasing frequency because the plasma is thin and collision dominated at least for frequencies less than 10 GHz. Since the peak plasma densities occur at much higher altitudes for the RAM C, the boundary layers are thicker and the collision frequencies are lower, resulting in very strong frequency dependence. Based on the RAM C results, one would select the highest practical frequency in order to minimize attenuation.

However, atmospheric and rain attenuation must be considered. As DirecTV™ system users are aware, when a rain cell passes over, synchronization is lost, causing a perfect picture to become a

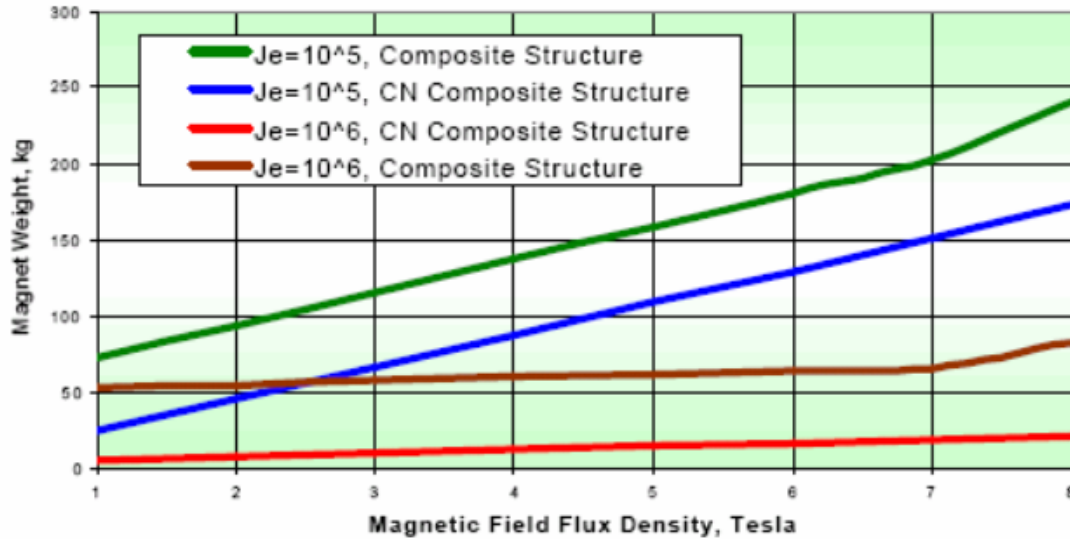


Figure 47. Estimates of magnet weight for carbon nanotubes (CN), projected from superconductivity data.

blank screen. DirecTV™ operates at 14 GHz. As a practical limit, unless a ground station diversity protocol is implemented, the communication link should be below approximately 10 GHz.

There are three potential ways to mitigate, if not eliminate, RF attenuation caused by rain. One would be to use two ground station sites sufficiently far apart to make the probability of both simultaneously experiencing rain heavy enough to attenuate RF propagation acceptably small. This would require that the launch vehicle antenna have a footprint that includes both ground station sites. The second methodology would be to use at least one ground station that only very rarely suffers from heavy rain. Thirdly, rain droplet size is a determining factor affecting attenuation of RF signals. Seattle, Colorado, and other areas in the Western United States would be desirable because very few rainstorms with large drops occur at those locations. Through scheduling of launch vehicle operations, one could avoid excessive RF attenuation by rain. The launch vehicle could be flown only on days when no rain with big drops is forecast. Such operational limitations could have little impact on the commercial RLV business.

Some advance planning should be done to use any of these mitigation strategies. First, specific radio frequencies above 10 GHz should be set aside for RLV communications, based on what bands might be available and the rain and atmospheric propagation properties of the bands. Second, suitable geographic regions should be identified that have the appropriate weather and infrastructure available for locating ground stations for RLV communications.

4.5 High Transmit Power

As described in Section 3.6, there is a limitation on the amount of CW power that can be transmitted from a slot without breaking down at a given altitude. This varies from about 20 watts at VHF (206 MHz) to 100 watts at S band (2.39 GHz). Once again, the higher one goes in frequency, the higher the power that can be transmitted without breakdown. Once again, atmospheric and rain attenuation impose a practical limit of about 10 GHz on frequency, but with the caveats discussed above.

The measured powers quoted herein are for a pulse width of 15.3 μsec , a relatively long pulse that gives breakdown results in the laboratory approaching the continuous-wave (CW) values. It may be possible to use coded short pulses to improve the results. Users of transmitter/receiver (T/R) tubes in receiver protection know that there is a high power spike that can leak through the device and can damage the diode detector. The spike occurs because of the time it takes the plasma within the T/R device to build up to the point at which it will effectively reflect the pulse. Whether this would allow sufficient power to be used to overcome the plasma attenuation would need to be investigated.

4.6 Observations on Raman Scattering

Nazarenko et al. [1994] discuss communication through plasma sheaths via a Raman (3-wave) scattering process. This approach was reviewed and found to have some interest as a laboratory experiment. However, the probability of it “solving” the blackout problem is believed to be very close to zero. Work at The Aerospace Corporation on “linear” coupling between longitudinal waves in warm plasma and electromagnetic waves [Stewart and Caron, 1965] was found to be an interesting research problem, but no warm plasma effects were ever seen in flight testing. Another question often raised was whether surface waves could propagate on the surface of a reentry vehicle (RV) and decrease isolation between slots. Once again, this was a phenomenon that could be observed with laboratory plasma but was not found for the real plasma profiles during reentry.

At high altitudes, one concern of the Raman researchers should be breakdown. They postulate an electric field for a pump power of 10^5 volts/meter. For an aperture the size of an S-band waveguide, this requires a power of about 80 kW.

At lower altitudes, the electron collision frequency is several hundred GHz. This is not only higher than the signal frequency in most cases, but also higher than the plasma frequency. In this region the plasma acts as a good conductor and can be well approximated by a thin sheet of a certain number of ohms per square. There is no so-called “turning point” where the pump signal goes from propagating to nonpropagating. The boundary layer can be either laminar or turbulent. One cannot estimate the noise spectrum by considering only thermal velocities of the electron gas.

As proposed, the communication would allow reception but not transmittal of a signal. Generating a signal from the ground to produce nonlinear coupling would involve very large amounts of power. Finally, if it is possible for the wave from the pump to reach the region where the reflected signal exists, it would appear to be much more feasible simply to modulate the pump signal and use it for communication.

5. Conclusions and Recommendations

The RF blackout mitigation strategies described in Section 4 fall into two general classes: passive approaches and active approaches. Passive approaches tend to be less costly than active approaches and argue for attention to design to minimize the plasma effects on communications signals. Active approaches entail manipulation of the plasma conditions and electron density in localized regions surrounding communication antennas to facilitate RF transmission. Implementing one or a combination of these passive approaches will minimize and possibly eliminate the blackout phenomenon. In our view, aerodynamic shaping is the most practical and influential approach for mitigating blackout. However, there are limitations in implementing such passive approaches and competing design requirements.

More active approaches are designed to manipulate the plasma conditions and electron density in localized regions surrounding the communications antenna to facilitate RF transmission. Injection of chemical quenchants or droplets that evaporatively cool the plasma and attach electrons and then recombine with positive ions, and applied magnetic fields are active approaches. These can be used periodically when passive approaches are inadequate. Among these, the use of quenchants is the more well-established, practical method, particularly when requirements are periodic rather than continuous. Magnetic field mitigation holds some promise, particularly for continuous operation, but has not been demonstrated sufficiently, and the requirements appear daunting using existing technologies. Both of these active approaches (quenchants/magnetic fields) could be placed on a more secure footing with additional experimental work to validate model calculations, particularly Usui's proposal that unique "whistler" modes may facilitate RF communications in a narrow range of "resonant" transmission frequencies. The authors propose such work in the recommendations below.

5.1 Conclusions

Aerodynamic shaping is the most promising approach for mitigating blackout and warrants further investigation. The most likely long-term reusable space transportation vehicle—the powered hypersonic air-breathing cruiser class—has great incentive to sharpen leading edges to reduce aerodynamic drag, which has the complementary benefit of making continuous RF communication more achievable.

Should blunt RLVs prevail, the application of sharp, slender probes or cones containing antennas protruding ahead of the shock wave should be evaluated.

As is well known, use of higher frequencies correlates with decreased blackout. However, atmospheric attenuation becomes an issue at frequencies greater than approximately 10 GHz. Methods to mitigate RF attenuation caused by rain were discussed. The ability to predict ionized flow fields for classes of vehicles most likely to emerge as hypersonic space transportation systems, with sufficient accuracy to identify the altitudes of blackout onset and recovery within reasonable bounds, has been demonstrated for altitudes greater than approximately 100 kft. This high-altitude regime is the most likely for future space transportation due to low g forces and low heat loads. For lower altitudes traversed by much higher velocity ballistic vehicles, the code predictions were in disagreement with measured data by factors up to seven. This is most likely due to uncertainties in chemistry of the heat shield material ablated and deposited in the high-temperature airflow, caused by extreme heat flux at low altitudes.

Determination of the interaction of RF with a known ionized layer, including reflection, attenuation, refraction, high-power breakdown limits, and also effects of the plasma on the antenna characteristics, have been demonstrated successfully. Analytic codes have been developed and are available to evaluate these phenomena.

Many concepts for mitigating blackout are presented in the literature of the 1960s and '70s. However, very few have been followed up with laboratory demonstrations. The **aerodynamic shaping** concept of Belov et al. [2001] for application to blunt leading edges/noses, and derivatives of that concept, appears to have promise. These researchers performed a very thorough analytic and experimental evaluation of the aerodynamics, heat transfer, and nose radius required to assure sufficiently low electron density in the aerodynamic flow further aft where the antenna is located, such that the antenna RF will experience negligible attenuation. Their sharp nose cone was made of porous sintered nickel-chromium alloy with porosity distribution tailored to assure survival of the nose cone cooled using pressurized air. At this time Aerospace has not evaluated this work in sufficient detail to validate or apply it to our systems.

A successfully flight-tested approach for mitigating blackout is the **injection of liquids (quenchants)**, through appropriately designed orifices, into the plasma flow of the reentering vehicle. This approach has demonstrated sufficient reduction in electrons to permit restoration of RF communication from a blackout condition. The Gemini 3 Reentry Capsule is an example of a successful flight demonstration that used injection of liquids into the flow to alleviate blackout. The Gemini 3 Reentry Capsule was manned by two astronauts and reentered the atmosphere on March 23, 1965 [Schroeder and Russo, 1968]. Significant levels of signal strength increase during the early portion of the water injection sequence over an altitude range of 272 to 246 kft were noted by ground stations on VHF telemetry (230.4 MHz) and VHF voice transmission (296.8 MHz). Enhancement of C-band beacon signal (5,690 MHz) was observed during the latter portion of the water injection sequence from 200 to 160 kft altitude. A comparison of calculated electron concentration—based on an assumption that the theory where the primary mechanism of electron concentration reduction is assumed to be recombination at or near the surface of water drops, with values deduced from the observed VHF attenuation data—shows the same trends. The data from this flight provide evidence that it is possible to alleviate RF attenuation on a blunt body by water injection in the flow field.

In addition to aerodynamic shaping and quenchants, one other concept appears worthy of further evaluation; this is the **magnetic window** concept. Theory supports the concept of applying a magnetic field, and laboratory experiments at NASA-Langley concluded that a 750-gauss magnetic field resulted in a 20 dB reduction in VHF attenuation, from 60 dB to 40 dB. Starkey [2003] analyzed a hypothetical air-breathing vehicle with very blunt leading edges (6-in. radius) and showed that this configuration generates thick plasma layers with very high electron density. He calculated a magnetic field strength of 10^4 gauss to penetrate this plasma. However, no reasonable air-breathing vehicle will have leading-edge radii that large. A Japanese team concluded from an analytical experiment that use of the whistler mode (where the magnetic field cyclotron frequency equals the RF frequency) could provide a window for RF transmission with a magnetic field strength of 1500 gauss [Usui et al., 2000]. Whereas current magnetic field strength generation technology may support up to 1500 gauss at acceptable weight and volume, the consensus is that achieving 10^4 gauss will require significant advances in superconducting technologies. The large difference in measured and estimated magnetic field strength requirements suggests that further in-depth laboratory experiments are needed. Reasons for the large disparity of magnetic field strengths between the NASA experiment and theoretical projections should be explored. Regarding the proposed whistler mode,

the effects of collision frequency should be evaluated, and if the use of whistler mode still looks attractive, experiments should be designed, using a shock tube that can produce well-defined plasmas, to evaluate its effectiveness. Chernyshev et al. [2006] have recently compared analytical models with shock tube data to demonstrate the potential for using applied magnetic fields to improve the aerodynamic characteristics of supersonic and hypersonic vehicles. The RF blackout mitigation strategies described above fall into two general classes: passive approaches and active approaches. Passive approaches tend to be less costly than active approaches and argue for attention to design to minimize plasma effects on communications signals. Example passive approaches to mitigating the RF blackout problem are: transmitting at high frequencies, with high power, from blunt vehicles with antennas designed with an aerodynamically shaped sharp leading edge, and, most importantly, use of sharp leading edges on a hypersonic air-breathing cruise vehicle. An example sharp leading edge is a blade analogous to the one NASA used successfully on the RAM C flights to mount ion-measuring probes. This blade was mounted at a 45° angle, slanted backwards, to the surface of the conical heat shield and measured the ion concentration from the vehicle surface out to the oblique shock wave, i.e., across the entire plasma layer thickness. This provides flight evidence that a blade with a very sharp leading edge (0.01 in.) survived down to 185 kft altitude (where it was retracted) without use of active cooling, i.e., to an altitude only 23 kft higher than where the Shuttle recovers from blackout. (Shuttle blackout determined from many flights begins at 265 kft, recovers at 162 kft, and lasts for 16 minutes.)

Implementing one or a combination of passive approaches will minimize and possibly eliminate the blackout phenomenon. In our view, aerodynamic shaping is the most practical and influential approach for mitigating blackout. However, there are limitations in implementing such passive approaches and competing design requirements. For example, the sharp tips must withstand the aerodynamic heating environment and keep their shape during reentry. Belov et al. [2001] had to use cooling to protect their protruding tip from the environment, making it an active system. Recent work has shown, however, that refractory materials are promising for use as sharp leading edges [Walker and Sullivan, 2003].

5.2 Recommendations

Several recommendations are proposed. The first is to study candidate mitigation methodologies such as aerodynamic shaping, injection of liquids, and application of a magnetic field, analytically and, where appropriate, experimentally, to prove that the concepts will work over the entire blackout period for a given vehicle configuration. For concepts shown to be viable, creation of full-scale system parametric designs is recommended, to assess size, weight, and complexity. A Failure Modes and Effects Analysis (FMEA) should then be performed for systems that progress to a potential implementation stage, to assure safety of the vehicle under all conditions.

Evaluation of indirect RF transmission from vehicles to the ground via satellites was beyond the scope of the present effort but might warrant exploration. This approach is used, for example, for the Space Shuttle. The parameters for commercial space vehicles should be explored, including considerations of employing commercial satellite constellations for communication.

The authors also recommend that an analysis be performed of frequency ranges suitable for commercial RLV developers, taking into account RF blackout amelioration and availability of frequencies not reserved for other applications incompatible with commercial launch vehicle use. Example issues to be explored for high frequencies would include atmospheric attenuation at approximately 10 GHz and above, compatibility with ground stations and satellites, and compatibility

with Automatic Dependent Surveillance - Broadcast Mode (ADS-B) architecture. Example issues to be explored for low frequencies include antenna size, compatibility with ground stations and satellites, and workarounds such as gap antennas around the vehicle. Such research could lead to exploration and potential development of all-weather approaches for RF communications.

6. Acronyms and Abbreviations

A	activation energy
ADB-S	Automatic Dependent Surveillance – Broadcast Mode
AIAA	American Institute of Aeronautics and Astronautics
AoA	angle of attack
AST	Office of Commercial Space Transportation
ASTV	Aero-assisted Space Transfer Vehicle
BLIMP	Boundary Layer Integral Matrix Procedure code
B ₀	magnetic induction
cc	cubic centimeter
C-band	frequency range from 4 to 8 GHz
CCl ₄	carbon tetrachloide
CGS	centimeter-gram-second units
CN	carbon nanotube
COTR	Contracting Officer’s Technical Representative
COTS	Commercial Orbital Transportation Services
CW	continuous wave
dB	decibel(s)
deg	degree(s)
e	charge on electron
EA	electron affinity
ELV	expendable launch vehicle
EM	electromagnetic
EMF	electromagnetic field
eV	electron volt
FAA	Federal Aviation Administration
FATE	Fuzing and Arming Test and Evaluation
FMEA	Failure Modes and Effects Analysis
ft	foot, feet
g	gram
g	unit of force: acceleration equivalent to gravitational force at rest
G	gauss
GHz	gigahertz
GPS	Global Positioning System
G _s	conductance
HYGPSIM	HYpersonic GPS SIMulation code
ICBM	intercontinental ballistic missile
in.	inch(es)
ISS	International Space Station
JSC	Johnson Space Center (NASA)
k	wave vector
K	potassium
K-1	Kistler Aerospace Corporation 2-stage developmental rocket
K _a -band	frequency range from 18 to 40 GHz
kft	kilofoot, kilofeet
kG	kilogauss

kHz	kilohertz
km	kilometer
kW	kilowatt(s)
LAP	launch assist platform
LaRC	Langley Research Center (NASA)
lb	pound(s)
LNA	low-noise amplifier
LOX	liquid oxygen
m	electron mass
MHD	magnetohydrodynamics
MHz	megahertz
mm	millimeter(s)
MoF ₆	molybdenum hexafluoride
Na	sodium
NAS	National Airspace System
NASP	National Aerospace Plane
NASA	National Aeronautics and Space Administration
N _e	electron density
OV	orbital vehicle
PIRATE	<u>P</u> oly- <u>I</u> terative <u>R</u> eacting <u>A</u> ero- <u>T</u> hermal <u>E</u> valuation tool set
PPM	parts per million
qbar	dynamic pressure
Q _c	heat flux
RAM	Radio Attenuation Measurements
RANT	Reentry Antenna Test
REACH	REentry Aerothermal CHEmistry code
ReF ₆	rhenium hexafluoride
RF	radio frequency
RLV	reusable launch vehicle
R _N	nose radius
RpK	Rocketplane Kistler, Inc.
RV	reentry vehicle
s	second(s)
S	distance along surface of body from nose tip
SAIC	Science Applications International Corporation
SATMS	Space and Air Traffic Management System
S-band	frequency range from 2 to 4 GHz
SF ₆	sulfur hexafluoride
SSTO	single stage to orbit
STS	Space Transportation System (Space Shuttle flight numbering)
T	tesla
TDRSS	Tracking & Data Relay Satellite System
T/R	transmit/receive
U _∞	free stream velocity
V	velocity
VHF	very high frequency
WF ₆	tungsten hexafluoride
X-band	frequency range from 8 to 12.5 GHz

y	distance normal to body surface
α	angle of attack
Δ	shock standoff distance
ξ	ratio of downstream position to hemisphere radius
ρ_∞	free-stream density
τ_a	auto-detachment lifetime
ν	collision frequency
ω	frequency
ω_p	plasma frequency
Ω_e	electron cyclotron frequency

7. References

Aisenberg, S., and P. N. Hu, "The Removal of Free Electrons in a Thermal Plasma by Means of Rapidly Evaporating Liquid Additives," in *The Entry Plasma Sheath and its Effects on Space Vehicle Electromagnetic Systems, Vol. I*, NASA Langley Research Center, Oct. 13–15, 1970, pp. 617-622.

Akey, N. D., "Overview of RAM Reentry Measurements Program," in *Proceedings, The Entry Plasma Sheath and its Effects on Space Vehicle Electromagnetic Systems, Vol. I*, NASA SP-252, NASA Langley Research Center, Oct. 13–15, 1970, pp. 25–26.

Bachynski, M. P., et al., "Electromagnetic Properties of High Temperature Air," *Proc. IRE*, 347-356 (1960).

Belov, I. F., V. Y. Borovoy, V. A. Gorelov, A. Y. Kireev, A. S. Korolev, and E. A. Stepanov, "Investigation of Remote Antenna Assembly for Radio Communication with Reentry Vehicle," *J. Spacecraft and Rockets* **38**, 2, Mar.–Apr. 2001, pp. 249–256.

Bertin, J. J., *Hypersonic Aerothermodynamics*, AIAA Education Series, 1994.

Blottner, F. G., "Viscous Shock Layer at the Stagnation Point with Nonequilibrium Air Chemistry," *AIAA Journal*, vol. 7, no. 12, December 1969, p. 2281–2288.

Campbell, E. E. B., and R. D. Levine, "Delayed Ionization and Fragmentation en Route to Thermionic Emission: Statistics and Dynamics," *Annu. Rev. Phys. Chem.* 51(2000)65.

Chapman, J. N., R. S. Ruoff, R. J. Litchford et al., "Flightweight Magnets for Space Applications Using Carbon Nanotubes," 41st Aerospace Sciences Meeting and Exhibit, AIAA Paper 2003-330, 6–9 Jan. 2003.

Chernyshev, A. S., Y. P. Golovachov, Y. A. Kurakin, A. A. Schmidt, and D. Van Wie, "Effect of an Applied Magnetic Field on Blunt Body Plasma Flow," 44th AIAA Aerospace Sciences Meeting and Exhibit, AIAA Paper No. 2006-1002, January 9-12, 2006.

Christophorou, L. G., and J. K. Olthoff, "Electron Attachment Cross-sections and Negative Ion States of SF₆," *Int. J. Mass Spect.* 204(2001)27.

Cowperthwaite, R. L., H. Myers, and E. P. Bialecke, "Studies of Electron Attachment for the Alleviation of Radio Communications Blackout," in *The Entry Plasma Sheath and its Effects on Space Vehicle Electromagnetic Systems, Vol. I*, NASA Langley Research Center, Oct. 13–15, 1970, pp. 559-577.

Dunn, M. G., and S. W. Kang, "Theoretical and Experimental Studies of Reentry Plasmas," NASA CR-2232, April 1973.

Fuhs, A. E., "Flight Instrumentation for Reentry Plasma Sheath," AIAA/Northwestern University Fifth Biennial Gas Dynamics Symposium, AIAA Paper No. 1963-379, August 14-16, 1963.

Golden, K., EMRUN, Ver 15-3-04, Xontech Inc., Los Angeles, CA, 2004.

Grantham, W. L., "Reentry Plasma Measurements Using a Four-Frequency Reflectometer," in *Proceedings, The Entry Plasma Sheath and its Effects on Space Vehicle Electromagnetic Systems, Vol. I*, NASA SP-252, NASA Langley Research Center, Oct. 13–15, 1970, pp. 65–107.

Hall, D. W. et al., REACH, Reentry Aerothermal Chemistry, Ver 15-3-04, Science Applications International Corporation, King of Prussia, PA, 2004.

Huber, P. W., J. S. Evans, and C. J. Schexnayder, "Comparison of Theoretical and Flight-Measured Ionization in a Blunt Body Reentry Flow Field," *AIAA Journal*, vol. 9, no. 6, June 1971, pp. 1154–1162.

Hunter, S. R., J. G. Carter, and L. G. Christophorou, "Low Energy Electron Attachment to SF₆ in N₂, Ar, and Xe Buffer Gases," *J. Chem. Phys.* 90(1989)4879.

Jackson, T. A., "Power for a Space Plane," *Scientific American*, **295**, 2, August 2006, pp. 56-63.

Jones, Jr., W. L., and A. E. Cross, "Electrostatic Probe Measurements of Plasma Surrounding Three 25,000 Foot Per Second Reentry Flight Experiments," in *Proceedings, The Entry Plasma Sheath and its Effects on Space Vehicle Electromagnetic Systems, Vol. I*, NASA SP-252, NASA Langley Research Center, Oct. 13–15, 1970, pp. 109–136.

K-1 Vehicle, TA-10 Flight Experiments Design and Requirements Document, Kistler Document No. 21-Report N-001, Rev. C, December 19, 2002.

Kang, S. W., "Nonequilibrium, Ionized, Hypersonic Flow Over a Blunt Body at Low Reynolds Number," *AIAA Journal*, vol. 8, no. 7, July 1970, pp. 1263–1270.

Kowari, K., K. Leung, and B. D. Shizgal, "The Coupling of Electron Thermalization and Electron Attachment in CCl₄/Ar and CCl₄/Ne Mixtures," *J. Chem. Phys.* 108(1998)1589.

Lin, T. C., L. K. Sproul, D. W. Hall, and J. Sontowski, "Reentry Plasma Effects on Electromagnetic Wave Propagation," 26th AIAA Plasmadynamics and Lasers Conference, AIAA Paper No. 95-1942, June 19-22, 1995.

Lordi, J. A., R. J. Vidal, and C. B. Johnson, "Chemical Nonequilibrium Effects on the Flow in the Windward Plane of Symmetry of a Blunted Delta Orbiter," NASA TM X-2506, December 1971.

Mather, D. E., J. M. Pasqual, J. P. Sillence, and P. Lewis, "Radio Frequency (RF) Blackout During Hypersonic Reentry," AIAA/CIRA 13th International Space Planes and Hypersonics Systems and Technologies Conference, AIAA Paper No. 2005-3443, 2005.

Modica, A., G. Stepakoff, and H. Rosenbaum, "A Shock Tube Study of Plasma Alleviation by Oxide Dust," in *The Entry Plasma Sheath and its Effects on Space Vehicle Electromagnetic Systems, Vol. I*, NASA Langley Research Center, Oct. 13–15, 1970, pp. 531-558.

- Morris, R. A., P. M. Bench, K. E. Golden, and E. A. Sutton, "Characterization and Prediction of Hypersonic Plasma Effects," 37th AIAA Aerospace Sciences Meeting and Exhibit, AIAA Paper No. 99-0630, January 11-14, 1999.
- Nazarenko, S. V., A. C. Newell, and V. E. Zakharov, "Communication Through Plasma Sheaths via Raman (Three-Wave) Scattering Process," *Physics of Plasmas*, 1 (9), September 1994, pp. 2827–2834.
- Nusca, M. J. and G. R. Cooper, "Computational Simulation of EM Attenuation by Plasmas Formed in Hypervelocity Atmospheric Flight," 8th AIAA International Space Planes and Hypersonic Systems and Technologies Conference, AIAA Paper 98-1573, Apr. 27-30, 1998.
- Orton, G. F., and L. F. Scuderi, "A Hypersonic Cruiser Concept for the 21st Century," AIAA 98-5525, September 1998.
- Parmentier, E. M., K. L. Wray, and R. F. Weiss, "Aerophysical Plasma Alleviation," in *The Entry Plasma Sheath and its Effects on Space Vehicle Electromagnetic Systems, Vol. I*, NASA Langley Research Center, Oct. 13–15, 1970, pp. 579-616.
- Potter, D. L., "Introduction of the PIRATE Program for Parametric Reentry Vehicle Plasma Effects Studies," 37th AIAA Plasmadynamics and Lasers Conference, AIAA Paper No. 2006-3239, June 5-8, 2006.
- Raizer, Y. P., *Laser Induced Discharge Phenomena (Studies in Soviet Science: Physical Sciences)*, Plenum Publishing Corp. (1977), p. 28.
- Rakich, J. V., D. A. Stewart, and M. J. Lanfranco, "Results of a Flight Experiment on the Catalytic Efficiency of the Space Shuttle Heat Shield," AIAA/ASME 3rd Joint Thermophysics, Fluids, Plasma and Heat Transfer Conference, AIAA Paper No. 1982-944, June 7-11, 1982.
- Rawhouser, R., "Overview of the AF Avionics Laboratory Reentry Electromagnetics Program," in *Proceedings, The Entry Plasma Sheath and its Effects on Space Vehicle Electromagnetic Systems, Vol. I*, NASA SP-252, NASA Langley Research Center, Oct. 13–15, 1970, pp. 3–17.
- Rothman, H., T. Morita, and W. Scharfman, "Transmission Through an Ionized Medium in the Presence of a Strong Magnetic Field," in *Electromagnetic Aspects of Hypersonic Flight, Its Effects Upon Reentry Communication and Detection*, ed. Rothman, Moore, and Papa, (Spartan Books, Cleaver-Hume Press, 1964), pp. 196-212.
- Russo, F. P., and J. K. Hughes, "Measurements of the Effects of Static Magnetic Fields on VHF Transmission in Ionized Flow Fields," NASA TM X-907, March 1964.
- Rybak, J. P., and R. J. Churchill, "Progress in Reentry Communications," *IEEE Trans. on Antennas and Propagation*, vol. AES-7, no. 5, September 1971, pp. 879–894.
- Schexnayder, C. J., J. S. Evans, and P. W. Huber, "Comparison of Theoretical and Experimental Electron Density for RAM C Flights," in *Proceedings, The Entry Plasma Sheath and its Effects on*

Space Vehicle Electromagnetic Systems, Vol. I, NASA SP-252, NASA Langley Research Center, Oct. 13–15, 1970, pp. 277–303.

Schroeder, L. C., and F. P. Russo, “Flight Investigation and Analysis of Alleviation of Communications Blackout by Water Injection During Gemini 3 Reentry,” NASA TM X-1521, 1968.

Starkey, R. P., “Electromagnetic Wave/Magnetoactive Plasma Sheath Interaction for Hypersonic Vehicle Telemetry Blackout Analysis,” 34th AIAA Plasmadynamics and Lasers Conference, 23–26 June 2003, p. 1.

Steiger, M., L. Glatt, F. Fernandez, J. Fedele, and K. Golden, “Reentry Communication: Theoretical Analysis and Flight Test Results,” AIAA 8th Aerospace Sciences Meeting, AIAA Paper No. 70-220, January 19-21, 1970.

Stewart, G. E., and P. R. Caron, “Radiation From a Line Source in a Ground Plane Covered by a Warm Plasma Slab,” *IEEE Trans. on Antennas and Propagation*, vol. AP-13, no. 4, July 1965, pp. 600–611.

Stewart, G. E., “Laboratory Simulation of Reentry Plasma Sheaths,” *IEEE Trans. on Antennas and Propagation* **15**, 6, Nov. 1967.

Stewart, G. E., K. E. Golden, and D. Pridmore-Brown, “Radiation From Circumferential Slots on a Plasma-Clad Cone,” in *The Entry Plasma Sheath and its Effects on Space Vehicle Electromagnetic Systems, Vol. I*, NASA Langley Research Center, Oct. 13–15, 1970, pp. 411–425.

Swift, C. T., F. B. Beck, J. Thomson, and S. L. Castellow, Jr., “RAM C-III S-Band Diagnostic Experiment,” in *Proceedings, The Entry Plasma Sheath and its Effects on Space Vehicle Electromagnetic Systems, Vol. I*, NASA SP-252, NASA Langley Research Center, Oct. 13–15, 1970, p. 152.

“User’s Guide of the Boundary Layer Integral Matrix Procedure (BLIMP),” Aerotherm Report No. UM-70-20, June 22, 1970.

Usui, H., H. Matsumoto, F. Yamashita, M. Yamane, and S. Takenaka, “Computer Experiments on Radio Blackout of a Reentry Vehicle,” 6th Spacecraft Charging Technology Conference, AFRL-VS-TR-20001578, 1 September 2000, p. 107.

Walker, S. P., and B. J. Sullivan, “Sharp Refractory Composite Leading Edges on Hypersonic Vehicles,” 12th AIAA International Space Planes and Hypersonic Systems and Technologies Symposium, AIAA Paper No. 2003-6915, 15-19 December 2003.

Bibliography

Anon., *Proceedings, The Entry Plasma Sheath and its Effects on Space Vehicle Electromagnetic Systems, Vol. I*, NASA SP-252, NASA Langley Research Center, Oct. 13–15, 1970.

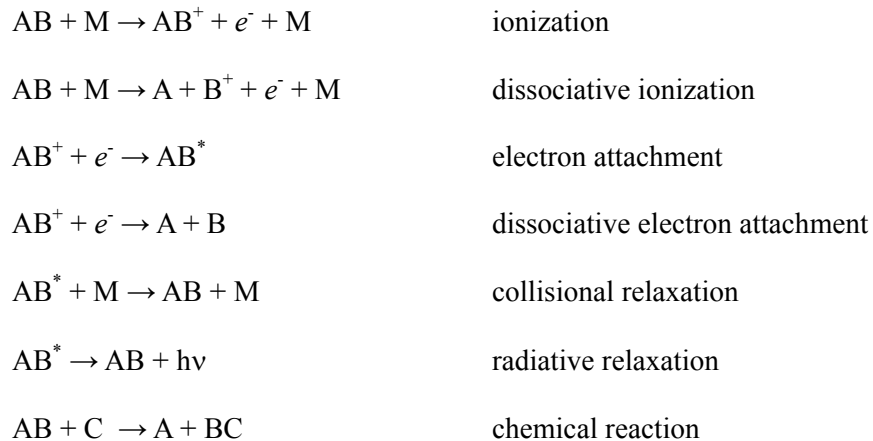
Heald, M. A., and C. B. Wharton, *Plasma Diagnostics with Microwaves*, Krieger Publishing, New York, 1978, chapter 6.

Rotman, W., H. K. Moore, and R. Papa (editors), *Electromagnetic Aspects of Hypersonic Flight, Second Symposium on the Plasma Sheath, Its Effects Upon Reentry Communication and Detection*, Spartan Books, Cleaver-Hume Press, 1964.

Appendix

Chemistry and Aerothermodynamics of Ionization in Plasma Sheaths Around Reentry Vehicles

This appendix will limit the description of the sources of electrons in the plasma sheath of reentry vehicles to be those due to the thermal environment created by the hypersonic flow. The plasma sheath forms due to the kinetic energy transfer from the reentry vehicle to the atmospheric gases. Other aerodynamic contributions come from the conversion of the viscous stresses to heat. A shock-wave forms along the leading boundary of the vehicle, compressing, heating, and ionizing the atmospheric gases. As the temperature of the air is raised the following sequence of events generally occurs: the molecules' rotational and vibrational degrees of freedom will be excited, while at higher temperatures the molecules will dissociate into their constituent atoms, and finally, still higher temperatures will ionize some of the atoms and molecules. Ultimately these effects can be described and characterized in terms collisional processes among molecules. The most important processes are the following:



where A, B, and C are generic constituent atoms of the atmosphere and M is a generic collision partner (atom, molecule, or surface). Each of these elementary processes has a characteristic rate that generally depends on temperature and the concentrations of the reactants on the left-hand side of the arrows; arrows indicate a transformation from reactant on the left to products on the right. The "final" concentration of atoms, molecules, ions, and electrons depends on how all of these rates balance at a given temperature.

Effective atmospheric chemical kinetics models can be developed, provided that the temperature-dependent rates of all of the processes among all the atmospheric species are known. Simplified kinetics models can then be combined with fluid mechanics models to provide a complete description of the flow field surrounding reentry vehicles. Even though air is mostly composed of 80% nitrogen (N_2) and 20% oxygen (O_2), because of the dissociation that occurs, 64 chemical reactions among 12 species are required to describe atmospheric kinetics. A sensitivity analysis has demonstrated that the number of reactions can be reduced to 11 among neutral species and 15 among charged species without significantly compromising the model for reentry vehicles [Dunn and Kang, 1973]. Table A-1, taken from Dunn and Kang, lists this subset of reactions. The first column shows the reactions in the forward direction, while the second and third columns give the forward rate coefficient (k_f) and

backward rate coefficient (k_b), respectively. The forward rate coefficients are seen to be of the form $k_f = C T^{-n} \exp(-A/T)$, where C is a constant and A is defined to be the activation energy (here expressed in units of temperature, K).

The space surrounding the reentry vehicle is divided into a conceptual grid to define a fluid mechanics model. The properties of each grid element (e.g., molecular composition, temperature, pressure) are determined by numerically solving the rate equations defined in Table A-1 with all the conservation equations of hypersonic flows. The concentrations of each species are tracked with rates of production and recombination, being combined with convection and diffusion when concentration gradients exist, contributing to and responding to the thermodynamic environment provided by all the species in the air. Each species is following its own conservation equations and contributing to the equation of state variables. The energies of dissociation and recombination contribute to the thermal environment. The bottom line for this study is that the electron densities throughout the flow around the vehicle are automatically derived from the net sum of electrons from all the reactions involving them.

Figures A-1 and A-2, taken from Dunn and Kang [1973], are solutions of the equations described in that reference and indicate the distribution of individual species (neutral and charged) for the simulated Shuttle reentering at 25 kft/sec at two altitudes (280 kft and 310 kft) and for different locations along the bottom surface (x) divided by the nose radius, which equals 4 ft. An S-band antenna is on the bottom surface at the $1.22 x/R_N$ location. The authors estimated transmission from that antenna and concluded, "It will probably be significantly attenuated for a period of approximately 15 minutes." It is noteworthy that this work was done in 1973, whereas the first Shuttle flight was on April 10, 1981. Shuttle blackout determined from many flights begins at 265 kft, recovers at 162 kft, and lasts for 16 minutes.

Table A-1. Chemical Reactions and Rate Coefficients used in Nonequilibrium Calculations
 [Dunn and Kang, 1973] (Reprinted courtesy of NASA)

NO.	REACTION	FORWARD RATE COEFF, k_F	BACKWARD RATE COEFF, k_B	THIRD BODY, M
	FORWARD DIRECTION	$\text{cm}^3/\text{mole sec}$	$\text{cm}^3/\text{mole sec}$ OR $\text{cm}^6/\text{mole}^2 \text{ sec}$	—
1	$\text{O}_2 + \text{M} \rightarrow 2\text{O} + \text{M}$	$3.6 \times 10^{18} T^{-1.0} \exp(-5.95 \times 10^4/T)$	$3.0 \times 10^{15} T^{-0.5}$	N, NO
2	$\text{N}_2 + \text{M} \rightarrow 2\text{N} + \text{M}$	$1.9 \times 10^{17} T^{-0.5} \exp(-1.13 \times 10^5/T)$	$1.1 \times 10^{16} T^{-0.5}$	O, NO, O ₂
3	$\text{NO} + \text{M} \rightarrow \text{N} + \text{O} + \text{M}$	$3.9 \times 10^{20} T^{-1.5} \exp(-7.55 \times 10^4/T)$	$1.0 \times 10^{20} T^{-1.5}$	O ₂ , N ₂
4	$\text{O} + \text{NO} \rightarrow \text{N} + \text{O}_2$	$3.2 \times 10^9 T^1 \exp(-1.97 \times 10^4/T)$	$1.3 \times 10^{10} T^{1.0} \exp(-3.58 \times 10^3/T)$	
5	$\text{O} + \text{N}_2 \rightarrow \text{N} + \text{NO}$	$7.0 \times 10^{13} \exp(-3.8 \times 10^4/T)$	1.56×10^{13}	
6	$\text{N} + \text{N}_2 \rightarrow \text{N} + \text{N} + \text{N}$	$4.085 \times 10^{22} T^{-1.5} \exp(-1.13 \times 10^5/T)$	$2.27 \times 10^{21} T^{-1.5}$	
7	$\text{O} + \text{N} \rightarrow \text{NO}^+ + e^-$	$(1.4 \pm 0.4) \times 10^6 T^{1.5} \exp(-3.19 \times 10^4/T)$	$(6.7 \pm 2.3) \times 10^{21} T^{-1.5}$	
8	$\text{O} + e^- \rightarrow \text{O}^+ + e^- + e^-$	$(3.6 \pm 1.2) \times 10^{31} T^{-2.91} \exp(-1.58 \times 10^5/T)$	$(2.2 \pm 0.7) \times 10^{40} T^{-4.5}$	
9	$\text{N} + e^- \rightarrow \text{N}^+ + e^- + e^-$	$(1.1 \pm 0.4) \times 10^{32} T^{-3.14} \exp(-1.69 \times 10^5/T)$	$(2.2 \pm 0.7) \times 10^{40} T^{-4.5}$	
10	$\text{O} + \text{O} \rightarrow \text{O}_2^+ + e^-$	$(1.6 \pm 0.4) \times 10^{17} T^{-0.98} \exp(-8.08 \times 10^4/T)$	$(8.0 \pm 2.0) \times 10^{21} T^{-1.5}$	
11	$\text{O} + \text{O}_2^+ \rightarrow \text{O}_2 + \text{O}^+$	$2.92 \times 10^{18} T^{-1.11} \exp(-2.8 \times 10^4/T)$	$7.8 \times 10^{11} T^{0.5}$	
12	$\text{N}_2 + \text{N}^+ \rightarrow \text{N} + \text{N}_2^+$	$2.02 \times 10^{11} T^{0.81} \exp(-1.3 \times 10^4/T)$	$7.8 \times 10^{11} T^{0.5}$	
13	$\text{N} + \text{N} \rightarrow \text{N}_2^+ + e^-$	$(1.4 \pm 0.3) \times 10^{13} \exp(-6.78 \times 10^4/T)$	$(1.5 \pm 0.5) \times 10^{22} T^{-1.5}$	
14	$\text{O}_2 + \text{N}_2 \rightarrow \text{NO} + \text{NO}^+ + e^-$	$1.38 \times 10^{20} T^{-1.84} \exp(-1.41 \times 10^5/T)$	$1.0 \times 10^{24} T^{-2.5}$	
15	$\text{NO} + \text{N}_2 \rightarrow \text{NO}^+ + e^- + \text{N}_2$	$2.2 \times 10^{15} T^{-0.35} \exp(-1.08 \times 10^5/T)$	$2.2 \times 10^{26} T^{-2.5}$	
16	$\text{O} + \text{NO}^+ \rightarrow \text{NO} + \text{O}^+$	$3.63 \times 10^{15} T^{-0.6} \exp(-5.08 \times 10^4/T)$	1.5×10^{13}	
17	$\text{N}_2 + \text{O}^+ \rightarrow \text{O} + \text{N}_2^+$	$3.4 \times 10^{19} T^{-2.0} \exp(-2.3 \times 10^4/T)$	$2.48 \times 10^{19} T^{-2.2}$	
18	$\text{N} + \text{NO}^+ \rightarrow \text{NO} + \text{N}^+$	$1.0 \times 10^{19} T^{-0.93} \exp(-6.1 \times 10^4/T)$	4.8×10^{14}	
19	$\text{O}_2 + \text{NO}^+ \rightarrow \text{NO} + \text{O}_2^+$	$1.8 \times 10^{15} T^{0.17} \exp(-3.3 \times 10^4/T)$	$1.8 \times 10^{13} T^{0.5}$	
20	$\text{O} + \text{NO}^+ \rightarrow \text{O}_2 + \text{N}^+$	$1.34 \times 10^{13} T^{0.31} \exp(-7.727 \times 10^4/T)$	1.0×10^{14}	
21	$\text{NO} + \text{O}_2 \rightarrow \text{NO}^+ + e^- + \text{O}_2$	$8.8 \times 10^{15} T^{-0.35} \exp(-1.08 \times 10^5/T)$	$8.8 \times 10^{26} T^{-2.5}$	
22	$\text{O}_2 + \text{O} \rightarrow 2\text{O} + \text{O}$	$9.0 \times 10^{19} T^{-1.0} \exp(-5.95 \times 10^4/T)$	$7.5 \times 10^{16} T^{-0.5}$	
23	$\text{O}_2 + \text{O}_2 \rightarrow 2\text{O} + \text{O}_2$	$3.24 \times 10^{19} T^{-1.0} \exp(-5.95 \times 10^4/T)$	$2.7 \times 10^{16} T^{-0.5}$	
24	$\text{O}_2 + \text{N}_2 \rightarrow 2\text{O} + \text{N}_2$	$7.2 \times 10^{18} T^{-1.0} \exp(-5.95 \times 10^4/T)$	$6.0 \times 10^{15} T^{-0.5}$	
25	$\text{N}_2 + \text{N}_2 \rightarrow 2\text{N} + \text{N}_2$	$4.7 \times 10^{17} T^{-0.5} \exp(-1.13 \times 10^5/T)$	$2.72 \times 10^{16} T^{-0.5}$	
26	$\text{NO} + \text{M} \rightarrow \text{N} + \text{O} + \text{M}$	$7.8 \times 10^{20} T^{-1.5} \exp(-7.55 \times 10^4/T)$	$2.0 \times 10^{20} T^{-1.5}$	O, N, NO

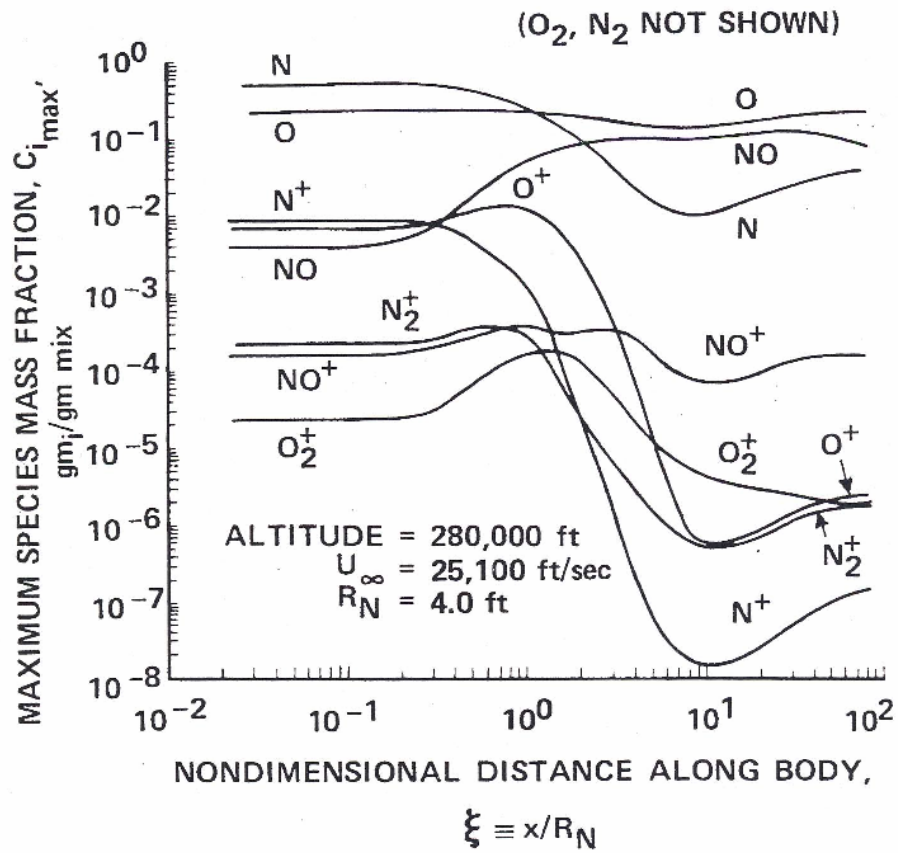


Figure A-1. Nonequilibrium flow species distribution for hemisphere on 20° cone at 280 kft altitude. [Dunn and Kang, 1973]. (Reprinted courtesy of NASA).

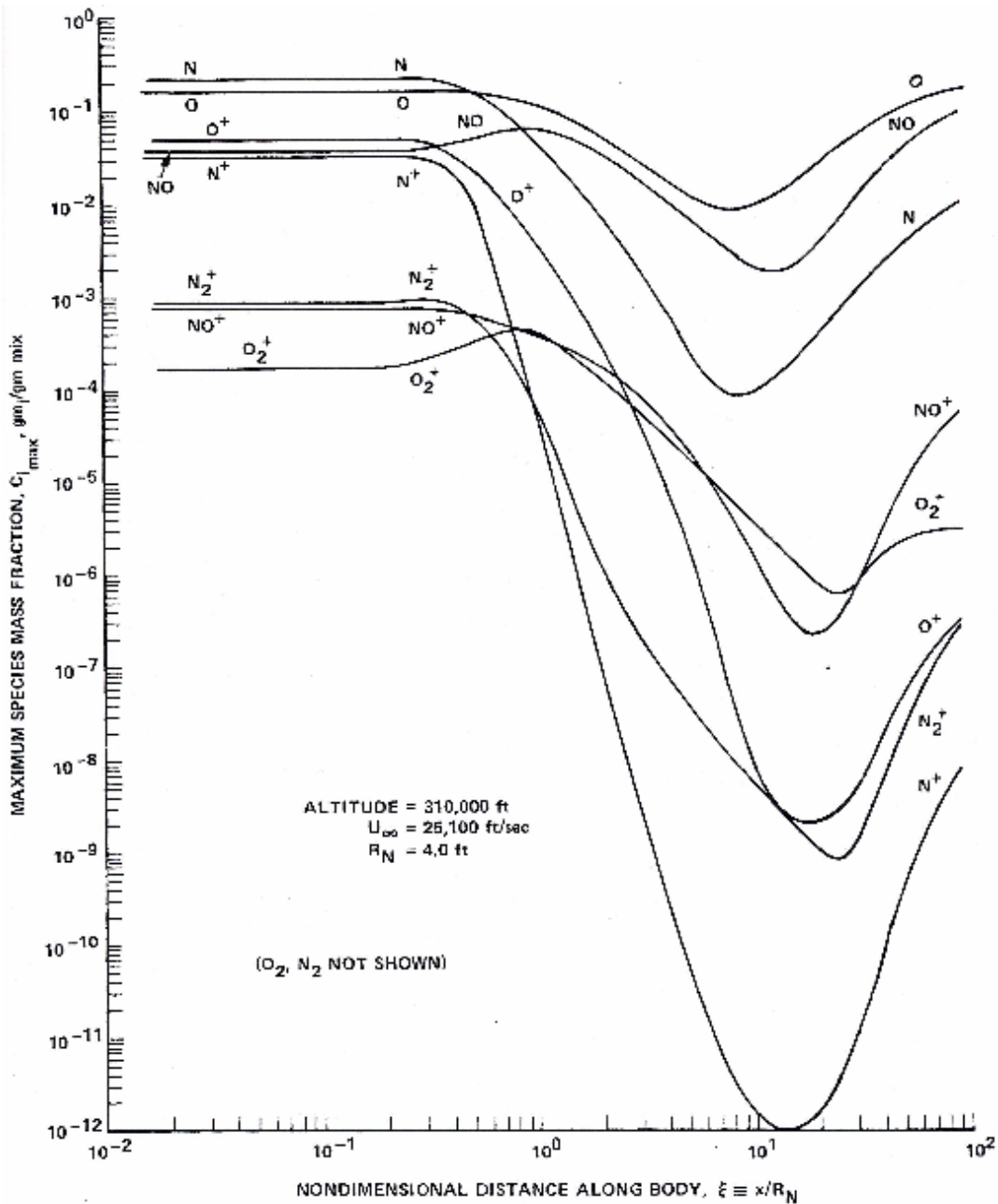


Figure A-2. Nonequilibrium flow species distribution for hemisphere on 20° cone at 310 kft altitude. [Dunn and Kang, 1973]. (Reprinted courtesy of NASA).

With this background, the terms equilibrium and nonequilibrium used by aerothermodynamicists can be more easily understood. The reactions described in Table A-1 occur over time. In a closed system, eventually the system will come to thermodynamic equilibrium such that the rates of production of all species are exactly balanced by their rates of consumption; there is no net change in concentration, temperature, or pressure. If the time to reach chemical equilibrium is fast relative to the velocity of the mass flow through the grid, the computational effort in modeling the system is

significantly reduced. The thermodynamic equations for solving equilibrium concentrations are much easier to solve than numerically integrating the rate equations to determine species concentrations. Nonequilibrium flows can have substantial effects on the thermodynamic states of hypersonic flows. On a molecular level, the rates of reaction are determined from the frequency and energy of collisions of the molecules, which are functions of the density and temperature of the air at each location, and the velocity and altitude of the vehicle. Figure A-3 taken from [Rakich et al., 1982] shows the trajectory of the Shuttle and indicates the velocity and altitude regime where nonequilibrium analyses must be made.

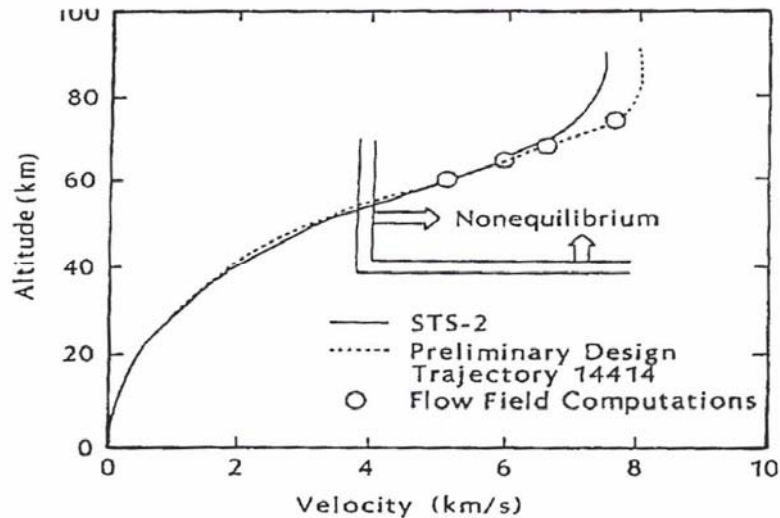
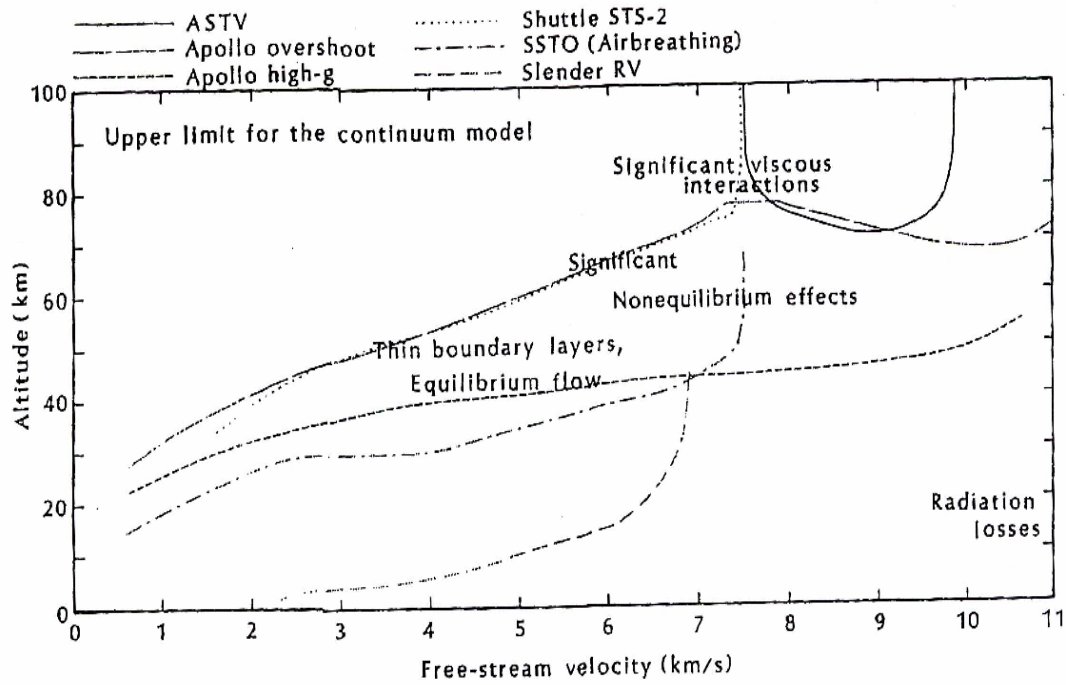


Figure A-3. Region of nonequilibrium flows for the Shuttle. [Rakich et al., 1982]. (Reprinted with permission of the American Institute of Aeronautics and Astronautics, Inc).

Finally, in Figure A-4 Bertin [1994] has examined typical trajectories of several typical reentry vehicle classes showing regimes where certain aerodynamic features must be included in the analysis (e.g., viscous interactions at very high altitudes and boundary layers at lower altitudes), as well as where equilibrium and nonequilibrium analyses will prevail. Trajectories of air-breathing hypersonic cruise and boost glide vehicle trajectories will be added to this chart in ensuing months.

The foregoing describes the source of electrons surrounding reentry vehicles. These electrons interfere with ground communications. In this report, various mitigation strategies, such as injection of chemical quenchants, are described.



ASTV = Aero-assisted Space Transfer Vehicle; SSTO = single stage to orbit

Figure A-4. Modeling flow phenomena for hypersonic flight.
 [From Bertin, J. J., *Hypersonic Aerothermodynamics*, reprinted with permission of the American Institute of Aeronautics and Astronautics, Inc.]